Synthesis and Surface Engineering towards Complex Nanomaterials

Ryan Kastilani

A dissertation

submitted in partial fulfillment of the

requirements for the degree of

Doctor of Philosophy

University of Washington

2019

Reading Committee:

Lilo D. Pozzo, Chair

Qiuming Yu

Vincent C. Holmberg

Program Authorized to Offer Degree:

Chemical Engineering

University of Washington

Abstract

Synthesis and Surface Engineering towards Complex Nanomaterials

Ryan Kastilani

Chair of the Supervisory Committee:
Weyerhaeuser Professor Lilo D. Pozzo
Department of Chemical Engineering

From the self-cleaning properties of the lotus leaf to smartphones that have hundreds of millions times more processing power than computers that sent mankind to the moon, the importance of nanotechnology is beyond dispute. Throughout the last couple of decades, the ever increasing demand for technology have driven not only the quest for new nanomaterials, but also efficient ways to produce them. In this work, novel methods towards producing complex nanomaterials is presented: from molecules to product. In the first part, a method to synthesize quantum dots (QD) from molecular precursors using ultrasound, in an emulsion system under controlled temperature, is presented. This method offers remarkable temporal control, leading to on-demand synthesis of QDs, and has 10x production capacity compared to the typical single-phase sonochemical synthesis of QDs. In the second part, a general bottom-up method to assemble two different kinds of nanoparticles together by engineering the nanoparticle surface is presented, which opens the path towards scalable production of multifunctional nanomaterials. Finally, a specific application of surface engineering and particle assembly is demonstrated in the context of reducing the brittleness of ceramic membranes for energy storage applications.

TABLE OF CONTENTS

LIST OF FIGURES

LIST OF TABLES

ACKNOWLEDGEMENTS

I thank my advisor Prof. Lilo Pozzo for guidance and instruction over the years. Thank you for allowing me to explore my interests; the opportunities I have today would not have been possible without your continuous support for my various ventures. I also thank the committee members for their all their inputs and expertise. I also thank the Pozzo group members and other fellow grad students, both past and present, from technical discussions to stupid jokes and random shouts at midnight in Benson Hall. It was nice to know I was not the only one feeling like an imposter.

I thank my friends for all the fun, camaraderie, and support. You guys have been with me through thick and thin. You offered me food when I was hungry and shoulders to cry on when I was drowning. You guided me when my path went astray. The laughs we had kept me sane throughout all these years. Whether through Blue Sky, tennis, or some other fateful way, I truly, truly, treasure our moments together. I would not be the person I am today without you guys.

I thank my parents for being a reflection of God's love since day 0. There are no words to describe my gratitude.

Above all, I thank my lord, Jesus Christ, for without him, I am nothing.

Now there are also many other things that I want to thank, specific people, specific instances. Were every one of them to be written, I suppose that the world itself can barely contain the books that would be written.

DEDICATION

To my friends and family, with love.

Chapter 1. INTRODUCTION AND THEORY

Nanoscience and nanotechnology is the understanding and application of matter that are less than 100 nm in at least one dimension. At this length scale, unique physical and chemical properties arise due to quantum mechanical effects that begin to dominate over classical physical descriptions. It is also the scale in which surface and interfacial properties dominate over bulk properties due to the rapidly increasing surface area to volume ratio. Nanoscience has always been around us, ubiquitous in nature long before its conceptualization by humanity. The lotus leaf is a classic example, where its self-cleaning feature arises from hydrophobic protrusions or surface roughness in the nanoscale.[1] Throughout the last couple of decades, nanotechnology has found applications in various fields, including electronics, medicine, renewable energy, and environmental remediation, among others. Yet, the constant quest for new materials and technologies has led to continued research in nanoscience. It is an exciting avenue and there is still much to be explored and discovered. The rest of this chapter is dedicated to establishing fundamental concepts and the motivation for this whole body of work.

1.1 PARTICLE INSTABILITY

Particle stability refers to the ability for the particles to remain suspended with each particle maintaining its original geometry. Stability is kinetic in nature, rather than thermodynamic, since there exists a state with a lower free energy in which the particles do not maintain stability. Stable particles are in a local thermodynamic minimum and remain stable if there is a sufficient energy barrier preventing the system from reaching the global minimum. Thus, if a dispersion is called stable, it is important to know the time scale of this stability. There are many mechanisms of instability: phase separation, aggregation, coalescence, and Ostwald ripening among others. If a dispersion is called unstable, it is important to know the process through which instability occurs. Most often, dispersions are in a gravitational field, which can result in phase separation depending on the difference in density of the particles to that of the surrounding medium. If the density of the particles is smaller than the medium, creaming may occur, where the particles float towards the top. If the density of the particles is larger than the medium, sedimentation may occur, where the particles sink to the bottom. For a spherical particle, the rate at which particles sediment obeys Stokes' Law of creeping flow:

$$v_{sed} = \frac{2a^2(\Delta\rho)g}{9\mu} \tag{1.1}$$

where a is the particle radius, $\Delta\rho$ is the density difference between the particle and the surrounding media, g is the gravitational acceleration, and μ is the viscosity of the surrounding media. If the particles are sufficiently small, the phase separation may not be observed due Brownian motion, random thermal diffusion of the particles. The net velocity for spherical particles is given by

$$v_{Brown} = -\frac{kT}{6\pi\mu a}\frac{d\,ln\,n}{dx} \tag{1.2}$$

where k is the Boltzmann constant, T is the temperature, n is the local particle number density, and x is the distance of travel. Sedimentation velocity is proportional to the square of the radius of the particle (eq 1.1), while the net velocity due to Brownian motion is inversely proportional to the particle radius (eq 1.2). In other words, as particles become smaller, the random thermal effect of Brownian motion begins to dominate over the gravitational pull on the particles. At steady state, there is a balance between these two forces and there exists a distribution of particle concentration:

$$n(z) = n_0\, exp\left[\frac{-\pi d^3(\Delta\rho)g}{6k} z\right] \tag{1.3}$$

where n_0 is the number concentration of particles, d is the particle diameter, and z is the distance from the bottom of the container.

While randomly diffusing in dispersion, particles may come sufficiently close to each other, and attractive van der Waals forces may cause them to aggregate or coalesce, depending on whether particles are solid or fluid. Aggregation is the process in which particles 'stick' together to form a larger structure. For example, two spherical gold particles may aggregate together to form a dumbbell-shaped particle. These dumbbells may, in turn, aggregate with any other particle in dispersion to form even larger structures. On the other hand, coalescence is the process in which two fluid particles merge together to become a single entity. For example, two oil droplets in water may come together to form one larger droplet. Unlike aggregation, coalescence reduces interfacial area between the dispersed phase and the media.

Ostwald ripening is the process in which larger particles become larger, while smaller particles shrink until they completely disappear. Molecules from the smaller particles diffuse through the media and add to the larger particles. This occurs as a consequence of the Kelvin effect, where compared to a bulk material, smaller particles have larger vapor pressure, or in this case, higher solubility. The Kelvin Equation describes how the saturated vapor pressure changes as a result of a curved interface, and hence, as function of size:

$$p_r = p_\infty\, exp\left(\frac{2\sigma V}{aRT}\right) \tag{1.4}$$

where p_∞ is the vapor pressure at a flat interface, σ is the interfacial tension, V is the molar volume of the curved material, a is the radius, R is the gas constant, and T is the temperature. For solubility, the vapor pressures in eq 1.4 are simply replaced by solubility. Similar to coalescence, Ostwald ripening reduces interfacial area. However, unlike coalescence, Ostwald ripening requires a finite solubility of the dispersed material because of its diffusive nature.

1.2 INTERPARTICLE INTERACTION AND PARTICLE STABILITY

As particles diffuse in dispersion, they will undoubtedly come in proximity with each other and start to feel the effect of van der Waals forces. Van der Waals interactions are molecular in origin, but Hamaker showed that the van der Waals interaction between two macroscopic objects, such as flat plates or colloids, can be obtained by integrating pairwise interaction between all molecules in one body and those in another.[2] For two spheres, the potential energy between the two bodies is given by

$$\Phi_{vdW} = -\frac{A}{6}\left[\frac{2a_1a_2}{S_0^2+2a_1S_0} + \frac{2a_1a_2}{S_0^2+2a_1S_0+2a_2S_0+4a_1a_2} + ln\left(\frac{S_0^2+2a_1S_0+2a_2S_0}{S_0^2+2a_1S_0+2a_2S_0+4a_1a_2}\right)\right] \tag{1.5}$$

where A is the effective Hamaker constant, a_1 and a_2 are the radii of the two particles, and S_0 is the distance of closest approach. The Hamaker constant is not a true constant, but rather a measure of van der Waals strength for a particular bulk material. The effective Hamaker constant used in eq 1.5 takes into account the surrounding medium and can be computed from the Hamaker constant of the individual particles and that of the surrounding medium in vacuum. For the interaction between particles P dispersed in medium M, the effective Hamaker constant can be estimated by[3]

$$A_{PMP} = A_{PP} + A_{MM} - 2\sqrt{A_{PP}A_{MM}} \tag{1.6}$$

where A_P and A_M are Hamaker constants of the particle and the medium, respectively. The effective Hamaker constant between two particles with the medium in between can be thought of as two particles displacing the medium in the space occupied by the particles, and the cross term in eq 1.6 is simply the geometric average of the two pure Hamaker constants. Note that A_{PMP} is always positive given positive values of A_{PP} and A_{MM} and the negative sign in eq 1.5 means that van der Waals interaction between two particles of the same type are always attractive.

With particles getting attracted to each other, one would expect to observe rapid aggregation or coalescence, and yet this is not the case due to charge separation at the interface of particle and media. Particle charging may be innately due to the particle itself, or due to molecules that exist on the surface of the particles. Regardless of the mechanism, electrostatic repulsion due to these charges on the particle surfaces is responsible for particle stability against aggregation or coalescence. The expression for the potential energy between two particles due to particle charging can be derived from the Poisson Equation[4] and by applying the Derjaguin approximation:[5]

$$\Phi_E = \frac{64\pi a n_\infty kT}{\kappa^2}\tanh^2\left(\frac{ze\psi_\delta}{4kT}\right)\exp(-\kappa S_0) \tag{1.7}$$

where a is the radius of the particle, $n_\infty$is the total ion concentration in the bulk solution, z is the valency of ions in solution, e is the electron charge, ψ_δ is the surface potential relative to the bulk solution, and κ is the Debye parameter defined as

$$\kappa = \sqrt{\frac{2e^2z^2n_\infty}{\epsilon\epsilon_0 kT}} \tag{1.8}$$

where ϵ is the dielectric constant of the medium and ϵ_0 is the permittivity of vacuum. The sum of the potentials arising from van der Waals attraction (eq 1.5) and surface charge repulsion (eq 1.7) gives the total potential between two particles and is known as the DLVO theory[4], named after the pioneers in this area: Derjaguin, Laudau, Verwey, and Overbeek.

The Debye parameter (eq 1.8) can be thought of as a measure of ionic strength of the medium. Ions screen electrical potential and thus reduce the electrical repulsion between particles (Figure 1.1). At 1 mM or 10 mM, the potential energy as a function of energy shows a typical ‘DLVO curve’, where electrostatic repulsion dominates at larger distances and van der Waals attractions dominate at smaller distances. In order for colloids to aggregate or coalesce, the particles must overcome the energy barriers established by electrostatic repulsion. In the absence of other stabilizing forces, under energy barriers less than a few kT, particles will typically undergoe rapid aggregation as they have good probability to overcome this energy barrier. At 100 mM of salt concentration, there are enough ions in solution to completely screen out electrostatic repulsion and the dispersion will undergo rapid aggregation. Note that even with large energy barriers, van der Waals attraction will eventually dominate at shorter distances, and hence stable colloidal systems are not thermodynamically stable (i.e. in a global minimum). Instead, they are stable kinetically because the particles have a low probability to cross the stabilizing energy barrier. The probability can be sufficiently low such that particles are stable for most practical purposes. For example, colloidal gold synthesized by Michael Faraday over 150 years ago are still stable today and can be observed in The Royal Institution in the United Kingdom.

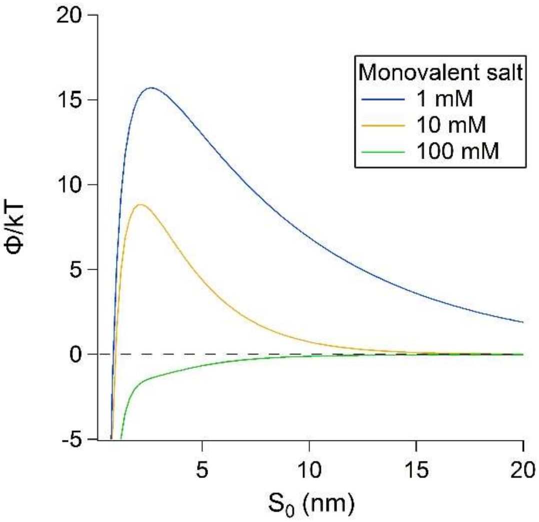

Figure 1.1: Example of DLVO plots for different monovalent salt concentrations.

In addition to salt concentration, another important parameter is pH. This is especially important when the origin of particle charging is sensitive the pH of the solution. For example, silica particles have hydroxyl groups on the surface, and their charge depends on the pH of the solution. Below pH 2, the hydroxyl group tends to be protonated to form $–OH_2^+$, and above pH 2, the hydroxyl group tends to be deprotonated to form $–OH^-$. At pH ~2, the hydroxyl groups balance between protonated and deprotonated states, and the surface carries no net charge. The pH at which the particle surface is uncharged is called the point of zero charge (PZC). Similar but different, the isoelectric point (EIP) is the pH in which functional groups are uncharged. In the absence of adsorbed ions on the particle surface, the PZC is the same as the EIP.

Particle surfaces may be modified to destabilize, enhance stability, or engineered in a way such that they assemble into desired structures. For example, gold nanoparticles, synthesized by the Turkevich method[6] in water, have adsorbed citrate ions as the capping agent for a large negative charge. The system can be destabilized by putting alkane thiols into the solution.[7] Thiol groups attach onto the surface of gold particles, displacing adsorbed citrate ions. The hydrophobic alkyl chains induce hydrophobic attraction, and the particles rapidly aggregate. Alternatively, the stability of the gold nanoparticles can be enhanced by putting polyethylene glycol-thiol (PEG-thiol) into the solution. Similarly, thiol groups bind to the surface of the gold, and the surface of the gold is now covered with a dense polymer adlayer. The achieved stability was theorized by Fischer[8] in the following way. When two particles approach each other, polymer chains from both particles would interpenetrate each other, pushing water out of the way, which introduces osmotic pressure because of the high concentration of polymer chains in the interpenetrated region. Osmotic pressure pushes water to flow into the area, thus pushing the two particles apart. If the particles approach even closer together, there will be an elastic recoil as the polymer adlayer from one particle is squeezed against the surface of the other particle. By using both alkane thiol and PEG thiol, Larson-Smith balanced hydrophobic attraction and steric repulsion of alkane thiols and PEG thiols, respectively, to control clustering of gold nanoparticles into a desired size.[7]

1.3 REDUCING AGENT MEDIATED AND SONOCHEMICAL SYNTHESIS OF NANOPARTICLES

The synthesis of nanomaterials can be classified as either top-down or bottom-up. In the top-down approach, a bulk material is ‘chiseled’ into the desired nanostructure. An example is lithography in semiconductor manufacturing, where a protective mask is put on certain areas, and unprotected areas are etched away. There are several disadvantages to top-down manufacturing. First, feature sizes are limited to about 10 nm, as determined by the electron beam and metal grain size. Second, the structures are limited to 2-D planar architecture, while certain desired properties such as plasmonic coupling are stronger by having 3-D structures. Third, top-down processes are expensive and inherently wastes large amounts of material.[9] Nevertheless top-down processing is still the gold standard in computer chip manufacturing due its extremely high precision. The bottom-up approach offers a more economical path, where nanostructures are built up from smaller pieces. Molecular precursors are used to synthesize nanoparticles, and these particles in turn are assembled together to form more complex structures. Assembly can be achieved by tuning the governing forces of these particles: surface engineering, environment modification, or through the application of an external field. For example, Larson-Smith modified the surface of gold nanoparticles using alkane thiols and PEG thiols to create clusters of nanoparticles of desired size.[7] Xi aligned conjugated polymers using electric fields to improve organic electronic performance.[10] Bottom-up approaches are more scalable because they often can be solution processed. Research efforts have been dedicated to better control these bottom-up processes. After decades of research, many different techniques have been developed to synthesize nanomaterials with various sizes, shapes, and compositions. Discussing each of them in detail is beyond the scope of this thesis. Herein, the focus is on concepts and techniques that pertain to the works that will be presented: chemical reduction of metal salts and sonochemical methods.

Metallic nanoparticles are commonly synthesized by reducing metal ions with reducing agents such as citrate or sodium borohydride. After reduction, uncharged metal atoms precipitate to form nanoparticles with controlled shape and size. A classic example is the Turkevich method to synthesize gold nanoparticles, which was first demonstrated in 1951.[6] In this method, water, gold chloride and sodium citrate are vigorously stirred and heated to boiling. Citrate is a weak reducing agent, but at high temperature, it can reduce gold ions to form gold nanoparticles. The size of the resulting nanoparticles can be controlled by tuning the ratio of gold chloride to citrate, with more citrate resulting in smaller particles.[11] Although the mechanism is complex, involving nanowire intermediates, and debated even as recent as 2015,[12–15] the procedure is simple to create monodisperse gold nanoparticles. Other metals salts and reducing agents are used to create metallic nanoparticles of various sizes, shapes, and compositions.

Another method to synthesize nanoparticles is to use ultrasound. Sonochemistry, the application of ultrasound to drive chemistry, has generated great interest over the last decade. When ultrasound is applied to liquids, the acoustic waves generate alternating compression and expansion of the liquid and this can lead to the formation of transient bubbles[16]. These bubbles can oscillate under the acoustic wave, accumulating energy and growing larger, until it reaches a critical size that is resonant with the incident acoustic wave. At this point, the bubbles cavitate, rapidly releasing the stored energy and producing incredibly high temperatures (~5000 K) and pressures (~500 atm) locally.[17] The advantage of this method is that not only bulk heating of the entire medium is unnecessary, but these localized extreme conditions allow access to unique chemistry that would otherwise be impossible.

Suslick and coworkers first demonstrated sonochemical synthesis of amorphous iron from iron pentacarbonyl.[18] The extreme conditions brought about by cavitation decomposed the organic constituents to release the metallic atoms. Metal carbonyls have an oxidation state of zero, and readily precipitate after the organic constituents are decomposed. If stabilizers such as oleic acid are also included, iron colloids are obtained instead.[19] Reactions that start from carbonyl precursors are typically carried out in non-aqeuous solvents such as hexadecane. Alternatively, it is also possible to synthesize nanoparticles from the sonication of metal salts dissolved in water. The energy released by cavitation generates free radicals that can reduce the metallic ions, leaving behind the metallic atoms to nucleate and form nanoparticles. Often other organic constituents such as isopropanol or surfactants are used to enhance reduction and accelerate the reaction.

1.4 SOL-GEL PROCESS

The sol-gel process is a bottom-up method used to synthesize metal oxides, typically silica, from molecular precursors. For the synthesis of silica, alkoxysilane, typically tetraethyl orthosilicate (TEOS), is mixed with water and alcohol as a cosolvent (Figure 1.2). Alkoxy groups undergo hydrolysis reaction to form silanols. The silanol can then undergo a condensation reaction either with alkoxysilane or another silanol to form siloxane bonds. Monomers turn into dimers, dimers into trimers, and so on to eventually become small particles, also called sols. Depending on the reaction conditions and subsequent steps, various products can be formed, including colloidal particles, porous media, and thin films (Figure 1.3); the sol-gel process is important to many applications.

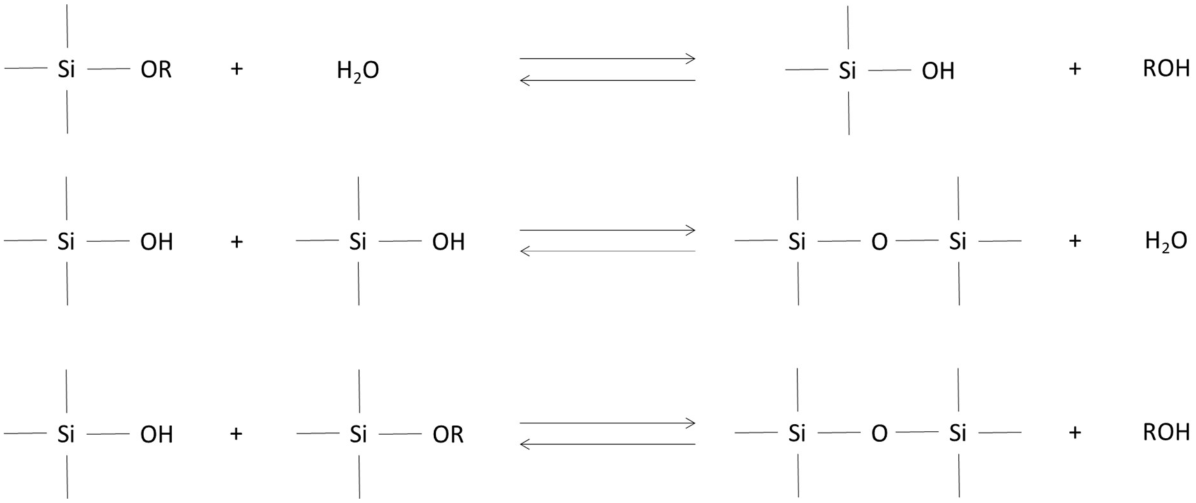

Figure 1.2: Schematic of the reactions that occur in sol-gel processing.

Numerous studies about the sol-gel process have been conducted, from the effect of composition to structural characterization of the products. The results are summarized in a book by Brinker and Scherer.[20] An important determination in the sol-gel process is the pH at which the reaction occurs. For silicates, an acidic environment leads to the formation of three-dimensional gel networks, which when dried, results in a solid material. On the other hand, a basic environment leads to the formation of stable particles or powders. This is also the basis for the Stöber process to synthesize monodispersed micron-sized silica particles.[21] Commercial products are also available for silica nanoparticles, commonly known as LUDOX®, ranging from 5 nm to 40 nm in diameter. These particles are stable in basic conditions, but may be destabilized by lowering the pH towards the PZC of 2, which eventually form gels.

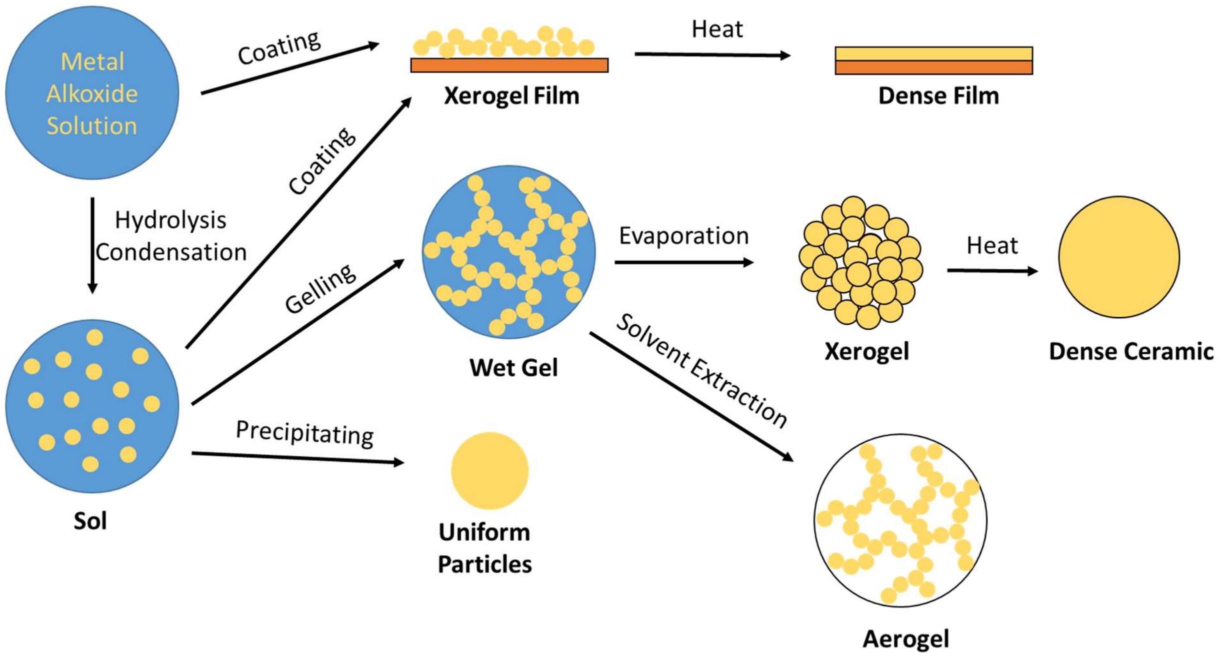

Figure 1.3: A summary of sol-gel processing.

1.5 OBJECTIVE AND APPROACH

This body of work will focus on the bottom-up approach used to synthesize nanomaterials. The process is divided into two parts. The first part is the synthesis of nanoparticles from molecular precursors. Depending on the molecular precursors, different techniques can be employed, each with their own advantages and disadvantages. If the starting materials are metal salts, then the sonochemical route may be employed. If metal alkoxides are used, then the sol-gel route may be employed. The resulting particles from this first step can be as simple as solid spheres, or as complex as multi-layered onion particles.[22]

The second part is the assembly of the primary particles into more complex nanostructures. For practical applications, this step is not always necessary, particularly if the primary particles themselves are sufficient for the desired application. For example, Li et al. developed core-shell nanoparticles as a sono-photoacoustic contrast agent,[23] and no assembly of these particles was necessary for the intended medical imaging purpose. Nevertheless, assembling nanoparticles into supracolloidal structures can enable multifunctional materials, such as recyclable catalysts, and these structures exhibit new properties that the primary particles do not exhibit by themselves, such as plasmonic magnetic coupling.[24,25] Furthermore, if the final desired product is a solid material, then the particles need to be assembled to form a gel. In this case, the structure of the assemblies in the nanoscale greatly influences the properties of the solid material. For example, the strength and reinforcement of fiber composites greatly depend on the orientation of the fibers within the matrix.[26]

This work embodies the whole process of nanomaterial synthesis, from the synthesis of nanoparticles to their assembly to form more complex structures. In chapter 2, experimental and analytical techniques are discussed, including the fundamental theories behind them. In chapter 3, I present a study of a relatively new system that is not yet explored in literature: sonochemical synthesis of nanoparticles via emulsions. CdSe is used as a model system to synthesize CdSe quantum dots (QD). In chapter 4, I present a method to control heteroaggregation of two species nanoparticles. The technique is general and can be applied to many different materials to form various structures, from heterodoublets to alternating worm-shaped heteroaggregates. In chapter

5, I present a specific application of particle assembly and surface modification towards flexible porous ceramics. Specifically, the structure and flexural properties of xerogel synthesized out of LUDOX silica particles and alkylsilanes is studied. This work was performed in collaboration with researchers from Membrion, a startup that spun out of the Pozzo Research Group, that attempts to create economical, ceramic-based ion exchange membranes. The goal of this project was to improve the mechanical properties of thin ceramic membranes. This work contributed to two pending patent applications, IP 47939.01US1 and IP 47939.03US2. In chapter 6, an outlook on nanoparticle, synthesis and assembly towards functional nanotechnology is given.

1.6 REFERENCES

(1) Barthlott, W.; Neinhuis, C. Purity of the Sacred Lotus, or Escape from Contamination in Biological Surfaces. *Planta* **1997**, *202*, 1–8.

(2) Hamaker, H. C. The London-van Der Waals Attraction between Spherical Particles. *Physica* **1937**, *4*, 1058–1072.

(3) Berg, J. C. *An Introduction to Interafaces & Colloids*; World Scientific: Singapore, 2014.

(4) Verwey, E. J. W.; Overbeek, J. T. G. *Thoery of the Stability of Lyophobic Colloids*; Elsevier: Amsterdam, 1948.

(5) Derjaguin, B. V. Friction and Adhesion. IV. The Theory of Adhesion of Small Particles. *Kolloid Z.* **1934**, *69*, 155–164.

(6) Turkevich, J., Stevenson, P. C., Hillier, J. A Study of the Nucleation and Growth Processes in the Synthesis of Colloidal Gold. *Discuss. Faraday. Soc.* **1951**, *11*, 55–75.

(7) Larson-Smith, K.; Pozzo, D. C. Scalable Synthesis of Self-Assembling Nanoparticle Clusters Based on Controlled Steric Interactions. *Soft Matter* **2011**, *7*, 5339–5347.

(8) Fischer, E. W. Elektronenmikroskopische Untersuchungen Zur Stabilität von Suspensionen in Makromolekularen Lösungen. *Kolloid Z.* **1958**, *160*, 120–141.

(9) Fan, J. a; Wu, C.; Bao, K.; Bao, J.; Bardhan, R.; Halas, N. J.; Manoharan, V. N.; Nordlander, P.; Shvets, G.; Capasso, F. Self-Assembled Plasmonic Nanoparticle Clusters.

Science **2010**, *328*, 1135–1138.

(10) Xi, Y.; Pozzo, L. D. Electric Field Directed Formation of Aligned Conjugated Polymer Fibers. *Soft Matter* **2017**, *13*, 3894–3908.

(11) Frens, G. Controlled Nucleation for the Regulation of the Particle Size in Monodisperse Gold Suspensions. *Nat. Phys. Sci.* **1973**, *241*, 20–22.

(12) Polte, J.; Kraehnert, R.; Radtke, M.; Reinholz, U.; Riesemeier, H.; Thünemann, A. F.; Emmerling, F. New Insights of the Nucleation and Growth Process of Gold Nanoparticles via in Situ Coupling of SAXS and XANES. *J. Phys. Conf. Ser.* **2010**, *247*, 012051.

(13) Pong, B. K.; Elim, H. I.; Chong, J. X.; Ji, W.; Trout, B. L.; Lee, J. Y. New Insights on the Nanoparticle Growth Mechanism in the Citrate Reduction of Gold(III) Salt: Formation of the Au Nanowire Intermediate and Its Nonlinear Optical Properties. *J. Phys. Chem. C* **2007**, *111*, 6281–6287.

(14) Wuithschick, M.; Birnbaum, A.; Witte, S.; Sztucki, M.; Vainio, U.; Pinna, N.; Rademann, K.; Emmerling, F.; Kraehnert, R.; Polte, J. Turkevich in New Robes: Key Questions Answered for the Most Common Gold Nanoparticle Synthesis. *ACS Nano* **2015**, *9*, 7052–7071.

(15) Kumar, S.; Gandhi, K. S.; Kumar, R. Modeling of Formation of Gold Nanoparticles by Citrate Method †. *Ind. Eng. Chem. Res.* **2007**, *46*, 3128–3136.

(16) Bang, J. H.; Suslick, K. S. Applications of Ultrasound to the Synthesis of Nanostructured Materials. *Adv. Mater.* **2010**, *22*, 1039–1059.

(17) Suslick, K. S. Sonochemistry. *Science* **1990**, *247*, 1439–1445.

(18) Suslick, K. S.; Choe, S.-B.; Cichowlas, A. a.; Grinstaff, M. W. Sonochemical Synthesis of Amorphous Iron. *Nature* **1991**, *353*, 414–416.

(19) Suslick, K. S.; Fang, M.; Hyeon, T. Sonochemical Synthesis of Iron Colloids. *J. Am. Chem. Soc.* **1996**, *118*, 11960–11961.

(20) Brinker, C. J.; Scherer, G. W. *Sol-Gel Science : The Physics and Chemistry of Sol-Gel Processing*, 1st ed.; Academic Press: San Diego, 1990.

(21) Stober, W.; Fink, A. Controlled Growth of Monodispersed Silica Spheres in the Micron Size Range. *J. Colloid Interface Sci.* **1968**, *26*, 62–69.

(22) Salazar-Alvarez, G.; Lidbaum, H.; López-Ortega, A.; Estrader, M.; Leifer, K.; Sort, J.; Suriñach, S.; Baró, M. D.; Nogués, J. Two-, Three-, and Four-Component Magnetic Multilayer Onion Nanoparticles Based on Iron Oxides and Manganese Oxides. *J. Am. Chem. Soc.* **2011**, *133*, 16738–16741.

(23) Li, D. S.; Yoon, S. J.; Pelivanov, I.; Frenz, M.; O'Donnell, M.; Pozzo, L. D. Polypyrrole-

Coated Perfluorocarbon Nanoemulsions as a Sono-Photoacoustic Contrast Agent. *Nano Lett.* **2017**, *17*, 6184–6194.

(24) Nie, Z.; Petukhova, A.; Kumacheva, E. Properties and Emerging Applications of Self-Assembled Structures Made from Inorganic Nanoparticles. *Nat. Nanotechnol.* **2010**, *5*, 15–25.

(25) Klinkova, A.; Choueiri, R. M.; Kumacheva, E. Self-Assembled Plasmonic Nanostructures. *Chem. Soc. Rev.* **2014**, *43*, 3976.

(26) Callister Jr., W. D.; Rethwisch, D. G. *Materials Science and Engineering An Introduction*, 8th ed.; John Wiley & Sons: New York, 2010.

Chapter 2. METHODS AND CHARACTERIZATION

2.1 ULTRAVIOLET-VISIBLE SPECTROSCOPY

Ultraviolet-visible (UV-vis) spectroscopy is technique to measure the extinction of light, as it passes through a material, as a function of wavelength. A monochromator is used to control the wavelength of the incident light, and the wavelength is swept from the UV region to the visible region, and even up to the infrared region depending on the tool. At each wavelength, the intensity of transmitted light through the sample is measured, while also knowing the intensity of the incident light. The governing equation for this technique is called Beer's law:

$$\log \frac{I_0}{I_T} = Abs = \epsilon LC \tag{2.1}$$

where I_0 is the intensity of the incident light, I_T is the intensity of the transmitted light, Abs is the absorbance, ϵ is the extinction coefficient, L is the path length of light through the sample, and C is the concentration. Absorbance is quite a misnomer because in addition to being absorbed and transmitted by the material, light can also be scattered. Hence, the reduction in intensity of the transmitted light is caused by absorption and scattering, which is often lumped together and simply called extinction. Absorbance is proportional to the amount of material that the light passes through, i.e. the path length and concentration, and the intrinsic property of the material, the extinction coefficient. During a measurement, the path length and concentration is typically constant, and it is the extinction coefficient that varies as a function of wavelength. For each wavelength, the proportion of light that is scattered and absorbed is dependent on the material.

If light is absorbed, the energy from the photon is used to excite electrons from one energy level to a higher level. For semiconductors, the valence and the conduction bands are separated by a certain amount of energy known as the band gap. Hence when performing UV-Vis spectroscopy on semiconductors, a sharp edge separating wavelengths with low and high absorbance is observed. Using photons with energies above this threshold promotes an electron from the valence band to the conduction band.

Beer's law can be used to measure the concentration of a solution or dispersion. If the extinction coefficient of the sample at a particular wavelength is known, the concentration can be directly calculated from eq 2.1. Otherwise, a Beer's law curve needs to be constructed first by measuring the absorbance at several different concentrations. The absorbance is plotted against concentration, and the resulting slope is ϵL (eq 2.1). Typically, a wavelength at a peak absorbance is chosen as the wavelength since it results in the highest signal to noise ratio. Note that the implicit assumption in Beer's law is that the absorbance varies linearly with concentration, which may not be true for samples with high concentration. As the sample becomes more concentrated, the effects particle-particle interactions and multiple scattering becomes more significant, and Beer's law is no longer obeyed. In addition, there are limitations with regards to the instrument. For example, if the absorbance of a sample is 2, only 1 % of the incident light is transmitted (eq 2.1), and the sensitivity of the detector is pushed to the limit.

The interaction of light with matter may also depend on the geometry of the matterial, and thus UV-vis spectroscopy can also be used to observe changes in structures. For example, the conjugated polymer poly(3-hexylthiophene) (P3HT) when dissolved in chloroform has a characteristic peak around 460 nm. When P3HT self-assemble into nanofibers, additional peaks arise at around 600 nm, and it is possible to extract quantitative information on the amount of fiber formation. Another example is gold nanoparticles in dispersion. Gold nanoparticles generally have a strong extinction peak at around 520 nm. The shape and location of this peak is dependent on the size of the gold nanoparticles and the distribution of sizes, e.g. larger gold particles result in a shift of the peak towards larger wavelengths.

2.2 PHOTOLUMINESCENCE SPECTROSCOPY

Photoluminescence (PL) spectroscopy is related to UV-Vis spectroscopy in that it shines incident light to a sample. But rather than measuring the extinction of the source light, PL spectroscopy measure light that is emitted from the sample that results from absorption of the source light. As previously mentioned, when light is absorbed, the energy can promote an electron from one energy level to a higher one, or in the case of semiconductors, from the valence band to the conduction band. This excited state is often not thermodynamically favorable, and electrons will tend relax to the original energy level and emit photons. This mode of relaxation is called radiative relaxation. In PL, the intensity of these released photons is measured.

Often, the energy that is absorbed is larger than the energy that is emitted, i.e. the PL peak is red-shifted from the absorption peak. This occurs because electrons have non-radiative relaxation mechanisms as well, such as vibrational relaxation, and they occur at much shorter time scales than radiative relaxation. Hence, some of the absorbed energy is used for molecular vibrations first, before radiative relaxation takes place. The wavelength difference between the absorption peak and the emission peak is called the Stokes shift.

Sometimes, emissions other than band edge emissions are also observed, particularly if the semiconductor material contains defects. These defects, whether in the bulk crystal structure or on a surface of a nanoparticle, introduce energy levels that lie in between the conduction band and the valence bands and that are often called ‘traps’. In this case, excited electrons can relax directly from the conduction band to the valence band, but it can also relax to these trap states before relaxing to the conduction band, leading to emissions at lower energies.

2.3 SMALL ANGLE X-RAY SCATTERING

Small angle x-ray scattering (SAXS) is a technique to investigate the structure of nanomaterials. A schematic of a SAXS experiment is shown in Figure 2.1. A collimated x-ray beam is incident on the sample, and is transmitted, absorbed, or scattered. The detector records the intensity of x-ray at various angles. Since the scattering angle depends on the incident wavelength, we define the scattering wave vector, q (or Q). Mathematically, q is defined as the difference between the propagation vector of the scattered and that of the incident x-ray. The magnitude of q is defined as

$$|q| = \frac{4\pi}{\lambda}\sin\left(\frac{\theta}{2}\right) \tag{2.2}$$

where λ is the wavelength and θ is the scattered angle. This essentially normalizes the scattering angle against the incident wavelength, and the intensity is analyzed as a function of q. The scattering profile $I(q)$ is often plotted on a log-log scale for analysis.

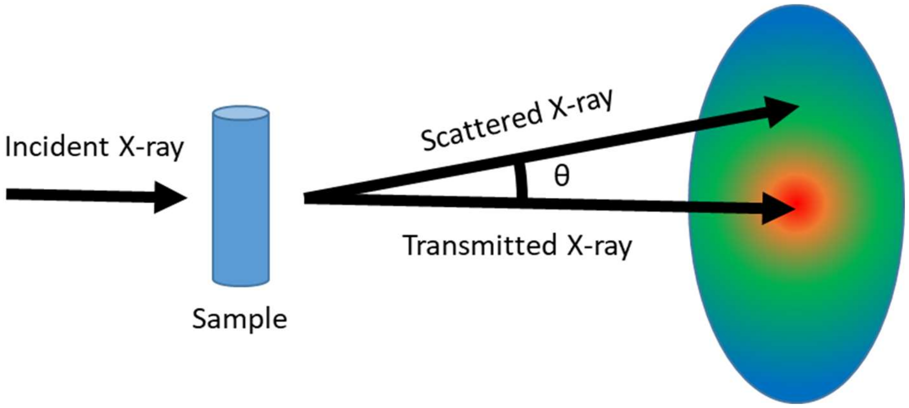

Figure 2.1: Schematic of a SAXS experiment.

Interactions between x-ray radiation and electrons in matter are responsible for the scattering of x-rays in matter. The scattering length density (SLD) is the volumetric average of all scattering lengths within the control volume. Hence, denser and more electron-rich materials result in a larger SLD. SLD is analogous to the refractive index, and the difference in SLD is what gives contrast in SAXS. The measured intensity in a SAXS experiment is the square of the Fourier transform of the SLD distribution:

$$I(q) = \left| \int \rho(r) e^{-iq\cdot r} dr \right|^2 \tag{2.3}$$

In other words, SAXS is a measure of the correlation of features in inverse space and the scattering profile is dependent on the nanoscale geometry and the material of the sample. It is especially useful to investigate the multi-scale structures, with smaller features appearing at high-q and larger features appearing at low-q (Figure 2.2). To probe lower q-ranges, the ultra-small angle x-ray scattering (USAXS), which can reach as low as 8 x 10^{-5} $Å^{-1}$, or a light scattering setup is necessary.

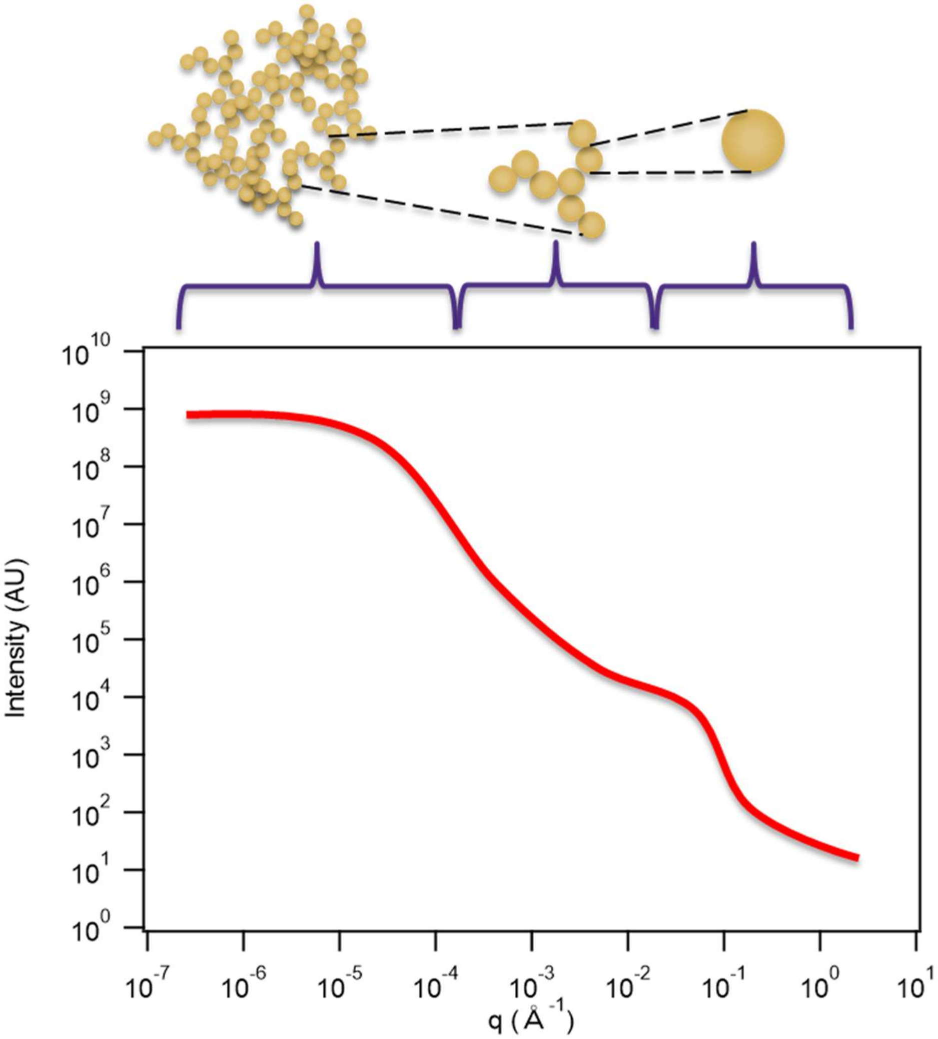

Figure 2.2: An example of small angle scattering data demonstrating the multi-scale measurement of structures.

For homogenous particles, the scattering intensity can be decomposed as

$$I(q) = nV_p\Delta\rho^2 P(q)S(q) + bkg \tag{2.4}$$

where n is the number density of particles, V_p is the volume of a single particle, $\Delta\rho$ is the difference in SLD between the particle and its surrounding, $P(q)$ is the form factor, $S(q)$ is the structure factor, and bkg is the incoherent scattering background. Note that n, V, and $\Delta\rho^2$ multiplies the profile by a constant factor. This means that on the log-log scale, these parameters shift the scattering profile up and down, but do not change the shape of the profile. The form factor gives information regarding the geometry of a single particle. The form factor has been worked out for various geometries. For spherical particles, the form factor is[1]

$$P_{sph}(q) = \left[\frac{3[\sin(qR) - qR\,cos(\mathrm{qR})}{(qR)^3}\right]^2 \tag{2.5}$$

where R is the radius of the sphere. An example of a scattering profile of a sphere is shown in Figure 2.3.

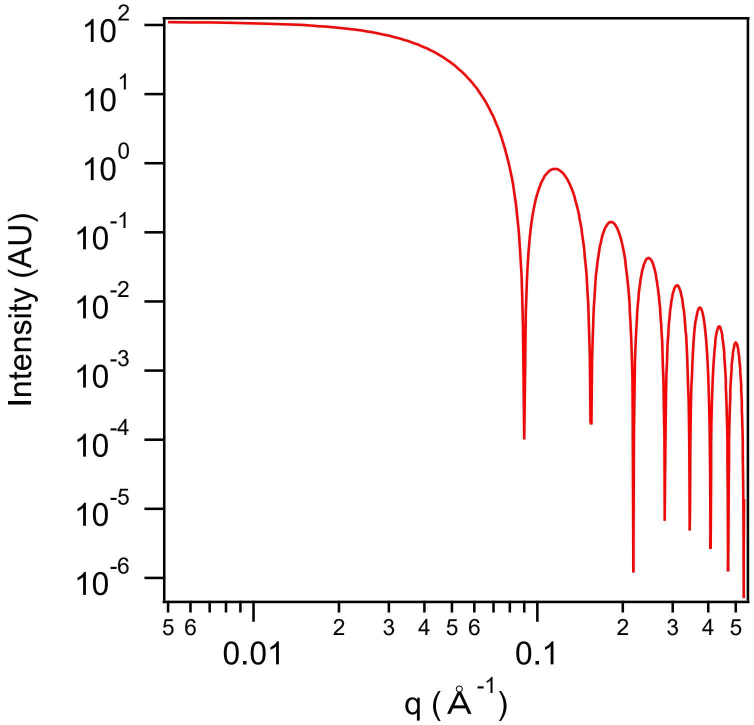

Figure 2.3: Calculated scattering profile of spherical particles with 50 Å using eq 2.5

The structure factor is related to the spatial correlation between scattering centers of particles and it gives information on the way these are arranged in space. In x-ray diffraction (XRD), the peaks that result from regular atomic spacing is the structure. In SAXS, the structure factor refers to the arrangement of particles in the system. For dilute systems, there are no correlations between the particles, and the structure factor approaches unity, i.e. only the form factor contributes to the scattering profile. For more concentrated systems, a peak that results from repeat particle-particle correlations may appear (Figure 2.4). However, for colloidal particles this is unlike the sharp Bragg peaks that arise from reproducible atomic correlations in crystal structures. These peaks are broader because of statistical variations in the repeat distance of larger and more disorganized colloidal systems. There can also be a decrease in intensity at low-q because, as the particles pack closely together, each particle is now surrounded by other similar particles effectively reducing the SLD difference that originally existed with the solvent. The aggregation of particles may also result in mass fractals, and the corresponding structure factor has been previously derived.[2]

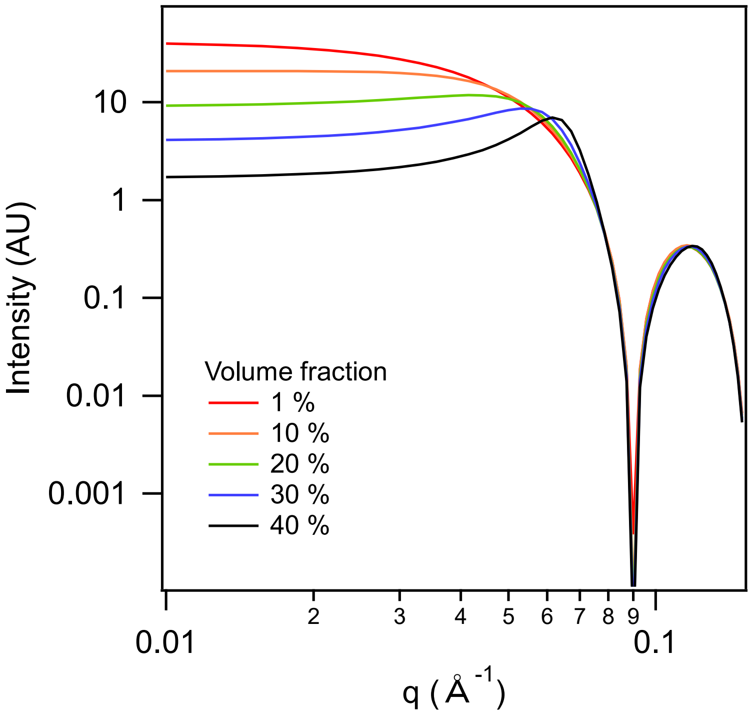

Figure 2.4: The effect of having more concentrated systems on the scattering profile of 50 Å spherical particles. The scattering profiles were calculated using the hard sphere structure factor and are matched on the second hump so that the first hump can be compared.

SAXS has a couple of advantages over other characterization techniques for nanomaterials. First, SAXS probes structures as an ensemble. Imaging techniques such as transmission electron microscopy (TEM) or scanning electron microscopy (SEM) are limited to a particular viewing area, and may also be limited to viewing only the surface structure. On the other hand, the scattering profiles obtained from SAXS represent an ensemble-average of the structures in the sample, probing both internal and surface structures. Secondly, SAXS can be performed in-situ for dispersions. For example, to image nanoparticle assembly in dispersions with electron microscopy, the dispersion is first deposited over a grid and dried, before imaging under SEM or TEM. However, the drying process may affect the resulting assembly and this can generate misleading results. The assessment of three-dimensional structures may also be difficult. SAXS allows the structure of the assemblies to be determined in their native environments.

2.4 X-RAY DIFFRACTION

The concept of x-ray diffraction (XRD) is similar to that of SAXS. While SAXS measures the scattering of x-rays at angles typically less than 6° and probes the correlation of electrons in particles, XRD measures the scattering of x-rays at higher angles and probes the correlation of atoms in crystalline materials. From a length scale perspective, electrons in a nanoparticle are viewed as a continuous distribution in SAXS, whereas XRD 'zooms in' to characterize the particles as made up of discrete atoms. If these atoms are regularly ordered and form a lattice, viz. non-amorphous materials, then the repeat distances between atoms across various planes in the lattice appear as peaks in an XRD profile. This is particularly useful to determine the lattice structrue of a sample. Physically, the interaction of incident x-rays with a sample produces constructive interference when the experimental conditions satisfy Bragg's Law:

$$n\lambda = 2d\sin(\theta) \tag{2.6}$$

where n is an integer, λ is the wavelength of the x-ray, d is the repeating lattice distance in real space, and θ is the angle between the sample stage and the incident x-ray. Unless characterizing an entirely new material, analysis of XRD data is often done by comparing the data with existing diffraction data. Given some elements that are, or might be, in the sample, the XRD profile is scanned against a database containing diffraction data for those compounds. If the peaks in the data match against those in the database, it suggests that the material is in-fact in the proposed structure.

2.5 DYNAMIC LIGHT SCATTERING

Dynamic light scattering (DLS) is a method used to measure particle sizes in colloidal dispersions. As small particles exhibit Brownian motion, fluctuations of scattered light intensity due to interference is monitored. Scattered light from each particle interfere constructively and destructively depending on the position of the particles, which changes with time. Given time t and a short interval τ, the intensity $I(t)$ and $I(t+\tau)$ are strongly correlated since the locations of the particles at time $t+\tau$ are close to that at time t. Over time, this correlation decreases as the particles move farther from their original locations. This correlation is described mathematically by the autocorrelation function:[3]

$$G(\tau) = \lim_{T\to\infty}\frac{1}{T}\int_0^T I(t)I(t+\tau)dt = \langle I(t)I(t+\tau)\rangle \tag{2.7}$$

where T is the experimental time. The instrument obtains this data by taking snapshots of the intensity at small discrete time intervals. For a monodisperse particle dispersion, the autocorrelation function has the form of an exponential decay:

$$G(\tau) = A_0 + Aexp(-\Gamma\tau) \tag{2.8}$$

where A_0 is signal from background noise, A is the instrument constant, and Γ is the decay constant. Eq 2.8 is used to fit the data and extract the decay constant. The decay constant is related to the particle's diffusion coefficient by

$$\Gamma = q^2 D \tag{2.9}$$

where q is the magnitude of the scattering wave vector, and D is the particle diffusion coefficient. Finally, assuming spherical particles, the diffusion coefficient can be related to the particle size by

$$a = \frac{kT}{6\pi\mu D} \tag{2.10}$$

where a is the radius of the particle, k is the Boltzmann constant, μ is the viscosity of the medium. When fitting a polydisperse sample, a range of particle sizes are put into bins, and the contribution of each bin is weighted accordingly to fit the autocorrelation function.

2.6 THREE-POINT FLEXURAL TEST

Flexural test is a method to measure the mechanical strength of brittle materials, such as ceramics. The material is set on two supporting pins, and a loading pin from the top slowly comes down the center of the sample. The force on the loading pin as a result of bending the material is recorded as a function of displacement. The force and displacement are normalized according to the geometry of the sample and experimental setup. For materials with a rectangular cross section, the flexural stress is defined as

$$\sigma_f = \frac{3F}{2bd^2} \tag{2.11}$$

where σ_f is the flexural stress, F is the force, L is the distance between the two supporting pins, b is the width of the sample, and d is the thickness of the sample. Flexural strain is defined as

$$\epsilon_f = \frac{6\mathrm{Dd}}{\mathrm{L}^2} \tag{2.12}$$

where ϵ_f is the flexural strain and D is the deflection distance. The stress is plotted against the strain to obtain a stress-strain curve. For ceramics, the stress-strain curve is linear until the material fails, and there is a sudden drop in force. The slope of the stress-strain curve is a measure of the material's stiffness and it is called the material's modulus. In this case, since the mechanical testing is performed by a flexural test, it is called the flexural modulus, defined as

$$E_f = \frac{\mathrm{L}^3 m}{4\mathrm{bd}^3} \tag{2.13}$$

where E_f is the flexural modulus, m the slope in a force/deflection curve. The stress and strain at which the material breaks are called flexural strength and fracture strain, respectively.

2.7 REFERENCES

(1) Guinier, A.; Fournet, G.; Walker, C. B. *Small-Angle Scattering of X-Rays*; John Wiley & Sons: New York, 1955.

(2) Teixeira, J. Small-Angle Scattering by Fractal Systems. *J. Appl. Crystallogr.* **1988**, *21*, 781–785.

(3) Berg, J. C. *An Introduction to Interafaces & Colloids*; World Scientific: Singapore, 2014.

Chapter 3. ON-DEMAND SONOCHEMICAL SYNTHESIS OF ULTRASMALL AND MAGIC-SIZE CDSE QUANTUM DOTS IN SINGLE-PHASE AND EMULSION SYSTEMS

Reproduced with permission from Journal of Physical Chemistry C, submitted for publication.

3.1 INTRODUCTION

Over the past decades, there has been great interest in the synthesis and application of semiconductor quantum dots (QDs) due to the fact that they exhibit tunable properties that are drastically different from their bulk counterparts via the effects of quantum confinement. In short, quantum confinement occurs when the characteristic size of a nanoscale particle approaches the exciton Bohr radius of the material, leading to unique optical and electronic properties, which are tunable by the size, shape, and composition of the QD particles.[1] Due to their unique properties, QDs find numerous applications including bio-labeling and imaging, light-emitting diodes (LEDs) and phosphors, solar cells, photodetectors, field-effect transistors (FET), and memory elements.[2–4] A subset of QDs include magic-size clusters (MSCs), which are small QDs – typically less than 2 nm in diameter – that consist of discrete sizes that correspond to a specific, well-defined number of atoms.[5,6] Their electronic structure sits at the interface between molecules and QDs, and they exhibit unique properties, sharp absorbance features, and entirely surface-state-based luminescence. Applications and advantages of MSCs include white-light LEDs, facile renal clearance in biological imaging, and their use as starting materials for the generation of more complex nanostructures.[6]

Typically, colloidal QDs are prepared by the hot-injection method, where molecular precursors are injected into a hot solvent at temperatures of up to several hundred degrees Celsius, successfully resulting in the synthesis of nanocrystals (NCs) with numerous sizes, shapes, and compositions.[7,8] Notably, this standard technique has a number of critical drawbacks that make it difficult to scale and that can result in batch-to-batch reproducibility issues. Since the method relies on the rapid injection of up to 50% of the total mixture volume, efficient mixing of the reagents at high temperature becomes difficult as reaction volumes become larger. Likewise, after the initial injection, the reaction temperature often needs to be adjusted quickly in order to control NC growth, and heat transfer becomes an issue as fluid volume and vessel sizes increase. Alternative approaches include the solvothermal method, where all precursors are initially mixed in a vessel that is then heated and cooled in a controllable manner.[9] However, decoupling of nucleation and growth is necessary to prevent polydispersity, so great care must be taken to ensure that there is sufficient nucleation within a short period of time, otherwise necessitating subsequent size-focusing processes such as Ostwald ripening, or size-selective post-synthetic purification processes that substantially decrease product yield. Moreover, in the case of multicomponent QDs, it is vital that the mixture be rapidly heated to a temperature where the reactivity of all components is matched, else the composition of the NCs will not reflect that of the original bulk solution.

A relatively new route toward NC synthesis is through sonochemistry, where ultrasound is applied to a solvent mixture that contains the NC precursors. When ultrasound is applied to a liquid, the alternating positive and negative pressure crests can lead to the formation of transient vapor bubbles or cavities. Furthermore, these bubbles oscillate and grow under repeated compression and expansion cycles, continually gaining potential energy. Eventually, the bubbles grow to a resonant size that can lead to their abrupt and violent collapse, resulting in an extremely rapid release of the accumulated energy in a highly localized space. This results in localized 'hotspots' with temperatures that have been estimated to reach 5000 K and pressures in excess of 1000 bar.[10,11] These extreme conditions, albeit spatially and temporally localized, lead to rapid reaction of the precursor molecules, resulting in NC nucleation and growth. Similar sonochemical methods have been used successfully to synthesize a wide variety of dispersed nanomaterials.[11] However, controlled and systematic studies are few, and the effects of sonication are often convoluted with other effects, including possible rise of the bulk solvent temperature, which results during continuous sonication without active cooling.

In this work, the sonochemical synthesis of ultrasmall and magic-sized CdSe QDs is reported in single-phase and emulsion-based systems, while actively maintaining the solvent temperature to minimize effects related to bulk temperature increases. We hypothesize that sonochemical synthesis in emulsion systems offers an efficient, accelerated, and controllable pathway toward the on-demand synthesis of complex nanomaterials.

3.2 EXPERIMENTAL

Chemicals

1-octadecene (90%), oleic acid (90%), oleylamine (70%), cadmium oxide (≥99.99%), selenium (≥99.99%), trioctylphospine (97%) (TOP), and dodecane (≥99%) were purchased from Millipore-Sigma (St Louis, MO USA). Hexanes (mixed isomers, 99.9%) and ethylene glycol were purchased from Fisher Scientific (Hampton, NH USA). All chemicals were used as received.

Precursor Preparation

The cadmium precursor, 84 mM cadmium oleate, is prepared in the following way. To a round bottom flask, 0.256 g of cadmium oxide, 20 mL octadecene, and 2.6 mL of oleic acid were added. Using a Schlenk line, the flask is degassed by applying vacuum while stirring at 800 RPM using a magnetic stir bar. Under nitrogen atmosphere, the flask is heated to 270°C and is held at this temperature for 30 minutes or until the mixture becomes clear and colorless; the temperature is then held for 30 additional minutes. At this time, the temperature is lowered to 150°C, and 1.3 mL of oleylamine is added. The temperature is then lowered to 100°C, and the flask is degassed for 30 minutes. Finally, the resulting product is cooled to room temperature. The selenium precursor, 1 M TOP:Se, is prepared by mixing Se powder and TOP overnight in a glove box until all the Se is dissolved and the solution is clear and colorless.

Sonochemical Quantum Dot Synthesis

The cadmium precursor is first mixed with the selenium precursor at a 1:4 molar ratio. A schematic of the synthesis process is depicted in Figure 3.1. In the emulsion system, 2.245 mL of the cadmium precursor is mixed with 0.755 mL of the selenium precursor in a 20-mL glass scintillation vial. The vial is hand-shaken to mix the two precursor solutions, before adding 7 mL of ethylene glycol. The capped vial is again shaken by hand vigorously to create a coarse emulsion. The vial is then placed in a cooling bath containing water at 20°C. Sonication is then initiated using a Branson 450 Digital Sonifier (400 W max power, 20 kHz), equipped with a 3/8” titanium horn directly immersed 0.5 cm into the solution. Sonication is performed continuously at a 20% power setting on the control panel, which has been calibrated to be equivalent to a power dissipation of 12.6 W (See Supplemental Information). Sonication is then temporarily stopped to collect sample aliquots at each relevant time stamp, and an equivalent volume of ethylene glycol is added into the scintillation vial such the volume is always kept at 10 mL. The volume of aliquot that is withdrawn is such that there is approximately 250 μL of oil phase (octadecene) in each aliquot. The water in the cooling bath is also exchanged with fresh cold water, and the sonication is continued. The temperature of the vials is also monitored with a thermocouple in order to separate the effect of sonication / cavitation from that of a possible bulk temperature increase.

Each sample aliquot is then centrifuged and decanted to separate the dispersed oil phase containing the quantum dots from the continuous ethylene glycol phase in the emulsions. These samples are referred as 'unpurified' because of the presence of excess unreacted precursors and organic components. The 'as-synthesized' samples are characterized by small-angle X-ray scattering (SAXS) and diluted about 100-fold in octadecene for UV-vis spectroscopy as a function of sonication time. For X-ray diffraction (XRD), the as-synthesized samples are purified by simply precipitating with the addition of excess ethanol. The powder is then separated and deposited onto a silicon wafer for analysis. Alternatively, the as-synthesized samples are diluted 10-fold in dodecane, and purification is performed by liquid-liquid extraction using an equivalent volume of methanol (250 μL) that is changed three times. After each addition of methanol, the samples are vortexed, and centrifuged. Care is taken to replace the dodecane lost during the extraction process to prevent the particles from precipitating, since precipitates are not re-dispersible. After cleaning, particles are also characterized by SAXS, diluted into hexanes 10-fold for UV-vis spectroscopy, 1000-fold for photoluminescence (PL) spectroscopy, and 100-fold for transmission electron microscopy (TEM).

In the single-phase system, the sonication procedure is very similar. The only difference is that the 10-mL reaction volume is entirely composed of the precursor mixture. No ethylene glycol is used and no emulsification is necessary. Also, for these samples, no makeup solvent is added upon removal of sample aliquots as a function of time. The as-synthesized samples are characterized with SAXS and diluted about 10-fold in octadecene for UV-vis spectroscopy. Purification of these samples is also performed by liquid-liquid extraction using an ethanol wash of equivalent volume (250 μL) three times, after which, the particles spontaneously adhere to the walls of the plastic centrifuge tubes. For XRD sample preparation, the purified samples are re-dispersed into toluene and drop-cast onto a silicon wafer. Samples are also re-dispersed into 250 μL dodecane for characterization in dispersion with SAXS, and then diluted into hexanes 10-fold for UV-vis spectroscopy, 1000-fold for PL spectroscopy, and 100-fold for TEM.

UV-Visible (UV-vis) Absorbance and Photoluminescence (PL) Spectroscopy

Both UV-vis and PL spectroscopy are performed using quartz cuvettes with a 1 cm pathlength. UV-vis spectroscopy is performed using a Thermo Scientific Evolution 300 (Waltham, MA USA) spectrophotometer operating over a 300-700 nm wavelength range. PL is performed using a Molecular Devices SpectraMax M5 (San Jose, CA USA) fluorescence spectrophotometer.

Transmission Electron Microscopy (TEM)

Bright field TEM is performed using FEI Tecnai G2 F20 Super-Twin (Hillsboro, OR) operating at 200 kV. Samples are deposited over a copper TEM grid with 300 mesh carbon from Electron Microscopy Sciences (Hatfield, PA USA) by drop casting 3 μL of sample and letting this dry.

Small-Angle X-ray Scattering (SAXS) and X-ray Diffraction (XRD)

SAXS is performed using Anton-Parr SAXSess (Graz, Austria) Kratky camera in a line-collimation (0.26 Å smearing) configuration with Cu K-α radiation. Samples are mounted using quartz capillaries of 1 mm in diameter. X-ray scattering is collected using a Fujifilm phosphor image plate (Japan) that is then developed in a PerkinElmer Cyclone Plus plate reader (Waltham, MA USA). The 2D raw data is converted to a 1D profile and subsequently corrected by subtraction of the scattering from the solvent and from the empty capillary. Absolute scaling of SAXS intensity is performed using water standard.[12] XRD is performed using Bruker D8 Discover Microfocus (Billerica, MA) using a beam that has been collimated to a 1 mm cross-section with Cu K-α radiation. X-ray diffraction spectra ares collected using Pilatus 3R 100KA 2D detector. The 2D raw data is then converted to a 1D profile and subsequently corrected by subtracting the broad background signal.

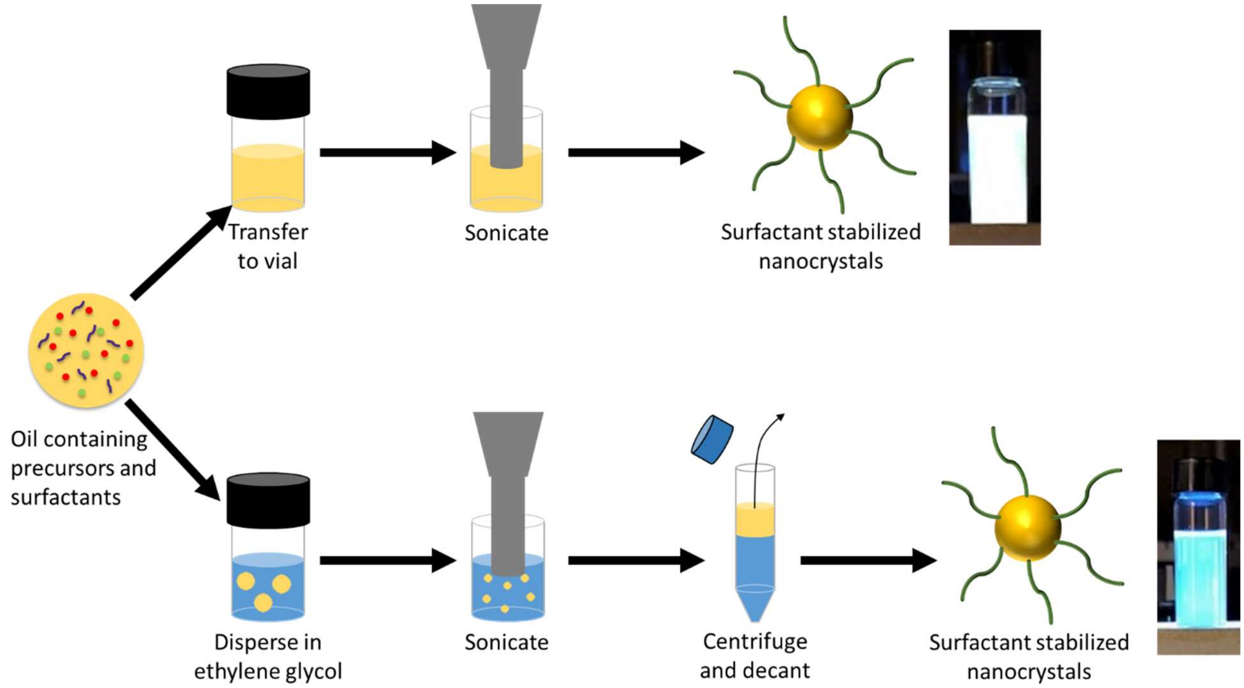

Figure 3.1: Schematic of the particle synthesis, along with photos of the final products under UV light.

3.3 RESULTS AND DISCUSSION

To determine the total acoustic power that is delivered to the system, calorimetry was performed, as devised by Kikuchi and Uchida,[13] using water in an insulated environment at the same sonication horn parameters that were used for QD synthesis. Details of the calorimetry experiment is provided in the supplemental information. Previous sonochemical synthesis of CdSe QDs has shown that particle growth kinetics can be controlled by tuning the ultrasound power;[14] however, it remained unclear if the faster kinetics were due to increased ultrasound cavitation intensity or simply due to the systematic rise in the bulk temperature of the reaction mixture as sonication proceeded. In fact, since no temperature control was implemented in that system, the reaction temperature was observed to rise as high as 200°C, which is close to the typical temperature used in hot-injection or solvothermal methods for CdSe synthesis.[9,15] In this work, the power delivered by the ultrasound horn was set to 12.6 W for all syntheses. At this power, the reaction temperature stabilizes at a steady-state of 55°C in the single-phase system and 65°C in the emulsion system. Notably, both of these temperatures are significantly lower than what is typically necessary for either a hot-injection or solvothermal CdSe NC synthesis. Examples of temperature profiles as a function of time are provided in the supplemental information for each reaction (Figure 3.11). To ensure that QD formation is due to ultrasound, and not due to the mild rise in temperature, a control experiment was performed where the reaction mixture was heated to 60°C on a hot plate. As would be expected, UV-vis absorbance measurements did not show any changes or QD formation, even after 3 hours of heating (Figure 3.12, Supplemental Information).

In our experiments, both the single-phase and emulsion systems were sonicated and tracked for a total of 3 hours. Aliquots of the sample were taken at several time points to monitor QD growth as a function of sonication time. Figure 3.2 and Figure 3.4 show UV-vis absorbance and photoluminescence (PL) spectra of the single-phase and emulsion systems, respectively, after purification. UV-vis absorbance spectra were also taken before and after QD purification. Although absorbance and PL spectra carry rich information regarding the QDs, including the clear formation of a $1S_{3/2}1S_e$ excitonic absorption feature and the associated band-edge luminescence, they also exhibit broad surface-state emission, which can be influenced by a variety of factors including the ligands present on the surface of the QDs.[16–20] In order to characterize the structure of the QD, small-angle X-ray scattering (SAXS) was also performed (Figure 3.3 & Figure 3.5) as a function of sonication time. In addition, SAXS was also performed before and after sample purification to gain a more complete picture of the changes that occur during the synthesis and purification processes. After each sonochemical synthesis was completed, the samples were also characterized by X-ray diffraction (XRD) and transmission electron microscopy (TEM).

As the precursor mixtures were sonicated in the single-phase and emulsion-based systems, particles were observed to form and steadily grow with longer sonication time. In the single-phase system, the first excitonic peak in the absorbance spectra (Figure 3.2a) was observed to red-shift along with the band-edge luminescence (Figure 3.2b) as sonication times increased, indicating gradual growth of the QDs. Using the position of the $1S_{3/2}1S_e$ excitonic absorbance peak,[21] the QD diameter was estimated as a function of time, growing from a diameter of approximately 1.74 nm after 30 minutes of sonication to 1.91 nm after 180 minutes of sonication. In addition to band-edge luminescence, all PL spectra exhibited broad emission at higher wavelengths throughout the visible frequency regime due to the presence of surface states, which are commonly observed for ultrasmall QDs.[22–24]

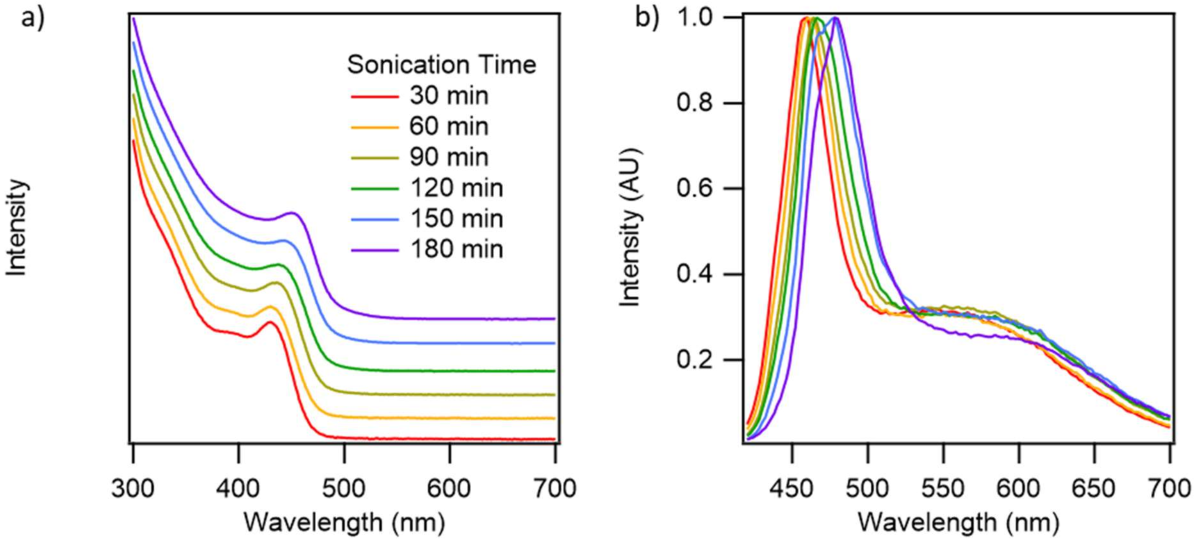

Figure 3.2: a) Absorbance and b) PL spectra (λ_{exc} = 360 nm) of CdSe QDs synthesized via sonication in the single-phase solvent system.

SAXS characterization of the particle dispersions further confirms the growth of ultra-small QDs with increasing time (Figure 3.3). In SAXS, the scattering intensity profile is related to the square of the Fourier transform of the spatial correlation function of electrons in the sample.

The intensity is typically plotted against the scattering wave vector, q, which is dependent on the scattering angle and the X-ray energy or wavelength. Longer spatial correlations appear as features at lower q values, while shorter correlations appear as features at high q. Figure 3.3a shows the scattering profiles for the single-phase samples as synthesized, prior to cleaning and purification. The data is presented after normalization to an absolute intensity,[12] which allows for direct correlation of SAXS intensity to the concentration of QDs in dispersion.

Notably, prior to the start of the reaction, there is already a scattering profile that arises due to the formation of inverse micelles in the precursor solutions.[25] At longer sonication times, scattering contributions from the CdSe QDs start to dominate the signal. This is especially evident at low q, where a second low-q Guinier 'hump' is observed in addition to that found for the precursors prior to sonication. After cleaning the samples, the scattering from the inverse micelles in the precursor is no longer observed, and only a single Guinier turnover is observed at low q (Figure 3.3b). The scattering profiles of purified and 'cleaned' samples are no longer placed in an absolute scale because there is an inevitable loss of product that is associated with the cleaning process, and the intensities of each profile can no longer be directly compared to one another. Nevertheless, the shape of the scattering profiles only depends on the geometry of the QDs and, under sufficiently dilute conditions, should be independent of the QD concentration. In Figure 3.3b, the scattering intensities are arbitrarily scaled such that the intensity is matched at high q for qualitative comparison of their shape. As sonication proceeds, the Guinier region shifts toward lower q values, indicating the formation of larger particles. Using the Irena software tool suite,[26] the scattering profiles were fit to a model to extract the QD size. Scattering fits are also provided in the supplemental information. The mean diameter of the QDs grows from 2.43 nm after 30 minutes of sonication to 2.58 nm after 180 minutes of sonication (Figure 3.3c inset). The size determined from SAXS is larger when compared to the size calculated from UV-vis absorption features because the head groups of stabilizing ligands that are adsorbed to the surface of the QDs can also contribute to the SAXS signal due to their electron density.

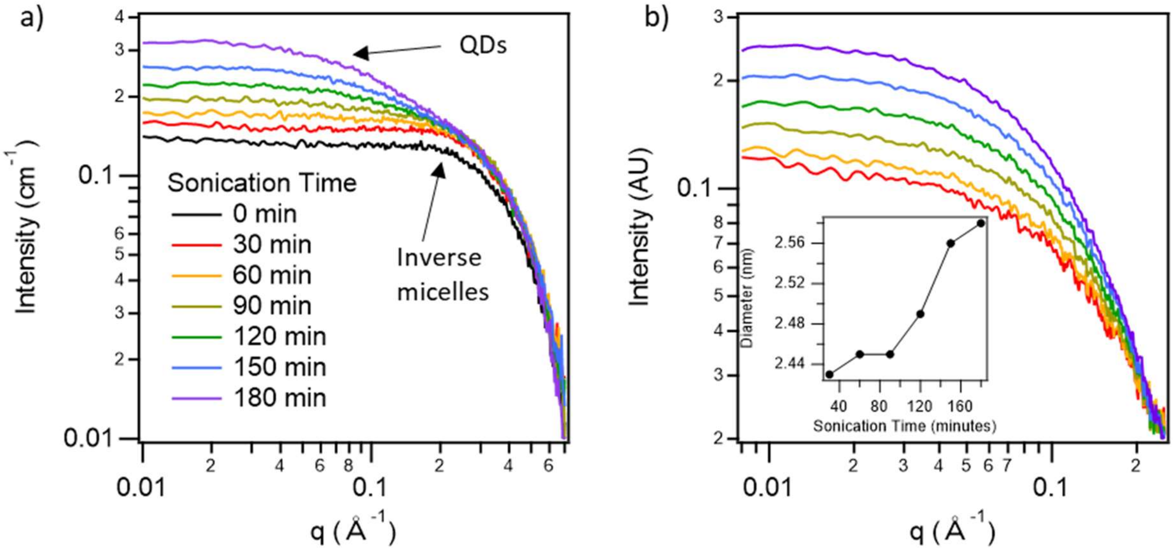

Figure 3.3: a) Absolute-scale SAXS profiles of CdSe QDs synthesized via sonication of the single-phase solvent system prior to cleaning and purification. Arrows indicate the two features that correspond to inverse micelles and QDs. b) Arbitrary-scale SAXS profiles after, with an inset showing the diameter of the QDs extracted from model fitting.

In stark contrast to the above results, when sonochemical QD syntheses are performed in emulsion systems, the results are drastically different. While sonication of the single-phase system produces ultrasmall QDs, sonication of the emulsion-based system produces QDs with well-defined discrete sizes, which are commonly known as magic-sized clusters (MSCs). As the sample is sonicated, no shift of the first excitonic peak is observed in the UV-vis absorbance spectra. Instead, an extremely sharp absorbance peak is observed at 425 nm (fwhm ≈ 100 meV) that does not shift with increasing sonication time, but does increase in intensity (Figure 3.4a). These samples also exhibits broad, ‘white-light’ emission but with no characteristic band-edge luminescence peak. Such a sharp absorbance peak coupled with broad surface-state emission, but no band-edge luminescence is strongly characteristic of MSCs.[6,22,27–29] In particular, the absorption peak at this wavelength corresponds well to the known $(CdSe)_{33}$ and $(CdSe)_{34}$ MSCs.[30] Interestingly, the relative height of the peak at 425 nm starts to decrease after 90 minutes of sonication, and an absorption tail starts to appear. This turning point at 120 minutes is also observed in the PL spectra (Figure 3.4b). Up until 90 minutes of sonication, the luminescence is almost entirely characteristic of surface-state emission. However, at ~120 minutes of sonication, a peak starts to develop that blue-shifts with longer sonication time, bearing resemblance of a band-edge luminescence peak. The formation of a tail in the UV-vis spectra and a peak in the PL spectra suggests the formation of larger QDs is taking place after extensive sonication.

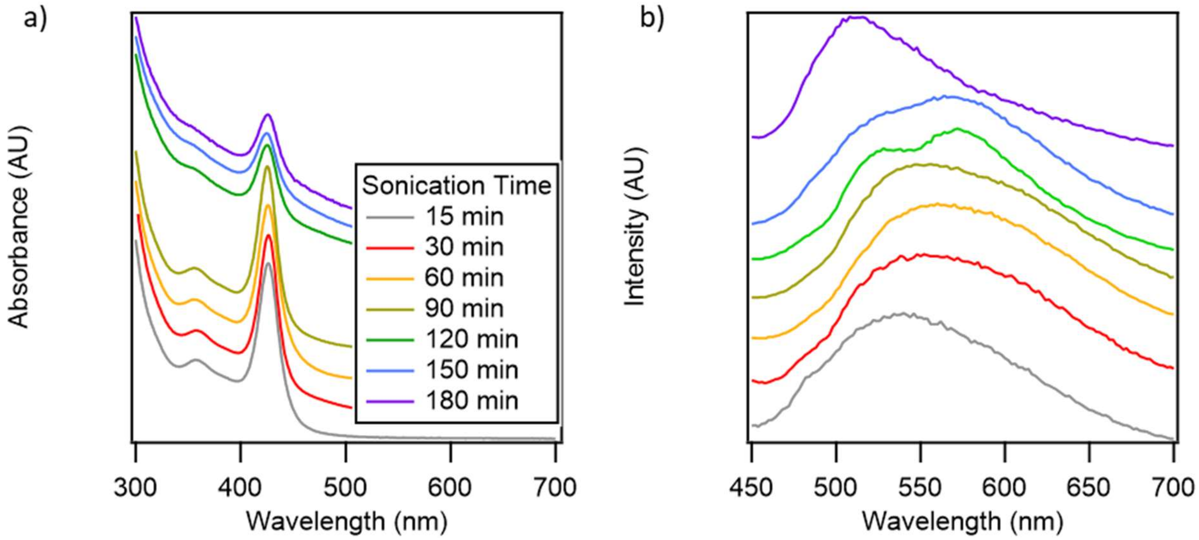

Figure 3.4: a) Absorbance and b) PL spectra (λ_{exc} = 420 nm) of cleaned CdSe particles synthesized using sonication in emulsion systems as a function of sonication time.

SAXS was also performed both before and after purification of the emulsion system samples (Figure 3.5). Similar to the single-phase system, the SAXS data for the emulsion-based system was transformed to an absolute scale for the as-prepared samples (Figure 3.5a). The scattering intensity increases steadily with longer sonication time, indicating that the volume fraction of particles increases with sonication time. The Guinier hump near 0.2 Å^{-1} is related to the primary particles, *viz.* CdSe QDs, and the continued rise in intensity toward low q suggests that the particles are associating to create large-scale structures. The intensity continues to rise even at the lowest q values, which means that the size of the aggregates lies beyond the resolution of the SAXS instrument. The samples were subsequently diluted 10-fold, purified, and SAXS was performed again on the 'cleaned' samples in the absence of excess molecular precursors (Figure 3.5b). Similar to Figure 3.3a, these SAXS profiles are not placed in an absolute scale since there are some material losses that occur during the purification process. Instead, the scattering profiles were normalized to have matching intensities at high values of q. Even after purification and a 10-fold dilution, the large flocculates continued to persist, as evidenced by the continued rise in intensity at low q. Interestingly, the profiles overlap until after 120 minutes, which matches well with the turning point of the UV-vis spectra, when the intensity of the sharp absorbance feature begins to decrease (Figure 3.4a). This indicates that the rise in volume fraction with sonication time (Figure 3.5a) up to 120 minutes is not due to QD size increases, but rather to an increase in the total quantity of MSCs. To further extract structural information, we fit the scattering profiles of the cleaned samples, up to 90 minutes of sonication, to a model of fractal aggregates of spherical primary particles.[31] From this model, we obtain a primary particle radius of 7.3 Å that is consistent with the size found by Kasuya *et al.* for MSCs.[30] The primary particles then form aggregates with a fractal dimension of 1.3, corresponding to a low-density aggregate. Details of the SAXS models and fits are provided in the supplemental information. After 120 minutes, the SAXS profile supports the conclusion that larger QDs are formed, which is most evident in the SAXS profile at 180 minutes (Figure 3.5b). The feature at 0.2 Å^{-1} that corresponds to the MSCs is still present, but another feature at 0.1 Å^{-1} emerges that corresponds to larger QDs.

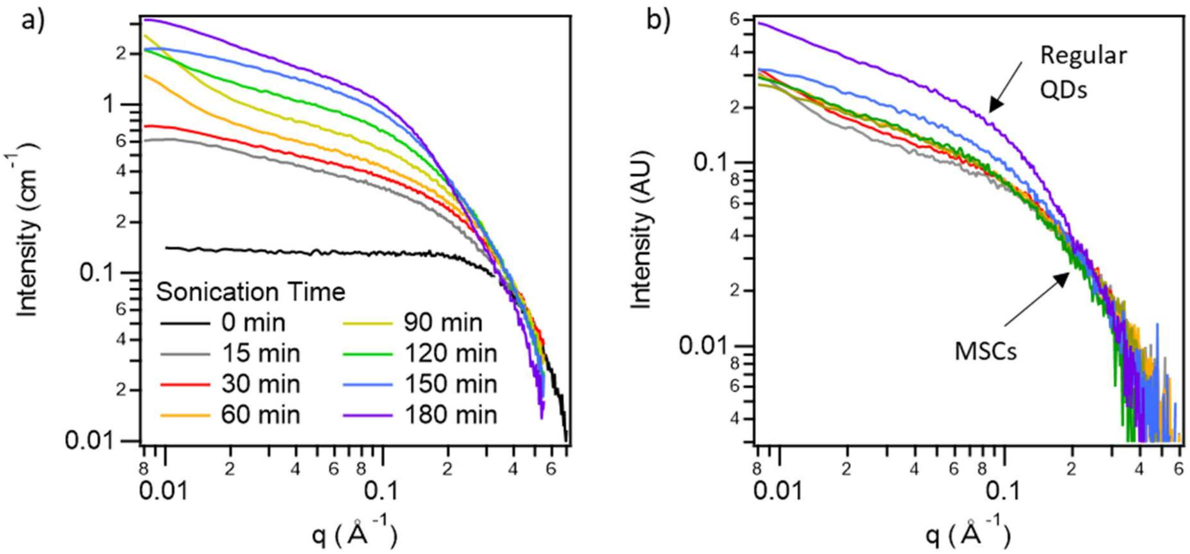

Figure 3.5: SAXS profiles for CdSe particles synthesized with sonication in an emulsion-based system. a) As-prepared samples (*i.e.* before cleaning and purification) in absolute scale units and b) samples after purification in an arbitrary intensity scale. Arrows indicate the two features that correspond to MSCs and regular QDs.

After 3 hours of sonication, samples from both the single-phase and emulsion systems were also purified and characterized by XRD (Figure 3.6) and TEM (Figure 3.7). The XRD data exhibits significant peak broadening due to the small size of the QDs produced in both the single-phase and emulsion-based synthesis systems. The XRD profile for the sample from the single-phase system matches that of cubic zincblende CdSe (PDF 04-003-6493, Figure 3.6a). However, care must be taken because since such significant peak broadening cannot decisively differentiate between the cubic zincblende and hexagonal wurtzite structures.[6,32,33] The excess signal at low angles is likely due to the remaining ligands in the sample. The diffraction peaks of the material produced from the emulsion system are even broader (Figure 3.6b) because of the even smaller QD sizes. Notably, MSCs have nearly 80% of their atoms on the surface, which leaves only two unit cells in the core of the particles,[22,23] with the observed peaks at 27° and 45° corresponding very closely to what has been seen with previous XRD characterization of CdSe and CdS MSCs.[34,35]

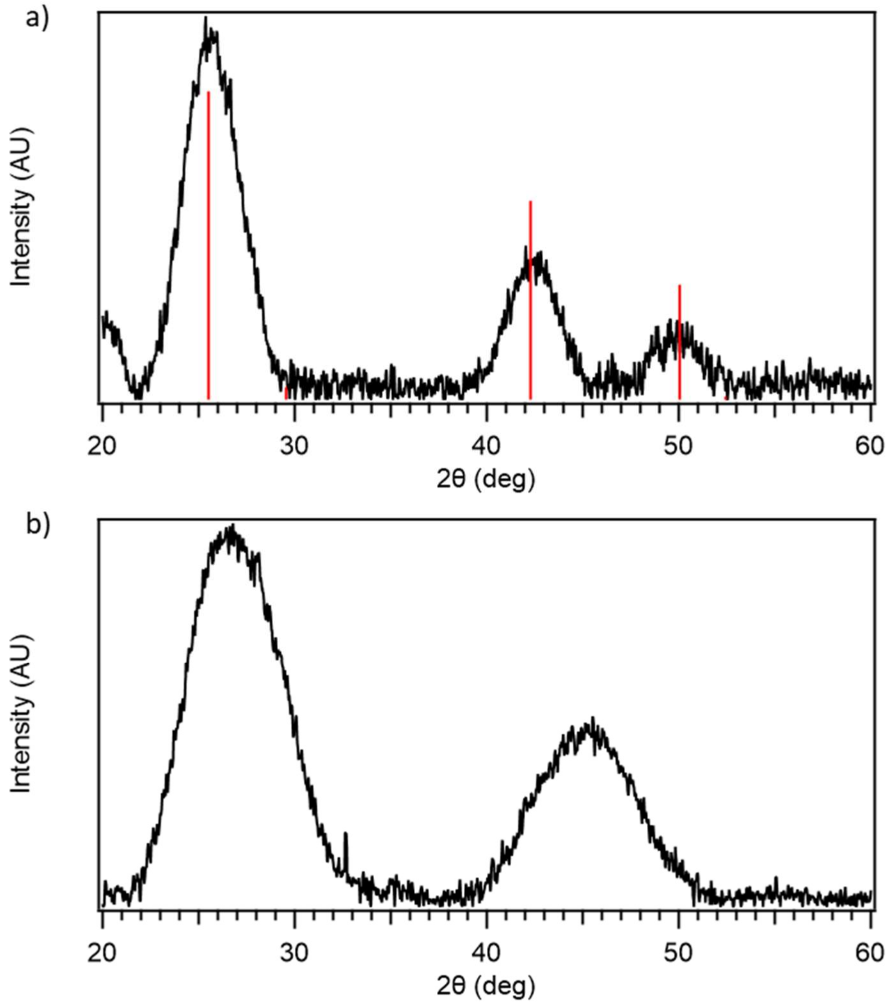

Figure 3.6: XRD spectra of CdSe particles synthesized via sonication in a) single-phase and b) emulsion-based systems. Red lines represent the expected peak positions for the bulk zincblende CdSe structure.

Figure 3.7 shows TEM images of the QDs produced via 180 minutes of sonication for both processes. The contrast in the TEM images is very limited due to the small size of the QDs; nonetheless, the QDs observed from the end-point of the three-hour emulsion-based synthesis are larger than would be expected for MSCs, which supports the data discussed above that suggested the formation of larger QDs after extensive sonication. These particles are also larger in size than what was determined from the SAXS profiles after 30 minutes of sonication, further supporting the idea that MSCs are converted into regular-sized QDs after prolonged sonication in emulsions. Given the vanishingly low contrast associated with ultrasmall QDs, it was not possible to directly image the MSCs using TEM.

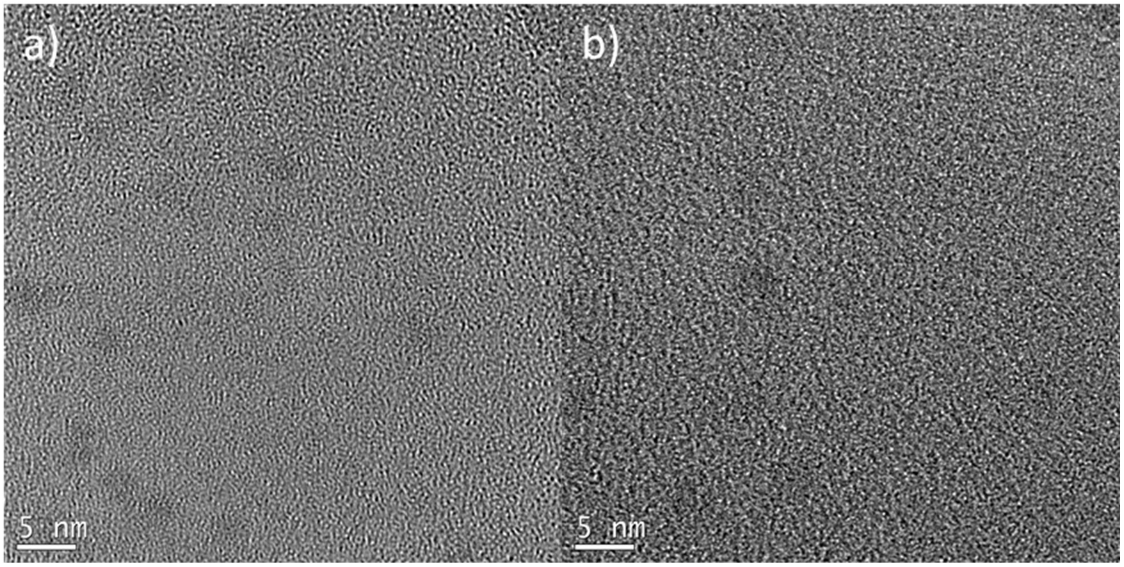

Figure 3.7: CdSe nanoparticles formed after 180 minutes of sonication in a) single-phase, and b) emulsion-based systems.

It is important to note that MSCs and ultrasmall QDs are distinct, both in terms of their electronic structure and growth process. While ultrasmall QDs are simply small-sized QDs, MSCs exhibit an electronic structure at the interface between that of a molecule and an inorganic particle, with a specific molecular structure and precisely defined number of atoms that result in a precise electronic excitation that leads to a sharp absorbance peak. Furthermore, since the number of atoms that gives rise to a stable MSC is also precisely defined, MSCs do not grow in a continuous fashion, but rather they transition from one allowed configuration to another. The result is that absorbance peaks do not gradually move or shift, as is the case with regular QDs, but rather they ‘jump’ from one discrete wavelength to another. In this work, the only family of MSCs that was observed corresponds to $(CdSe)_{33}$ and $(CdSe)_{34}$. However, it should be noted that numerous other works have successfully synthesized many other families of CdSe MSCs.[28,36]

Interestingly, in the UV-vis spectra of the samples obtained from the emulsion-based synthesis (Figure 3.4a), the shrinking of the absorption peak centered at 425 nm is not just relative, but absolute. Prior to purification, the absorbance peak was slightly shifted to 420 nm (Figure 3.13), likely due to a difference in ligand coordination to the MSC before and after purification. Quantitative tracking of the absorbance at 420 nm with increased sonication time (Figure 3.8a) shows that the absorbance at 420 nm continues to rise without any shift in wavelength, even after about 120 minutes of sonication, suggesting that the number of MSCs in the system is increasing as the sample is sonicated. Afterward, however, the absorbance at 420 nm decreases and an absorption tail at longer wavelengths emerges. This coincides with the appearance of a second Guinier region in the SAXS profile after 150 minutes of sonication (Figure 3.5b), suggesting that the regular QDs are synthesized at the expense of the MSCs. In other words, the regular QDs are not side products of the sonochemical reaction; instead, QDs are formed from subsequent reactions of MSCs after they are produce. If only MSCs are desired, then the sonication process can be stopped at an appropriate time.

Aside from the difference in product properties, the rate of conversion from precursor to QDs is remarkably faster in the emulsion-based systems. This is evident from the absolute-scale SAXS profiles of the samples measured prior to cleaning. Comparing the samples from the single-phase systems (Figure 3.3a) to the emulsion systems (Figure 3.5a), the scattering intensity is much higher in the emulsion-based syntheses. In addition, when performing dilutions for UV-vis spectroscopy, the single-phase system samples needed to be diluted 10-fold to get sufficient light penetration through the samples, while the samples from the emulsion systems needed to be diluted more than 100-fold. To further quantify the rate of reaction for the QD and MSC syntheses, the absorption spectra were converted to an energy scale, and then integrated from 1.77 eV to 3.82 eV (325 nm - 700 nm). Since the integral of the absorption coefficient over the photon energy (*i.e.* $\int \alpha \, dE$) has a negligible size dependence,[21] the integral of absorbance over energy (*i.e.* $\int A \, dE$) can be used to quantify the conversion of Cd and Se precursors into CdSe units across different QD ensembles (Figure 3.8b). Details and cross-validation of this calculation are given in the supplemental information. After 3 hours of sonication, complete conversion was observed in the emulsion system, while only 11% conversion was observed in the single-phase system. Using a linear fit, the rates of conversion in the emulsion system and in the single-phase system were found to be 3.8 $g \cdot L^{-1} hr^{-1}$ and 0.48 $g \cdot L^{-1} hr^{-1}$, respectively, where the conversion rate of the former is comparable to that of a typical hot-injection synthesis of CdSe QDs.[37,38] For example, an optimized hot-injection synthesis of CdSe QDs yields about 3.7 g/L, and it takes approximately one hour, including the initial heating of the reaction mixture.[39] Thus, sonication in the emulsion system provides a competitive conversion rate for the synthesis of CdSe. Moreover, this rate can likely be further increased by delivering more ultrasound power, using larger volume fractions of oil, increasing precursor concentrations,[40] using a heterogenous selenium source,[41] and/or increasing the reaction temperature.

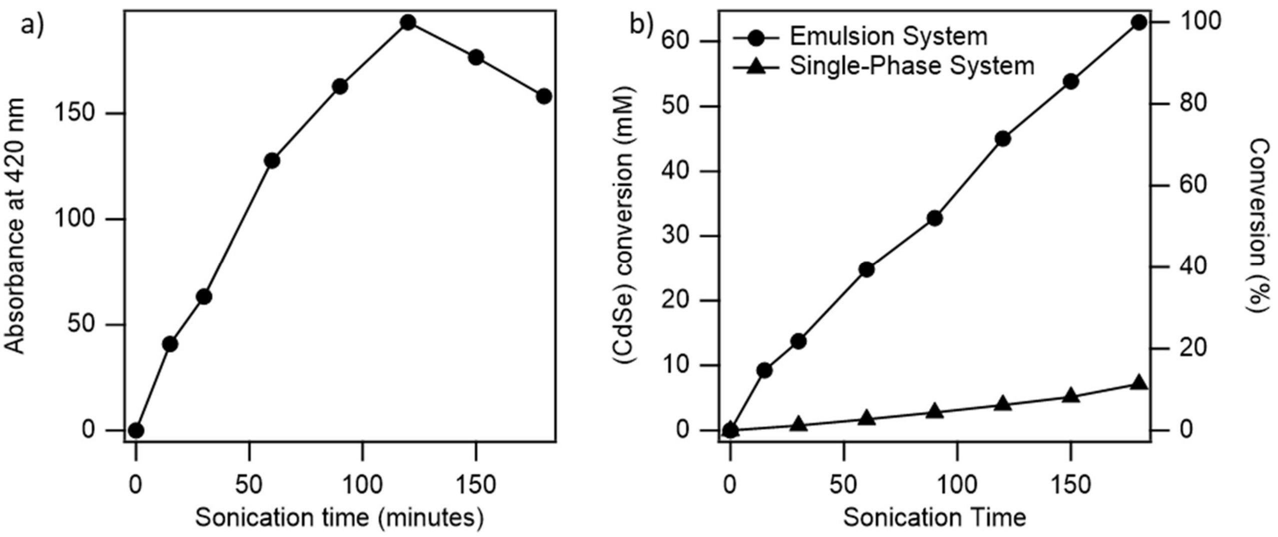

Figure 3.8: a) MSC absorbance at 420 nm in the emulsion system tracked as a function sonication time, and b) conversion of Cd and Se precursors into (CdSe) with sonication.

In addition, when using sonochemical synthesis methods, temporal control over when the reaction starts and stops is remarkable. In order to demonstrate this, an experiment where the sonication system was systematically turned ‘on’ and ‘off’ every 10 minutes was also performed with the emulsion-based synthesis. Once again, the absorbance at 420 nm was tracked as a function of elapsed time (Figure 3.9a). The data clearly shows that the absorbance increases only when the sonication is turned ‘on’, which results in a step-like growth curve. There are several important outcomes from this experiment that suggest that precise temporal control of the reaction can further elevate QD synthesis methods. First, this conclusively demonstrates that conversion of precursors to QDs is a direct result of ultrasound and not due to a rise in the temperature of the sample, which is a side effect of power dissipation during sonication. Although allowing the temperature to rise may increase QD production rates, such a precise level of temporal control may not be possible and it may also interfere with the selective formation of MSCs observed in the emulsion system. Second, the choice of using trioctylphosphine selenide (TOP:Se) as the chalcogen precursor, as opposed to more reactive secondary phosphine precursors such as diphenylphosphine selenide, is necessary to carefully control the sonochemical reactions. To note, there are several separate mechanisms for the formation of CdSe monomers.[42] One mechanism requires the decomposition of a tertiary phosphine-chalcogenide to form highly reactive H_2Se, while another mechanism does not involve precursor decomposition and instead is a direct reaction of secondary phosphine-chalcogenides and metal carboxylates. Since secondary phosphines are much more reactive than tertiary phosphines,[43,44] it has been shown that CdSe MSCs can be synthesized at temperatures as low as 45°C using diphenylphosphine selenide.[27] However, in this application, the low reactivity of TOP:Se prevents unwanted reactions from progressing uncontrollably at low temperatures. The extreme conditions that are locally exhibited by cavitation are more than sufficient to decompose TOP:Se and drive the conversion of CdSe QDs and MSCs. These design choices open the door towards efficient, on-demand synthesis of QDs, where the reaction can be started and stopped simply by turning the ultrasound on and off. Moreover, secondary phosphines are typically extremely pyrophoric; using TOP:Se allows for the synthesis of QDs without the safety risks associated with such highly reactive precursors. Finally, high-intensity focused ultrasound (HIFU) could also be used to spatially control the synthesis of QDs and MSCs in specific locations.

Two questions remain to be answered: 1) compared to the single-phase system, why is precursor conversion so much faster in the emulsion-based system and 2) why are the resulting products different? The answers to these questions are related. The synthesis of QDs is driven by the extreme conditions induced locally by cavitation. In the single-phase system, bubbles must nucleate homogenously, which is terribly inefficient. In such cases, cavitation tends to occur predominantly at interfaces such as the vial walls and the surface of the sonication horn. In the emulsion systems, the liquid-liquid interface of the droplets act as heterogenous nucleation sites for bubbles, which is much more favorable than homogenous nucleation.[45] These 'weak spots' in the system have been reasoned previously,[46] although no control experiment in a single-phase bulk system was performed. Moreover, the cavitation bubbles are generated exactly where they are needed, with the sonication energy dissipated locally where the precursor materials are also located (*i.e.* in the droplets). Hence sonication of the emulsion system results in more frequent and numerous cavitation events that are more efficiently distributed near the precursors, quickly driving nucleation and growth of the QDs (Figure 3.9b). This also explains why sonication in the emulsion system results in hotter mixture temperatures than those observed in the single-phase system, even at the same sonication power setting. Coincidentally, the liquid-liquid interface may also serve as a nucleation site for QDs, and it is well known that the energy barrier for heterogenous nucleation is lower than that of homogenous nucleation of QDs.[9]

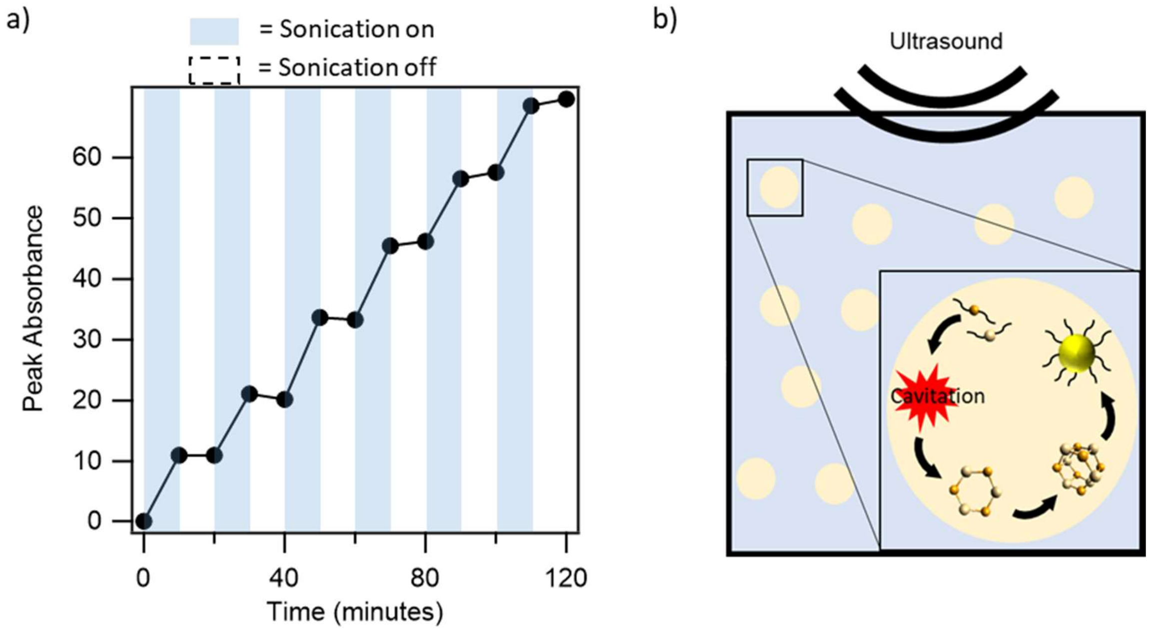

Figure 3.9: a) Quantitative absorbance at 420 nm of CdSe MSCs synthesized in the emulsion system with periodic 10-minute on-off cycles. Blue shades indicate the time period during which sonication is active. b) Schematic of the sonochemical QD synthesis mechanism, where cavitation provides the energy required for precursors to react, form clusters, and grow into QDs.

The high precursor concentration and fast conversion is key to the synthesis of MSCs in the emulsion system. Nevers *et al.* demonstrated that mixtures with high precursor concentrations offer a well-defined pathway towards synthesizing MSCs, and that the MSCs are stable and resistant towards growth and dissolution.[47] This is because the MSCs and their ligands form inorganic-organic fibers that, in turn, create ordered mesophases that stabilize the clusters against aggregation.[47] They found that the stability of the MSCs is specifically due to the formation of fibers, rather the assembled mesophases. In this work, the lack of sharp peaks in the SAXS profiles (Figure 3.5) suggests that highly ordered mesophases are not created. However, the low fractal dimension of the aggregates ($D_f = 1.3$) does suggest that the MSC aggregates form a nearly linear structure resembling that of a fiber, and this seems sufficient to keep the MSCs stable.

However, instability of the MSCs is evident when samples containing aggregates are diluted, which causes the aggregates to unbundle into individual MSCs. When a diluted sample is left for 36 hours at room temperature, the sharp peak at 420 nm is almost completely quenched, and a broad peak emerges (Figure 3.10a) at lower energies, indicating the formation of regular QDs. The same phenomenon is observed even with samples that are purified, indicating that these regular QDs are, at least in part, a result of Ostwald ripening. On the other hand, the stability of the MSCs when they are in an aggregated state is remarkable. If a sample is kept in its original higher concentration for a month, its UV-vis spectra shows no apparent change.

The apparent instability of the MSCs may also explain the decrease in MSC concentration after prolonged sonication in the emulsion system (Figure 3.8a). The creation of MSCs is discussed as the result of the extreme temperature and pressure exhibited by cavitation. Cavitation also evokes high velocity microjets[45] that may dislodge MSCs from their bundles, which could then dissolve or grow into regular QDs. Therefore, there are two competing processes with respect to MSC concentration. Toward the beginning of the sonication process, the system is rich in molecular precursors, and the rate of MSC creation is much faster than the rate dislodging. Conversely, toward the end of the process, the dislodging of MSCs dominates due to the higher concentration of MSC aggregates and lower concentration of precursors.

In the case of single-phase reaction system, the resultant ultra-small QDs may also go through MSC intermediates. Evidence of this can be found in the UV-vis spectra of the as-synthesized samples from the single-phase system (Figure 3.10b). Multiple peaks can clearly be seen, resembling the UV-vis spectra of smaller MSCs[28,48] at earlier sonication times and looking more like the Ostwald ripened MSCs in Figure 3.10a at longer sonication times. Because the conversion is much slower in the single-phase system, aggregates of MSCs would not be formed because their concentration is low, and hence the MSCs would not be protected from growth and dissolution. Therefore, any MSCs that are formed undergo ripening very quickly, resulting in the regular QDs that are observed in the UV-vis spectra of the purified samples (Figure 3.2a). This contrasts with the emulsion-based system where the rapid conversion to concentrated MSCs allow for aggregation and stabilization without becoming regular QDs.

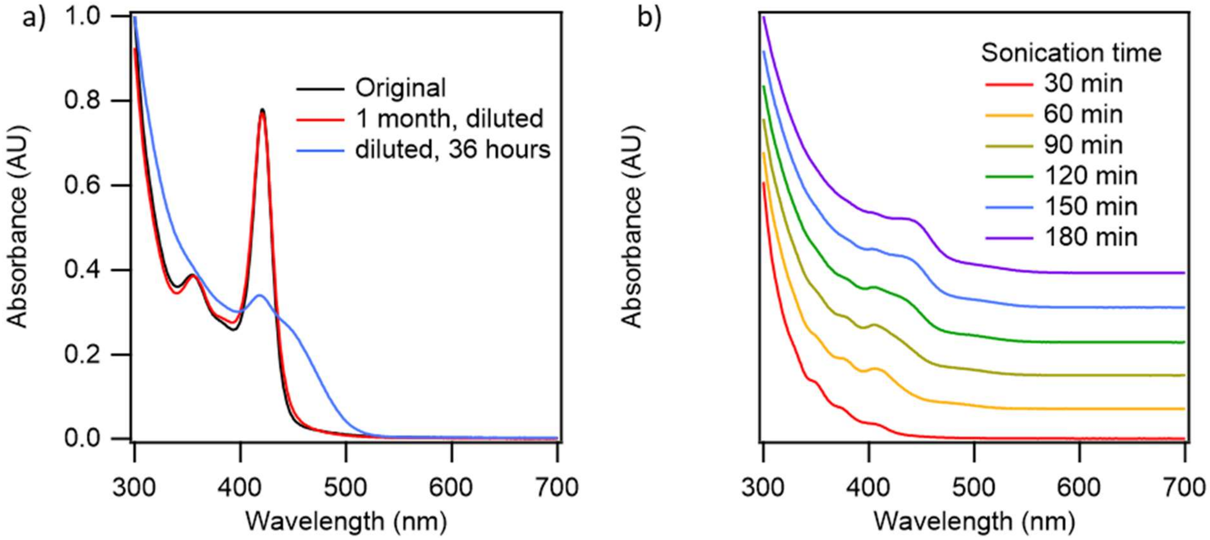

Figure 3.10: a) UV-vis absorbance spectra showing the growth and dissolution of MSCs when they do not form large aggregates. b) UV-vis spectra of as-synthesized samples from the single-phase system collected after different sonication times.

3.4 CONCLUSION

Sonochemical synthesis of CdSe QDs was performed in a single-phase and an emulsion-based system, while keeping the bulk sample temperatures low (< 70°C). Conversion of precursors into QDs is much faster in emulsion systems because the liquid-liquid interface serves as heterogenous nucleation sites for bubbles which leads to more frequent and more effective cavitation events to drive the reactions. In emulsion systems, MSCs, $(CdSe)_{33}$ and $(CdSe)_{34}$, were synthesized, although prolonged sonication beyond 120 minutes does also lead to the formation of regular QDs. In addition to ligand-based stabilization, the MSCs are stabilized *via* the formation of extended inorganic-organic aggregates, which are enabled by the rapid rise in MSC concentration in the emulsion-based system. Unbundling of these aggregates by dilution destabilizes the MSCs, resulting in dissolution and growth of MSCs into regular QDs. In the single-phase bulk synthesis systems, evidence suggests that MSCs are created as intermediates to QD synthesis; however, because the reaction rate is slow, the MSC concentration is too low to form stable aggregates, and instead, they undergo Ostwald ripening to form regular QDs. Controlled, on-demand synthesis of CdSe QDs is also demonstrated by simply turning the ultrasound 'on' and 'off' at any arbitrary rate. The rate of QD production in the emulsion system was found to be 3.8 $g\cdot L^{-1}hr^{-1}$ with complete conversion of precursors, which is much faster than that in the single-phase system (0.48 g/L hr) and is comparable to that of the typical hot-injection QD synthesis, and can likely be further optimized. Letting the temperature rise higher may speed up QD production, but likely at the cost of a loss in temporal reaction control. Finally, although this work focuses on CdSe QDs, there are no theoretical limitations that would prevent the synthesis of other types of QDs. Future work will involve more detailed characterization of these CdSe QDs, along with other types of semiconductor materials.

3.5 SUPPORTING INFORMATION

Calorimetry

To measure the actual power output from the sonication horn, calorimetry was performed based on the method developed by Kikuchi and Uchida.[13] A 60 mL glass vial is put into a large enough Styrofoam box such that the vial is entirely inside the box. The gaps between the box and the vial is filled with foam sealant to insulate the vial. Enough foam sealant is used such that the foam is beyond the height of the vial, but not covering the mouth of the vial. The vial is filled with 50 mL of water, and the sonication horn and a thermocouple are immersed in the water. The sonication is turned on, and the temperature is tracked with time. Assuming a constant heat capacity of water, the energy delivered to the water is calculated.

Temperature profile of the mixture with sonication

The temperature inside the reaction vessel was measured by using a thermocouple embedded directly inside the mixture. As explained in the main manuscript the temperature of the emulsion system is higher than that of the single-phase system because there are more cavitation events in the emulsion system. The liquid-liquid interface between ethylene glycol and octadecene act as heterogeneous nucleation site for bubbles. The temperature of the emulsion system starts to go down after 90 minutes of sonication. This is likely due to the decrease of the oil phase as aliquots are taken out, resulting in overall less liquid-liquid interface and therefore less total number of cavitation events as well.

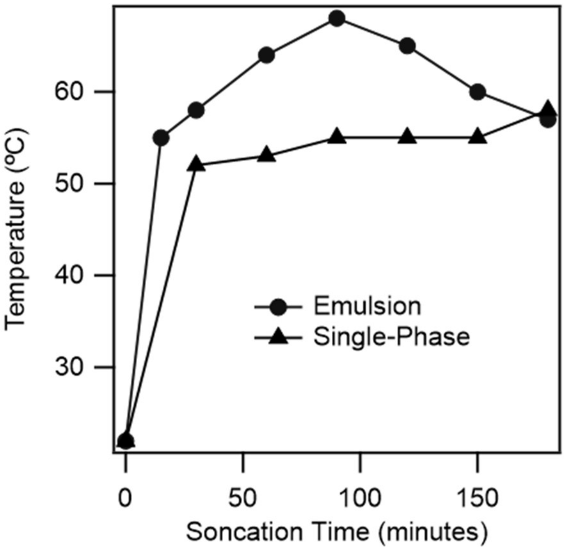

Figure 3.11: Temperature of the mixture tracked with sonication time.

Control sample using a hot plate

To ensure that particle formation is due to ultrasound and not temperature, a mixture with an identical recipe was heated on a hot plate while stirred for 3 hours. No change was observed in the spectra, indicating that no QDs were formed.

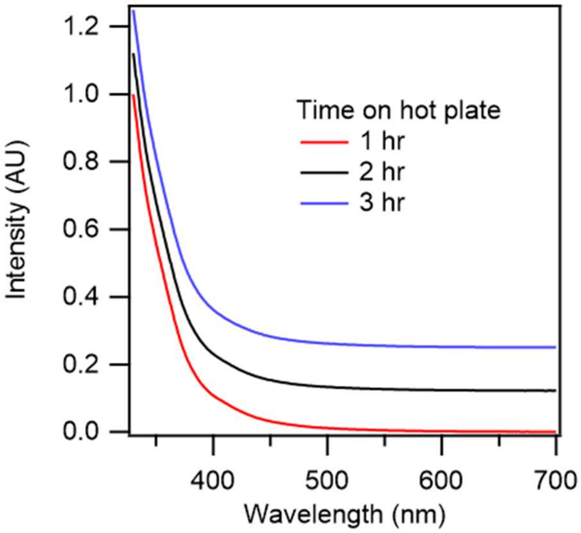

Figure 3.12: UV-Vis spectra of a mixture with an identical recipe to those used in sonication.

As-synthesized UV-Vis spectra of samples from emulsion system

The UV-Vis spectra of samples from the emulsion system before cleaning is shown in Figure 3.13. These spectra are almost identical to those after cleaning. One notable difference is that the sharp peak of the pre-cleaned samples is centered at 420, while that of the cleaned samples is at 425 nm. This difference is likely due to a difference in ligand population on the surface of the QDs.

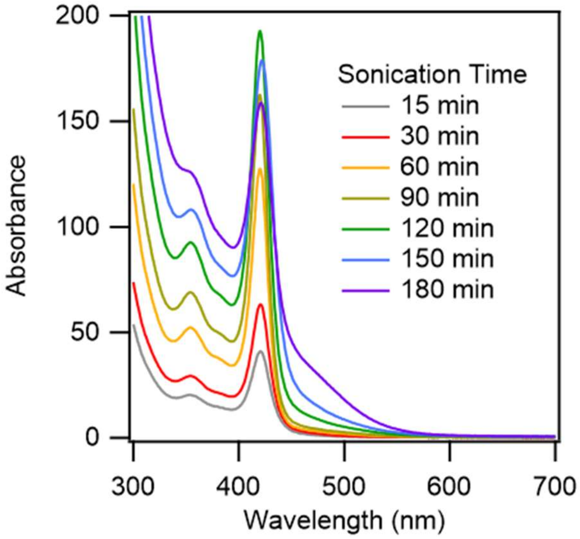

Figure 3.13: UV-Vis spectra of samples from the emulsion system before cleaning

MSC SAXS Data Model Fit

Fitting of MSC SAXS data was performed using SasView, a software to analyze small angle scattering data. The data was fit to the fractal model,[31] which calculates the scattering intensity from aggregates of spheres:

$$I(q) = \phi V\left(\rho_p - \rho_s\right)^2 P(q)S(q) + \text{background} \tag{3.1}$$

where ϕ is the volume fraction of particles, V is the volume of a single particle, ρ_p is the scattering length density of the particle, ρ_s is the scattering length density of the solvent. $P(q)$ and $S(q)$ are the form factor of a sphere and structure factor, respectively, and are defined as

$$P(q) = \left[\frac{3(\sin(qR) - qR\sin(qR)}{(qR)^3}\right]^2 \tag{3.2}$$

$$S(q) = 1 + \frac{D_f\Gamma(D_f - 1)}{\left[1 + \frac{1}{(q\xi)^2}\right]^{(D_f-1)/2}} \frac{\sin\left[(D_f - 1)\, tan^{-1}(q\xi)\right]}{(qR)^{D_f}} \tag{3.3}$$

where R is the particle radius, D_f is the fractal dimension, Γ is the gamma function, and ξ is the correlation length representing cluster size. When fitting, the volume fraction, particle radius, and fractal dimension were allowed to vary to fit the data. All other parameters were fixed. There is inevitable product loss during the QD purification process and therefore the intensity cannot be scaled to determine particle concentration. Hence, the fitted value of the volume fraction parameter is meaningless, and is only meant to arbitrarily scale model intensity to data intensity. Similarly, the values of scattering length densities are arbitrarily set since they only serve to scale the SAXS curve up and down in a log-log plot. The background is set to 0 because the solvent was subtracted. The correlation length is set to an arbitrarily large value of 10,000 Å since the continued rise in intensity at low-q means that the sizes of the aggregates are beyond the resolution of the SAXS instrument. Figure 3.14 shows the model fit to the SAXS data from the emulsion system after 30 minutes of sonication. The relevant parameters obtained are the particle radius and fractal dimension, which are 7.3 Å and 1.3, respectively.

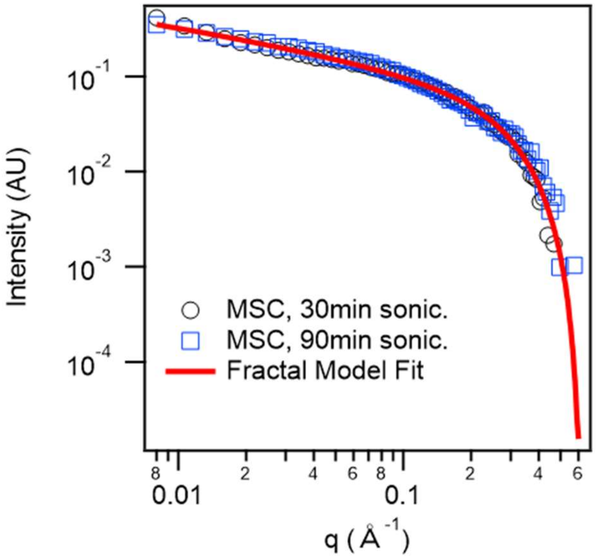

Figure 3.14: Comparison of SAXS profile of MSCs and a model fit using the fractal model.

SAXS fit of QDs synthesized in the single-phase bulk system

SAXS data was fitted to an ensemble of spherical particles using the Irena, a tool suite within Igor Pro software.[26]

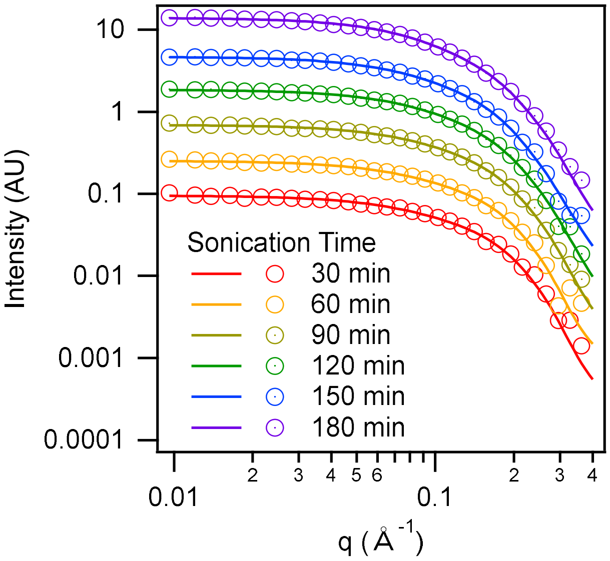

Figure 3.15: SAXS fitting of CdSe QDs synthesized in the single-phase bulk system.

CdSe conversion calculation

The linear absorption coefficient, $\alpha\ [=] cm^{-1}$, and the QD molar extinction coefficient, $\varepsilon\ [=] M^{-1}cm^{-1}$, are both a function of energy and can be related through

$$\varepsilon(E) = \frac{N_A V \times \alpha(E)}{1000 \times \ln(10)} \tag{3.4}$$

Where N_A is Avogadro's number and V is volume of a CdSe QD. For CdSe QDs in the size range of 2-8 nm, Jasieniak et al. showed that the oscillator strength across the spectra is simply redistributed across existing optical transitions.[21] In other words,

$$\int \alpha\, dE = constant \tag{3.5}$$

for any ensemble of CdSe QDs. This is especially convenient if the sample contains multiple populations of QDs with multiple overlapping peaks, such as the ones from the emulsion system at longer sonication times, and the size dependent extinction coefficient cannot be directly used.

First, we assume that for samples from the emulsion system, the sample up to sonication time of 90 minutes is exclusively composed of MSCs, and therefore we can obtain the concentration of QDs using Beer's law:

$$A = \varepsilon l C \tag{3.6}$$

where A is the absorbance, ε is the molar QD extinction coefficient, l is the path length, and C is the concentration. The value of ε is 1.60 x 10^5 M^{-1} cm^{-1}, calculated using the relation given by Jasieniak.[21] The concentration of (CdSe) cation-anion pair is obtained by multiplying the QD concentration by 33.5, since the absorption peak at 420 nm corresponds to MSCs $(CdSe)_{33}$ and $(CdSe)_{34}$.[30] The area under the UV-Vis spectra, $\int A\, dE$, is calculated by using the trapezoidal rule from the UV-Vis data. The area per (CdSe) cation-anion pair is then calculated by dividing the area by the (CdSe) concentration calculated directly from ε earlier.

$$\frac{Area}{(CdSe)} = B = \frac{\int A\, dE}{[(CdSe)]} \tag{3.7}$$

The value of B is averaged from sample from the emulsion system up to 90 minutes of sonication, since it was assumed that the sample only composed of MSCs up to this point. This value is then used with the area, $\int A\, dE$, to calculate the (CdSe) cation-anion pair concentration for all samples. A summary of this calculation is shown in Table 1S.

Table 3.1: Summary of the calculations used to determine the concentration of (CdSe).

Sonication Time	Absorbance at 420 nm	QD conc. (M)	[1](CdSe) conc. (M)	Area	B (M^{-1})	[2](CdSe) conc. (M)	[3](CdSe) conc. (M)
15	4.10E+01	2.56E-04	8.59E-03	1.93E+01	2.25E+03	9.24E-03	7.65E-03
30	6.32E+01	3.96E-04	1.33E-02	2.87E+01	2.17E+03	1.37E-02	1.18E-02
60	1.28E+02	7.99E-04	2.68E-02	5.19E+01	1.94E+03	2.48E-02	2.38E-02
90	1.63E+02	1.02E-03	3.41E-02	6.85E+01	2.01E+03	3.28E-02	3.04E-02
120	1.93E+02			9.41E+01		4.50E-02	
150	1.76E+02			1.13E+02		5.39E-02	
180	1.58E+02			1.32E+02		6.30E-02	

1. Calculated by multiplying the QD concentration by 33.5.
2. Calculated by dividing $\int A\, dE$ by the average B.
3. Calculated from the QD concentration, particle radius of 0.73 nm from SAXS data fitting, and assuming a CdSe density of 5.82 g/mol.

The calculated concentration of (CdSe) from method 2 agrees well with the values from method 3, which validates the assumption that those samples are composed of only MSCs $(CdSe)_{33}$

and $(CdSe)_{34}$. Values from method 1 also agrees with values from method 3, which validates the radius parameter from SAXS data fitting.

3.6 REFERENCES

(1) Bawendi, M. G.; Steigerwald, M. L.; Brus, Louis, E. The Quantum Mechanics of Larger Semiconductor Clusters (“Quantum Dots”). *Annu. Rev. Phys. Chem.* **1990**, *41*, 477–496.

(2) Michalet, X.; Pinaud, F. F.; Bentolila, L. A.; Tsay, J. M.; Doose, S.; Li, J. J.; Sundaresan, G.; Wu, A. M.; Gambhir, S. S.; Weiss, S. Quantum Dots for Live Cells, in Vivo Imaging, and Diagnostics. *Science* **2005**, *307*, 538–544.

(3) Shen, W.; Tang, H.; Yang, X.; Cao, Z.; Cheng, T.; Wang, X.; Tan, Z.; You, J.; Deng, Z. Synthesis of Highly Fluorescent InP/ZnS Small-Core/Thick-Shell Tetrahedral-Shaped Quantum Dots for Blue Light-Emitting Diodes. *J. Mater. Chem. C* **2017**, *5*, 8243–8249.

(4) Talapin, D. V; Lee, J.; Kovalenko, M. V; Shevchenko, E. V. Prospects of Colloidal Nanocrystals for Electronic and Optoelectronic Applications. *Chem. Rev.* **2010**, *110*, 389–458.

(5) Yu, Q.; Liu, C. Y. Study of Magic-Size-Cluster Mediated Formation of Cds Nanocrystals: Properties of the Magic-Size Clusters and Mechanism Implication. *J. Phys. Chem. C* **2009**, *113*, 12766–12771.

(6) Harrell, S. M.; McBride, J. R.; Rosenthal, S. J. Synthesis of Ultrasmall and Magic-Sized CdSe Nanocrystals. *Chem. Mater.* **2013**, *25*, 1199–1210.

(7) Rao, C. N. R.; Vivekchand, S. R. C.; Biswas, K.; Govindaraj, A. Synthesis of Inorganic Nanomaterials. *J. Chem. Soc. Dalt. Trans.* **2006**, No. 34, 3728–3749.

(8) Park, J.; Joo, J.; Soon, G. K.; Jang, Y.; Hyeon, T. Synthesis of Monodisperse Spherical Nanocrystals. *Angew. Chemie - Int. Ed.* **2007**, *46*, 4630–4660.

(9) Van Embden, J.; Chesman, A. S. R.; Jasieniak, J. J. The Heat-up Synthesis of Colloidal Nanocrystals. *Chem. Mater.* **2015**, *27*, 2246–2285.

(10) Suslick, K. S. Sonochemistry. *Science* **1990**, *247*, 1439–1445.

(11) Bang, J. H.; Suslick, K. S. Applications of Ultrasound to the Synthesis of Nanostructured Materials. *Adv. Mater.* **2010**, *22*, 1039–1059.

(12) Fan, L.; Degen, M.; Bendle, S.; Grupido, N.; Ilavsky, J. The Absolute Calibration of a Small-Angle Scattering Instrument with a Laboratory X-Ray Source. *J. Phys. Conf. Ser.*

2010, *247*.

(13) Kikuchi, T.; Uchida, T. Calorimetric Method for Measuring High Ultrasonic Power Using Water as a Heating Material. *J. Phys. Conf. Ser.* **2011**, *279*, 6–11.

(14) Murcia, M. J.; Shaw, D. L.; Woodruff, H.; Naumann, C. A.; Young, B. A.; Long, E. C. Facile Sonochemical Synthesis of Highly Luminescent ZnS-Shelled CdSe Quantum Dots. *Chem. Mater.* **2006**, *18*, 2219–2225.

(15) Kim, J. Y.; Voznyy, O.; Zhitomirsky, D.; Sargent, E. H. 25th Anniversary Article: Colloidal Quantum Dot Materials and Devices: A Quarter-Century of Advances. *Adv. Mater.* **2013**, *25*, 4986–5010.

(16) Majetich, S. A.; Carter, A. C. Surface Effects on the Optical Properties of Cadmium Selenide Quantum Dots. *J. Phys. Chem.* **1993**, *97*, 8727–8731.

(17) Ning, Z.; Molnár, M.; Chen, Y.; Friberg, P.; Gan, L.; Ågren, H.; Fu, Y. Role of Surface Ligands in Optical Properties of Colloidal CdSe/CdS Quantum Dots. *Phys. Chem. Chem. Phys.* **2011**, *13*, 5848–5854.

(18) Leatherdale, C. A.; Woo, W. K.; Mikulec, F. V.; Bawendi, M. G. On the Absorption Cross Section of CdSe Nanocrystal Quantum Dots. *J. Phys. Chem. B* **2002**, *106*, 7619–7622.

(19) Lazarenkova, O. L.; Balandin, A. A. Electron and Phonon Energy Spectra in a Three-Dimensional Regimented Quantum Dot Superlattice. *Phys. Rev. B* **2002**, *66*, 245319.

(20) Jiang, C.-W.; Green, M. A. Silicon Quantum Dot Superlattices: Modeling of Energy Bands, Densities of States, and Mobilities for Silicon Tandem Solar Cell Applications. *J. Appl. Phys.* **2006**, *99*, 114902.

(21) Jasieniak, J.; Smith, L.; Van Embden, J.; Mulvaney, P.; Califano, M. Re-Examination of the Size-Dependent Absorption Properties of CdSe Quantum Dots. *J. Phys. Chem. C* **2009**, *113*, 19468–19474.

(22) Landes, C. F.; Braun, M.; El-Sayed, M. A. On the Nanoparticle to Molecular Size Transition: Fluorescence Quenching Studies. *J. Phys. Chem. B* **2001**, *105*, 10554–10558.

(23) McBride, J. R.; Dukes, A. D.; Schreuder, M. A.; Rosenthal, S. J. On Ultrasmall Nanocrystals. *Chem. Phys. Lett.* **2010**, *498*, 1–9.

(24) Bowers, M. J.; McBride, J. R.; Rosenthal, S. J. White-Light Emission from Magic-Sized Cadmium Selenide Nanocrystals. *J. Am. Chem. Soc.* **2005**, *127*, 15378–15379.

(25) De La Iglesia, P.; Jaeger, V. W.; Xi, Y.; Pfaendtner, J.; Pozzo, L. D. Structure Characterization and Properties of Metal-Surfactant Complexes Dispersed in Organic Solvents. *Langmuir* **2015**, *31*, 9006–9016.

(26) Ilavsky, J.; Jemian, P. R. Irena: Tool Suite for Modeling and Analysis of Small-Angle

Scattering. *J. Appl. Crystallogr.* **2009**, *42*, 347–353.

(27) Cossairt, B. M.; Owen, J. S. CdSe Clusters: At the Interface of Small Molecules and Quantum Dots. *Chem. Mater.* **2011**, *23*, 3114–3119.

(28) Kudera, S.; Zanella, M.; Giannini, C.; Rizzo, A.; Li, Y.; Gigli, G.; Cingolani, R.; Ciccarella, G.; Spahl, W.; Parak, W. J.; Manna, L. Sequential Growth of Magic-Size CdSe Nanocrystals. *Adv. Mater.* **2007**, *19*, 548–552.

(29) Dukes, A. D.; McBride, J. R.; Rosenthal, S. J. Synthesis of Magic-Sized CdSe and CdTe Nanocrystals with Diisooctylphosphinic Acid. *Chem. Mater.* **2010**, *22*, 6402–6408.

(30) Kasuya, A.; Sivamohan, R.; Barnakov, Y. A.; Dmitruk, I. M.; Nirasawa, T.; Romanyuk, V. R.; Kumar, V.; Mamykin, S. V.; Tohji, K.; Jeyadevan, B.; Shinoda, K.; Kudo, T.; Terasaki, O.; Liu, Z.; Belosludov, R. V.; Sundararajan, V.; Kawazoe, Y. Ultra-Stable Nanoparticles of CdSe Revealed from Mass Spectrometry. *Nat. Mater.* **2004**, *3*, 99–102.

(31) Teixeira, J. Small-Angle Scattering by Fractal Systems. *J. Appl. Crystallogr.* **1988**, *21*, 781–785.

(32) Talapin, D. V.; Rogach, A. L.; Kornowski, A.; Haase, M.; Weller, H. Highly Luminescent Monodisperse CdSe and CdSe/ZnS Nanocrystals Synthesized in a Hexadecylamine-Trioctylphosphine Oxide-Trioctylphospine Mixture. *Nano Lett.* **2001**, *1*, 207–211.

(33) Kodama, K.; Iikubo, S.; Taguchi, T.; Shamoto, S. I. Finite Size Effects of Nanoparticles on the Atomic Pair Distribution Functions. *Acta Crystallogr. Sect. A Found. Crystallogr.* **2006**, *62*, 444–453.

(34) Yun-Sheng, X.; Zhu, C.-Q. Aqueous Synthesis of Luminescent Magic Sized CdSe Nanoclusters. *Mater. Lett.* **2008**, *62*, 2103–2105.

(35) Williamson, C. B.; Nevers, D. R.; Nelson, A.; Hadar, I.; Banin, U.; Hanrath, T.; Robinson, R. D. Chemically Reversible Isomerization of Inorganic Clusters. *Science* **2019**, *363*, 731–735.

(36) Ouyang, J.; Zaman, M. B.; Yan, F. J.; Johnston, D.; Li, G.; Wu, X.; Leek, D.; Ratcliffe, C. I.; Ripmeester, J. A.; Yu, K. Multiple Families of Magic-Sized CdSe Nanocrystals with Strong Bandgap Photoluminescence via Noninjection One-Pot Syntheses. *J. Phys. Chem. C* **2008**, *112*, 13805–13811.

(37) Abe, S.; Čapek, R. K.; De Geyter, B.; Hens, Z. Tuning the Postfocused Size of Colloidal Nanocrystals by the Reaction Rate: From Theory to Application. *ACS Nano* **2012**, *6*, 42–53.

(38) Jasieniak, J.; Bullen, C.; Van Embden, J.; Mulvaney, P. Phosphine-Free Synthesis of CdSe Nanocrystals. *J. Phys. Chem. B* **2005**, *109*, 20665–20668.

(39) Protière, M.; Nerambourg, N.; Renard, O.; Reiss, P. Rational Design of the Gram-Scale

Synthesis of Nearly Monodisperse Semiconductor Nanocrystals. *Nanoscale Res. Lett.* **2011**, *6*, 1–14.

(40) Williamson, C. B.; Nevers, D. R.; Hanrath, T.; Robinson, R. D. Prodigious Effects of Concentration Intensification on Nanoparticle Synthesis: A High-Quality, Scalable Approach. *J. Am. Chem. Soc.* **2015**, *137*, 15843–15851.

(41) Flamee, S.; Cirillo, M.; Abe, S.; De Nolf, K.; Gomes, R.; Aubert, T.; Hens, Z. Fast, High Yield, and High Solid Loading Synthesis of Metal Selenide Nanocrystals. *Chem. Mater.* **2013**, *25*, 2476–2483.

(42) Frenette, L. C.; Krauss, T. D. Uncovering Active Precursors in Colloidal Quantum Dot Synthesis. *Nat. Commun.* **2017**, *8*, 1–8.

(43) Ruberu, T. P. A.; Albright, H. R.; Callis, B.; Ward, B.; Cisneros, J.; Fan, H. J.; Vela, J. Molecular Control of the Nanoscale: Effect of Phosphine-Chalcogenide Reactivity on CdS-CdSe Nanocrystal Composition and Morphology. *ACS Nano* **2012**, *6*, 5348–5359.

(44) Evans, C. M.; Evans, M. E.; Krauss, T. D. Mysteries of TOPSe Revealed: Insights into Quantum Dot Nucleation. *J. Am. Chem. Soc.* **2010**, *132*, 10973–10975.

(45) Brennen, C. E. *Cavitation and Bubble Dynamics*, 1st ed.; Cambridge University Press: Cambridge, 2013.

(46) Sivakumar, M.; Towata, A.; Yasui, K.; Tuziuti, T.; Kozuka, T.; Iida, Y.; Maiorov, M. M.; Blums, E.; Bhattacharya, D.; Sivakumar, N.; Ashok, M. Ultrasonic Cavitation Induced Water in Vegetable Oil Emulsion Droplets - A Simple and Easy Technique to Synthesize Manganese Zinc Ferrite Nanocrystals with Improved Magnetization. *Ultrason. Sonochem.* **2012**, *19*, 652–658.

(47) Nevers, D. R.; Williamson, C. B.; Savitzky, B. H.; Hadar, I.; Banin, U.; Kourkoutis, L. F.; Hanrath, T.; Robinson, R. D. Mesophase Formation Stabilizes High-Purity Magic-Sized Clusters. *J. Am. Chem. Soc.* **2018**, *140*, 3652–3662.

(48) Beecher, A. N.; Yang, X.; Palmer, J. H.; Lagrassa, A. L.; Juhas, P.; Billinge, S. J. L.; Owen, J. S. Atomic Structures and Gram Scale Synthesis of Three Tetrahedral Quantum Dots. *J. Am. Chem. Soc.* **2014**, *136*, 10645–10653.

Chapter 4. EFFICIENT ELECTROSTERIC ASSEMBLY OF NANOPARTICLE HETERODMERS AND LINEAR HETEROASSEMBLIES

Reproduced with permission from Kastilani, R., Wong, R., & Pozzo, L. D. (2018). Efficient Electrosteric Assembly of Nanoparticle Heterodimers and Linear Heteroassemblies. *Langmuir*, *34*(3), 826–836. https://doi.org/10.1021/acs.langmuir.7b01323. Copyright 2017 American Chemical Society.

4.1 INTRODUCTION

Interests in controlled assembly of nanoparticles has spiked due to the unique properties that arise with these ensembles. Just as nanoparticles behave differently than their corresponding material in bulk, new properties are unlocked when nanoparticles are assembled into larger structures with multiple sub-units. The applications of these structures are ubiquitous, including optoelectronic devices,[1,2] sensors,[3–7], data storage,[8–10] protein separation,[11] and catalysis,[12,13] among others. In creating these structures, it is important that the assembling process is precise, scalable, efficient and economic so that these technologies can be successfully translated to benefit society. In this respect, bottom-up self-assembly could be significantly more advantageous than well-established top-down manufacturing processes.[14] As more bottom-up techniques are developed, more complex structures can be created, leading to new properties, functionalities, and applications.

In this work, we focus our attention to developing a novel self-assembling process to organize two or more different types of particles to produce various kinds of heteroassemblies. In the case of assemblies of two particles of different kind, these are essentially Janus doublets or heterodimers. Larger assemblies containing multiple particles are also possible. These clusters are interesting because of the unique properties that can arise when mismatched nanoparticle pairs are clustered.[15] Furthermore these heteroassemblies can also institute multiple functionalities onto a single colloidal entity, creating multifunctional materials. For example, Jang et al. created Pd-Fe_3O_4 doublets that are used as recyclable catalysts in Suzuki coupling reactions.[13] Xu et al. also synthesized Au-Fe_3O_4 doublets that are used as dual functional probes for simultaneous optical and magnetic imaging.[16]

Many different techniques have been developed to create these heteroassemblies,[17–20] employing either direct synthesis of heteroassemblies or assembly of pre-existing particles. In direct synthesis, the second type of nanoparticle is grown directly onto the existing first type of nanoparticle. The second material can be deposited epitaxially by taking advantage of the difference in lattice parameters so that they share a coherent interface. The second material can also be deposited non-epitaxially, and then by increasing the interfacial tension using heat, the second material will coalesce to one side to minimize the interfacial tension. Finally, the second material can also be deposited across immiscible liquid-liquid interface. In this method, one type of nanoparticles is dispersed in an organic solvent, while a metal salt is dissolved in an aqueous phase. Upon reduction of the metal salts, the metallic particles self-assemble and join the existing organic-dispersed nanoparticles at the interface to form heterodimers. A general approach to create doublets of noble metals and semiconductor/magnetic particles by direct epitaxial heterogeneous nucleation has also been patented, demonstrating the economic importance of these complex materials.[21]

Alternatively, heteroassemblies can also by be synthesized from pre-existing particles by using highly-specific molecular targeting molecules as the driver for assembly or by tuning the environment[2,19,22–25]. Yet, each of these methods have unique limitations including the use of complex and expensive chemical steps, fundamental limitations on the types of materials that can be assembled, the use of very high temperatures, and/or limitations in the type of assembled structures that can be formed (e.g. only suitable for dimers). Furthermore, several of these methods produce structures that are dispersed in organic solvents and many applications, such as in biomedical uses[16], require particles to be dispersed in aqueous media.

Here, we present a simple and general methodology to controllably assemble two different types of pre-existing nanoparticles using combined steric and electrostatic forces, which are known as electrosteric interactions. We also demonstrate how this approach can be used to create heterodimers and other heteroassemblies in stable dispersion. The self-assembly is carried out in water, at room temperature, using relatively inexpensive raw materials. The method is an extension of previous work by Larson-Smith, where gold nanoparticles (GNP) were functionalized with polyethylene glycol (PEG) thiols and hydrophobic thiols to induce a controlled assembly process.[26] The hydrophobic thiols induce particle aggregation, but the extent of aggregation is effectively controlled and limited by the amount of PEG that is loaded on the surface of the GNPs. When more PEG is loaded on the surface, smaller particle assemblies are generated. Using this method, they successfully demonstrated the spontaneous formation of doublets, triplets, and so on by only controlling the amount of PEG that was added to the solution. In this work, instead of relying on hydrophobic thiols to induce attraction, the new method uses oppositely charged alkane-thiols to induce controlled aggregation of two different species of nanoparticles. Two different sized gold nanoparticles (GNP) were used as a model system since they are easily synthesized and visualized in the electron microscope. A schematic overview of the synthesis and assembly method is shown in Figure 4.1. We demonstrated that the PEG surface density controlled particle assembly and that we were able to successfully create heterodimers and linear heteroassemblies. Moreover, the structures have been thoroughly analyzed by UV-Vis spectroscopy, dynamic light scattering (DLS), thermogravimetric analysis (TGA), transmission electron microscopy (TEM), and small angle x-ray scattering (SAXS).

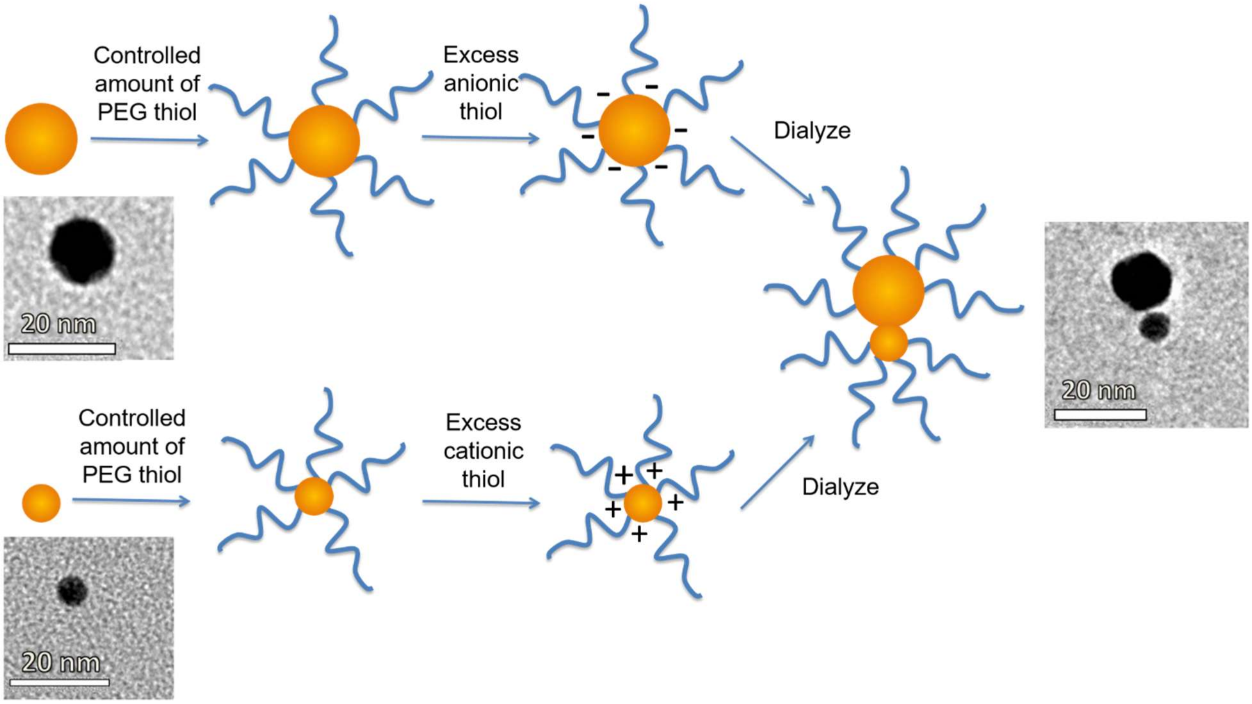

Figure 4.1: Schematic diagram of the process that is used to assemble nanoparticle heteroassemblies in dispersion. Controlled assemblies are created by balancing electrostatic attraction between oppositely charged particles through steric repulsion imparted by surface-bound PEG molecules. TEM micrographs of particles at different stages in the process are also included for comparison.

4.2 EXPERIMENTAL

Chemicals

Gold(III) chloride, sodium citrate, mercaptosuccinic acid, 8-mercaptooctanoic acid, 12-mercaptododecanoic acid (MDA), 8-amino-1-octanethiol chloride (8A1O), and (11-

Mercaptoundecyl)-N,N,N-trimethylammonium bromide (MUTA) were obtained from Sigma Aldrich (St Louis, MO). Hydrochloric acid, sodium hydroxide, and sodium chloride were obtained from Fisher Scientific (Hampton, NH). Mono-functional thiol-terminated poly(ethylene glycol) methyl ether (10 kDa) was obtained from Polymer Source (Dorval, Quebec, Canada). All chemicals were used as received.

Particle Synthesis

Two different types of gold nanoparticles (GNPs), measuring 13 nm and 7 nm in diameter, were used in this investigation. The 13 nm GNP were synthesized using the Turkevich method as refined by Frens,[27] where 0.75 mmol of $HAuCl_4$ dissolved in 625 mL of water was brought to a boil, and 75 mL of 38.8 mM solution of sodium citrate was added to synthesize 750 mL of dispersion. The 7 nm GNP were synthesized using the method proposed by Martin et al.,[28] where 0.25 mmol $HAuCl_4$ and HCl dissolved in 490 mL of water was brought to boil, and 10 mL of 0.1 M $NaBH_4$ and NaOH was added to create 500 mL of 7 nm GNP solution. In both synthesis, a condenser was implemented to prevent water loss, the solution was vigorously stirred throughout the reaction, and stirring was continued for 20 minutes after a red color was obtained while still boiling to allow for Ostwald ripening.

Surface Functionalization with PEG

Each batch of GNPs was functionalized with mono-functional PEG-thiol by dosing a controlled amount of molecules per surface area (0 – 4 chains/nm^2) from a 1 mM PEG-thiol aqueous stock solution. Stock solutions were made and used within 5 minutes to minimize the potential formation of disulfide bonds that can lead to reduced activity. The thiol functional group of the PEG molecules would then bind to the surface of the GNPs to create ‘hairy particles’. The dispersions were allowed to react for 24 hours before subsequent functionalization with charged thiols.

Surface Functionalization with Charged Alkane-Thiol Molecules

Corresponding charged thiols were added from a 10 mM stock solution in ethanol at a surface concentration (30 chains/nm^2) that was well above the maximum thiol packing density (~6 chains/nm^2).[29–32] Stock thiol solutions were also made and used within 5 minutes to minimize the potential formation of disulfide bonds that could lead to inactivation. These small charged thiols would diffuse through the PEG adlayer and bind onto unoccupied surface sites to create ‘charged-hairy particles’.[33] The 13 nm GNPs were functionalized with an anionic thiol while the 7 nm GNPs were functionalized with cationic thiols. The dispersions were allowed to react for 24 hours before subsequent dialysis to remove unbound PEG and excess charged thiol from solution. Each batch was dialyzed into 1 mM NaCl buffer for 21 hours, with the buffer having 100x volume relative to that of the sample, and the solution was changed at the 2 and 7-hour marks. Dialysis membrane Spectra/Por 6 with 50 kDa pores was obtained from Spectrum Laboratories (Rancho Dominguez, CA). The pH of the dispersion was adjusted to 6.0 using HCl or NaOH after dialysis.

Thermogravimetric determination of PEG concentration

Post-dialysis dispersion was concentrated using a stirred ultrafiltration cell (Millipore, Billerica, MA), lyophilized and analyzed using a thermogravimetric analysis (TGA) instrument (Q50 TA Instruments, Newcastle, DE). Samples were ramped at 1 °C/min until 550 °C under nitrogen gas flowing at 40 mL/min.

Self-assembly Process

The dispersions were mixed at a desired particle ratio of 13nm GNP and 7nm GNP, at room temperature. To get the appropriate ratio, first, complete reduction of gold ions during particle synthesis was assumed and corroborated with SAXS experiments (supplemental information). The concentration of the particle dispersion depends very strongly on the volume of each particle. Because the volume of a particle is proportional to R^3, small errors in particle size measurement lead to significant errors in concentration calculation. To solve this, the two dispersions were mixed in varying volume ratios to count the particles and a correlation curve was used to determine the dispersion volume ratio that would be necessary to create the desired particle ratio. In this work, systems with 1:1 particle ratio were the most interesting and is the focus of the analysis, but systems with excess particles (i.e. 10:1 and 1:10 particle ratios) were also investigated (supplemental information). The mixtures were then left for two days for the particles to assemble and reach their final structures before final analysis.

Characterization

UV-Vis spectroscopy was performed using Thermo Scientific Evolution 300 (Waltham, MA) over a range of 300 – 800 nm with 2 nm bandwidth. Before analysis, samples were diluted with water to reduce the concentration by a factor of four. Dynamic light scattering (DLS) was performed using a Malvern Zetasizer Nano ZS (Malvern, United Kingdom), using a laser wavelength of 633 nm. Samples were diluted by a factor of ten with water. Transmission electron microscopy (TEM) was performed using FEI Tecnai G2 F20 Supertwin (Hillsboro, OR). Samples were diluted twenty times with water and drop cast onto a 400 mesh copper grid with thin carbon film (Redding, CA). Significant dilution was necessary to allow for the identification of isolated particle assemblies. Prior to drop casting, the TEM grid was processed in a glow discharge chamber to make the surface more hydrophilic, which prevented particle aggregation during drying. Analysis of TEM images were performed using ImageJ software, developed by National Institute of Health. Small angle x-ray scattering (SAXS) was performed using beamline 12-ID-B in Advanced Photon Source, Argonne National Laboratory. SAXS data were analyzed using the Igor Pro SANS and USANS toolkit developed by National Institute of Standards and Technology, Center for Neutron Research.

4.3 RESULTS AND DISCUSSION

Gold particles were chosen because their surface chemistry is well understood and because monodisperse particles of variable size can be easily produced without the use of strongly-bound surface capping agents (e.g. thiol). The use of differently-sized nanoparticles facilitates the identification of particle populations in electron microscopy. GNPs of different type were synthesized in separate batches. Particle sizes were measured using TEM (N > 100) and particle concentration was calculated assuming complete reduction of gold ions and bulk density of gold. The total volume fraction of gold particles in each dispersion was measured with SAXS in absolute scale. The SAXS results had very good agreement with the assumption of complete reduction of gold ions. Both the 13 nm and 7 nm GNP solutions were initially red in color due to surface plasmon resonance, as indicated by a strong absorbance peak around 520 nm in the UV-Vis spectra (Figure 4.3a), which is typical of GNPs at this size range. Key parameters from the resulting dispersions are shown in Table 4.1.

Table 4.1: Parameters corresponding to the GNP dispersions that were synthesized and used in this work. Different sized GNPs facilitates differentiation of particles in electron microscopy. [a]From TEM analysis [b]Calculated from initial gold ion concentration and average particle size.

GNP	**Diameter[a]**	**PDI[a]**	**Nanoparticle Concentration[b]**
Larger	13.2 nm	0.0064	8.23×10^{12} cm^{-3}
Smaller	7.0 nm	0.0289	2.6×10^{13} cm^{-3}

Consistent with previous work in our group,[26] the amount of PEG chains that actually binds to the surface of the gold is much lower than the actual dosing amount. This is a result of PEG-thiol – gold binding that is affected by surface morphology, thiol reactivity, solvent quality, and the possible presence of other thiol moieties (e.g. excess charged thiols) in solution. The actual amount of PEG chains that are bound to the surface of the gold particles were determined by thermogravimetric analysis (TGA). TGA curves are given in the supporting information. Results in Table 4.2 show that only a small fraction (15-30%) of the dosed PEG actually binds to the surface of the GNPs and that the fractional binding efficiency is strongly affected by the particle size. Since the PEG binding is never complete, we make a distinction between PEG dosing and actual bound PEG. Henceforth, the reported numbers will be of the PEG surface concentration rather than PEG dosing.

Table 4.2: Dosed PEG concentration and actual surface concentration of thiol molecules on the surface of GNPs as determined by TGA.

13 nm GNP			**7 nm GNP**		
PEG dosing (chains/nm^2)	**PEG Surface Concentration (chains/nm^2)**	**MDA Surface Concentration (molecules/nm^2)**	**PEG dosing (chains/nm^2)**	**PEG Surface Concentration (chains/nm^2)**	**MUTA Surface Concentration (molecules/nm^2)**
1	0.15	4.60	1	0.32	3.70
2	0.31	6.73	2	0.66	3.34
3	0.43	6.49	3	0.70	3.23
4	0.58	5.90	4	0.84	3.16

Since heteroassemblies are desired, it is very important to maximize electrostatic attraction in these systems. Stronger electrostatic forces encourage binding between oppositely charged GNPs and discourage homoaggregation between equally-charged GNPs. Hence, all samples were dosed with excess cationic/anionic thiols. A decreased concentration of charged ligand would lower the surface potential, decreasing attraction between oppositely charged particles (heteroaggregation) and also decrease the barrier against homoaggregation. This situation is akin to adding salt into the dispersion, and its effects can be observed in Figure 4.2. Since the goal is to create heteroaggregates, it is imperative to maximize the electrostatic charge. There are two key parameters that can be optimized to maximize electrostatic forces: the charge density/potential on the GNPs' surfaces and the Debye length of the solution. Several cationic and anionic candidates for charged thiols were considered, and zeta potential experiments were performed to see which molecules would result in the greatest surface electrostatic potential. After this analysis, MDA and MUTA were chosen as the anionic and cationic thiols due to their large zeta-potential magnitudes with opposite sign over a broad pH range. However, several other candidate thiols resulting in similar surface properties were also identified and could have also been used in this work. This suggests that significant design flexibility is possible for this controlled assembly methodology. Details regarding the zeta potential experiments are provided in the supporting information.

A thorough dialysis step is also essential to maximize electrostatic interactions and to achieve a high concentration and yield of heteroassemblies. First, dialysis removes excess ions that are present after the synthesis of the GNPs such as citrate and chloride ions to reduce screening and to maximize the range of the electrostatic interactions. Secondly, dialysis also removes free, excess PEG and charged thiols to prevent charge neutralization that can be caused by ligand exchange after mixing particles of different surface charge. Thiols are known to bind competitively to gold surfaces and, if thiols of opposite charge are present, they can adsorb to produce a more favorable neutral particle while reducing electrostatic attraction. Self-assembled monolayers of cationic thiols on a nanoparticle are known to be competitively replaced by free anionic thiols in solution and vice versa.[34–40]

In this work, it was decided to dialyze particles into a solution of 1 mM NaCl so that the ion concentration would be low but also controlled across different samples. With the known solvent properties and surface potential from zeta potential measurements, interaction potentials could be estimated for charged particles in the absence of steric interactions (Figure 4.2). The electrical interaction potential was calculated using a modified Hogg-Healy-Fuerstenau (HHF) formula for dissimilar particles:[41]

$$\Phi_{\mathrm{Elec}} = \frac{\varepsilon a_1 a_2}{4(a_1+a_2+S_0)}\left[(\psi_1+\psi_2)^2 \ln\left(1+e^{-\kappa S_0}\right) + (\psi_1-\psi_2)^2 \ln\left(1-e^{-\kappa S_0}\right)\right] \tag{4.1}$$

and the van der Waals interaction potential values were calculated using the Hamaker approach:[42]

$$\Phi_{vdW} = -\frac{A}{6}\left[\frac{2a_1a_2}{S_0^2+2a_1S_0+2a_2S_0} + \frac{2a_1a_2}{S_0^2+2a_1S_0+2a_2S_0+4a_1a_2} + \ln\left(\frac{S_0^2+2a_1S_0+2a_2S_0}{S_0^2+2a_1S_0+2a_2S_0+4a_1a_2}\right)\right] \tag{4.2}$$

In eq 4.1 and eq 4.2, a_n is the radius of the particle, S_0 is the distance of closest approach between particles, ε is the dielectric constant of the medium, ψ_n is the surface potential, κ is the inverse Debye length, and A the Hamaker constant of gold across water. Since steric repulsion from PEG is not included in these calculations, this would only apply to particles that preferentially approach and bind on surface regions that have few or no PEG molecules present to generate steric repulsion. The DLVO calculations serve to demonstrate the role of electrostatics in the system, such as how interactions are affected by salt concentration to dictate the assembly of heteroaggregates versus homoaggregates. Including a steric term to these calculations would convolute the role of electrostatics with sterics. Moreover, to estimate these forces, significant assumptions are required regarding the polymer surface distribution that would lead to significantly more uncertainty in trying to quantitatively describe steric forces. This could result in potential misrepresentations of the data. Still, this simple analysis can provide great insight into the effect of altering electrostatic interactions by changing solution conditions. Surface potentials for the models were approximated from zeta potential measurements that were carried out on charged particles without any bound PEG-thiol. These zeta-potentials were -77 mV for the 13 nm GNPs and 38 mV for the 7 nm GNPs at a pH of 6. Depending on the nature of the charged thiol molecule, the surface charge can vary depending on the pH of the solution. However, since we desire strong opposite charging on the particles for assembly at the same solution conditions, the pH should be such that it is well below the pKa of the cationic thiol and well above that of the anionic thiol. For this study, the pH of all solutions was fixed at 6.0, where both sets of thiols were fully charged. It should be noted that for these particular thiol molecules, the pH range where high opposite charges could be obtained was broad and ranged from pH 4 – 12. As anticipated, the results of this DLVO analysis (Figure 4.2) clearly show that higher salt concentrations encourage homoaggregation and discourage heteroassemblies, both of which are undesirable.

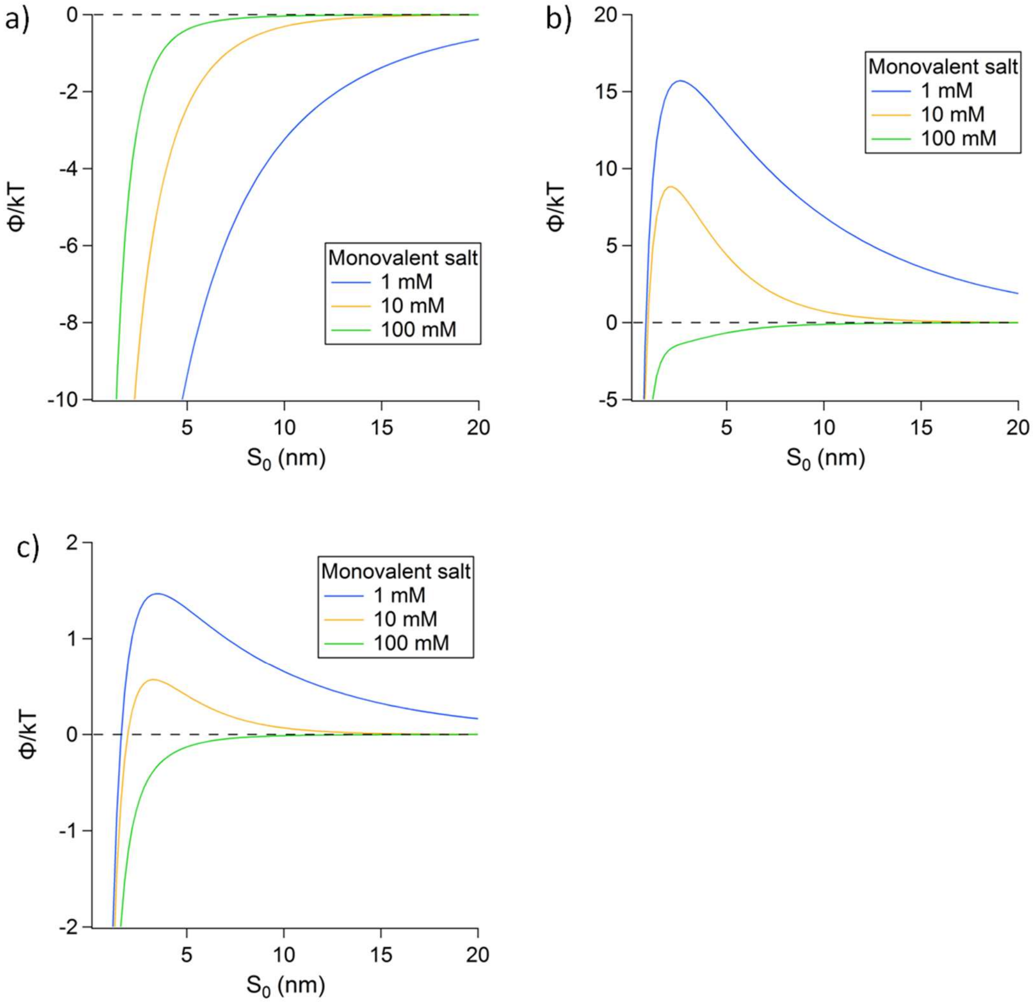

Figure 4.2: DLVO plots showing the potential between a) oppositely charged 7 nm GNP and 13 nm GNP, b) two anionic 13 nm GNPs, and c) two cationic 7 nm GNPs.

If the GNPs were to assemble and be close together (i.e. less than one diameter apart), one would expect to observe plasmonic coupling between the particles that would result in a red-shift the absorbance peak (Figure 4.3a) and a color change from red towards purple. After self-assembly was initiated by mixing oppositely charged particles, the mixtures were left for two days to allow sufficient time for the particles to assemble and reach their final structure. The required assembling time span was determined by measuring the UV-Vis spectra for mixtures every 24 hours; the spectra at the 48-hour mark and the 72-hour mark were very similar, indicating that assembly was complete after two days.

Examples of the UV-Vis spectra for individual particles and their 1:1 mixtures are shown in Figure 4.3a, with the red-shifts demonstrated. The red-shifts are modest (i.e. 10's of nm) due to the long spacer length of the charged thiols, which results in weak coupling of surface plasmons, and due to the small size of the nanoparticle assemblies. This is also consistent with previous work that showed smaller plasmonic red-shifts with longer thiol spacers.[26] Nevertheless, the change is very reproducible and it is well within the resolution of the spectrophotometer (± 1 nm). A summary of the peak wavelengths is shown in Figure 4.3b.

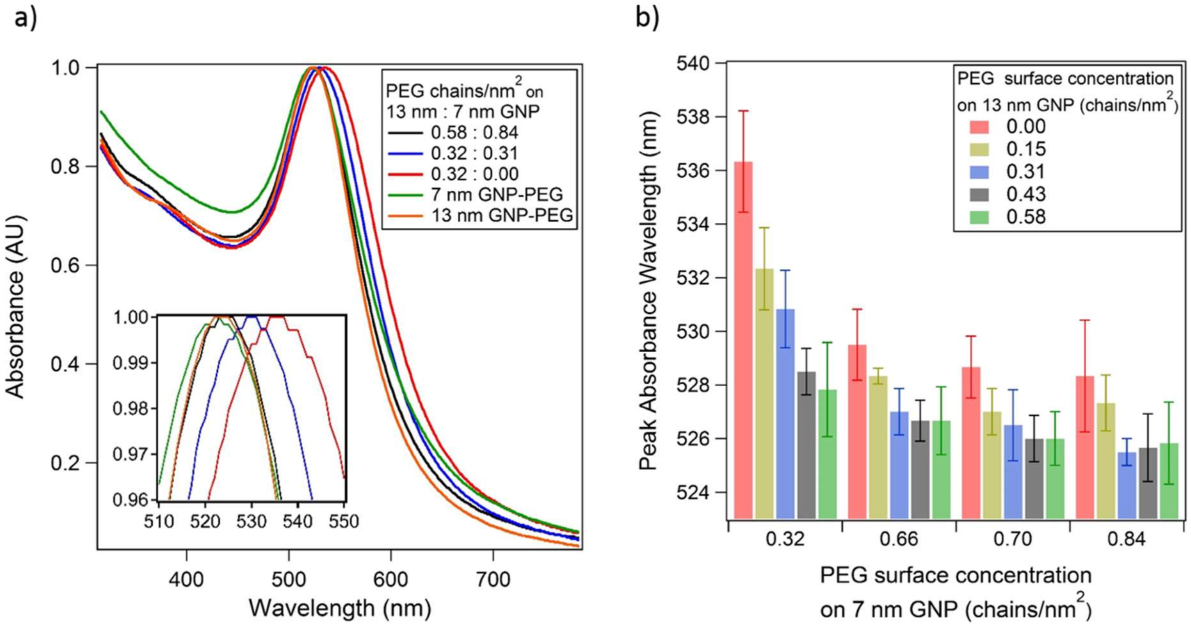

Figure 4.3: UV-Vis spectra of GNP mixtures. a) Examples of the UV-Vis spectra of singlets and assemblies of GNPs. Insert shows the plot zoomed in at the peaks. b) Dependence of peak wavelengths with different PEG surface concentration on both 13 nm and 7 nm GNPs. Error bars represent one standard deviation of samples prepared in triplicates.

In order to further investigate the trends observed in UV-Vis experiments, dynamic light scattering (DLS) experiments were performed to identify changes in hydrodynamic dimensions that result from the formation of particle assemblies. Figure 4.4 shows some example of DLS size distributions for 1:1 particle mixtures containing different PEG surface concentrations on each type of particle. The hydrodynamic diameter of the bare 13 nm GNP, without any surface-bound PEG, is very close to the true diameter as measured by SAXS and TEM. When the GNP is functionalized with PEG, the polymer adlayer adds hydrodynamic drag and this increases the hydrodynamic diameter. The amount of increased drag depends on PEG surface concentration on the GNPs and on the molecular weight of the polymer. For example, for the 13 nm GNPs, the lowest and highest PEG surface concentration of 0.15 chains/nm^2 and 0.58 chains/nm^2 increased the hydrodynamic diameter by 10 nm and 15 nm respectively. When oppositely charged particles are mixed, the hydrodynamic drag increased further due to the formation of multi-particle assemblies. The peak sizes from DLS measurements as a function of PEG loading on the GNPs are shown in Figure 4.4b.

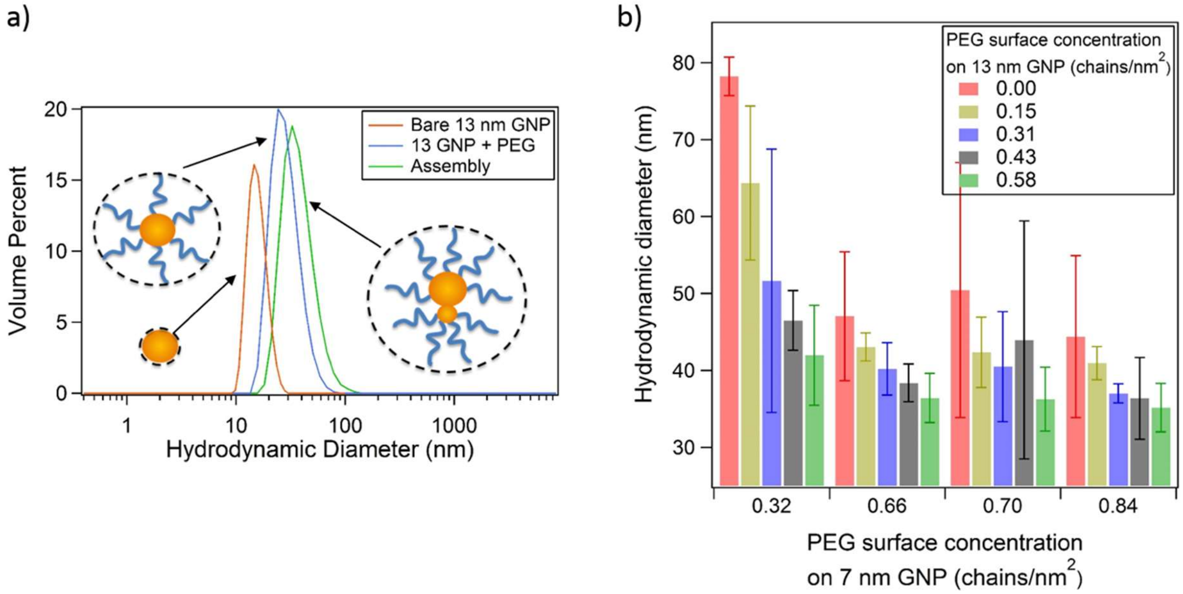

Figure 4.4: a) DLS size distributions for bare particles, PEG-coated particles and multi-particle heteroassemblies. b) Dependence of hydrodynamic diameter on PEG surface concentration of 13 nm and 7 nm GNPs. Error bars represent one standard deviation of samples prepared in triplicates.

While UV-Vis and DLS indirectly measure parameters that are related to the size of the particles in dispersion, these techniques do not have the high resolution that is necessary to probe their shape. A high-resolution technique is necessary to corroborate that heteroassemblies are being formed by electrosteric interactions and that homo-aggregation is not occurring. To that effect, TEM was performed on selected samples at several different PEG concentrations in each particle type to identify the anticipated changes in structure. At relatively high PEG concentrations, such as 0.66 PEG/nm^2 and 0.43 PEG/nm^2 on the 7 nm and 13 nm GNP respectively, a very high concentration of doublets was selectively produced with a yield that was greater than 66% (Figure

4.5) which we call the ‘doublet’ sample. More images of this sample can be seen in the supporting information. This represents an improvement of more than twice the efficiency for doublet formation that was found in recent work.[43] Unfortunately, the heterodimer yield could not be compared to several other published methods since efficiency numbers (i.e. yield of desired structure) were not reported.

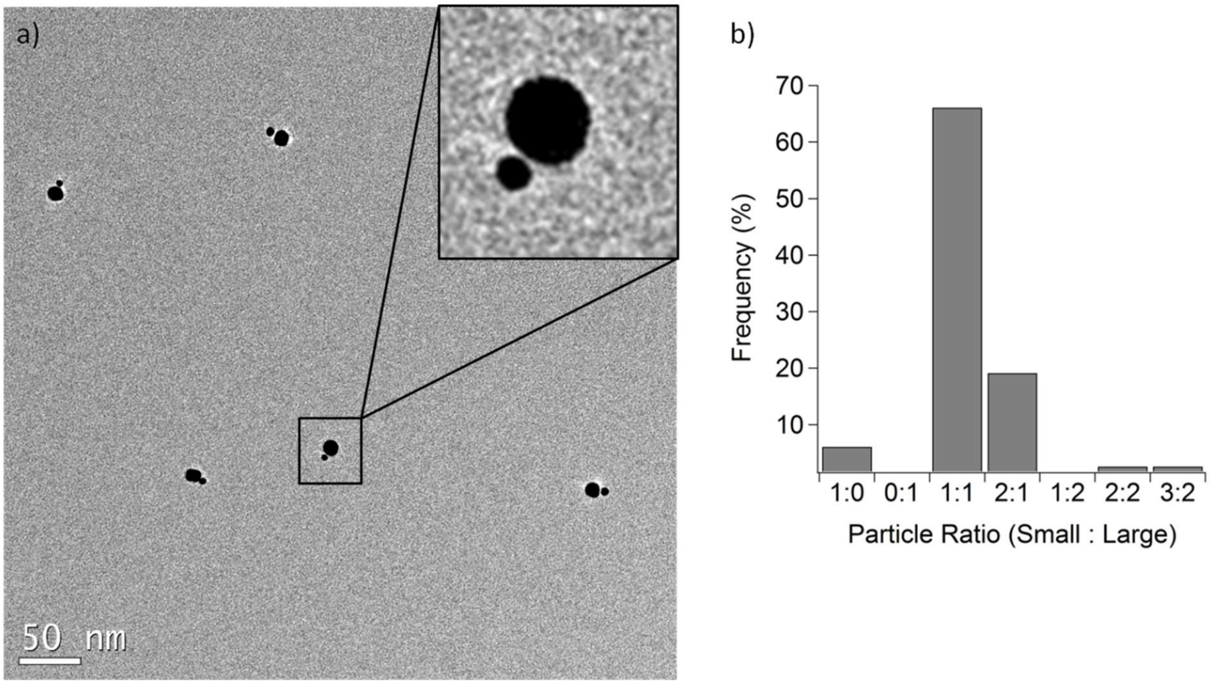

Figure 4.5: a) TEM images for a sample containing particles mixed at a ratio of 1:1 (cationic: anionic) that were loaded with 0.66 PEG/nm^2 and 0.43 PEG/nm^2 on the cationic 7 nm and anionic 13 nm GNP respectively. b) A frequency plot of the observed cluster sizes in terms of the number of large and small particles that were incorporated into the heteroassembly. The total number of structures that were counted was 115.

TEM images were also obtained for samples that had lower surface concentration of PEG since they were expected to produce larger heteroassemblies. Figure 4.6 shows some representative images obtained from a sample where PEG molecules were bound at a concentration of 0.32 and 0.31 chains/nm^2 for the 7 nm and 13 nm GNP, respectively. Clearly the resulting heteroassemblies are much larger with less surface-bound PEG, which is what was also anticipated from UV-Vis spectroscopy and DLS data. However, in contrast to previous work, where hydrophobic attraction was use, the assemblies that were observed in these TEM images tend to be linear in nature rather than globular.[26] Moreover, the size distribution of assemblies is much wider than that of samples that contained larger amounts of PEG and formed doublets. Samples with this intermediate PEG surface concentrations had observable assemblies that ranged from triplets (Figure 4.6e) to very long chains of more than 20 sub-particles (Figure 4.6f). TEM images were also taken for a different intermediate PEG surface concentration of 0.66 and 0.15 chains/nm^2 for the 7 nm and 13 nm GNPs, respectively (supporting information). The resulting assemblies were similar to those in Figure 4.6: polydisperse linear heteroassemblies. At lower surface concentration of PEG, but high enough to sustain stability, even larger assemblies were created and the resulting structures had a higher fractal dimension (i.e. they were more globular than linear). Examples of these structures are show in Figure 4.7, where the surface PEG concentration was 0.32 and 0.15 chains/nm^2 for the 7 nm and 13 nm GNPs, respectively.

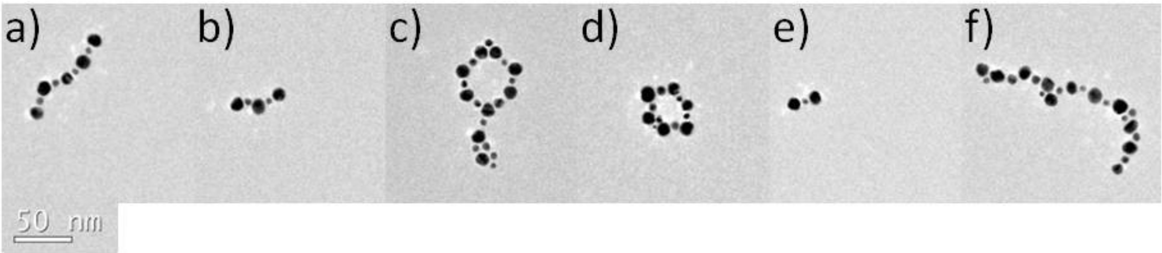

Figure 4.6: TEM images of a sample with particles mixed at a ratio of 1:1 (cationic : anionic) where the surface PEG concentration (10 kDa) corresponded to 0.32 and 0.31 chains/nm^2 on the 7 nm (cationic) and 13 nm (anionic) GNP, respectively. Linear heteroassemblies were observed.

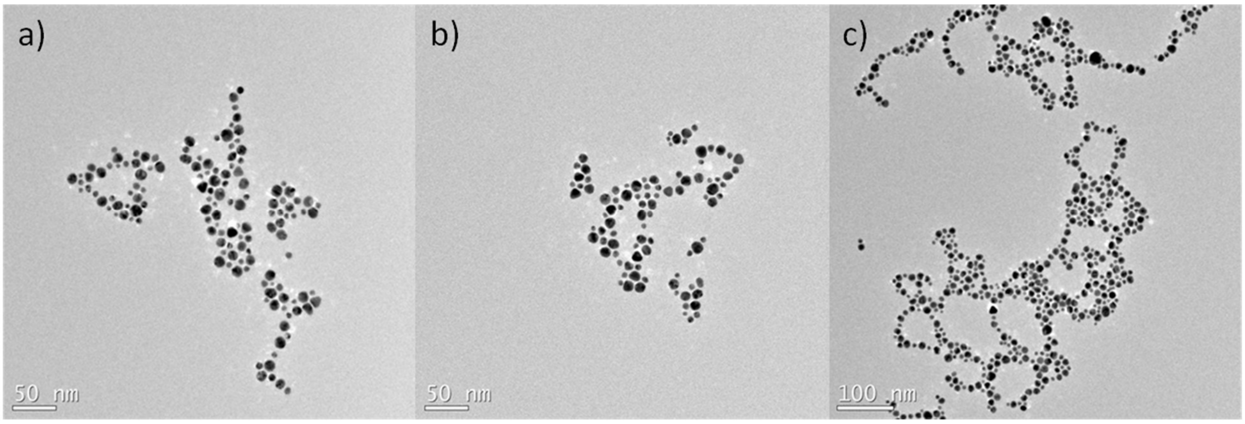

Figure 4.7: TEM images of a sample with particles mixed at a ratio of 1:1 (cationic : anionic) where the surface PEG concentration (10 kDa) corresponded to 0.32 and 0.15 chains/nm^2 on the 7 nm (cationic) and 13 nm (anionic) GNP, respectively. Assemblies were more globular in structure.

To further confirm that these heteroassemblies were created in dispersion, rather than due to drying effects during TEM grid preparation, SAXS was also used to analyze the sample in-situ while dispersed in water, probing a large ensemble of particles rather than individual snapshots on a TEM grid. SAXS would also demonstrate the scalability of this approach where the assembly process proceeds in bulk dispersion that could be of arbitrarily large volumes, at relatively large particle concentrations (i.e. large for nanoparticle systems) and that the cost of the raw materials is lower than for other competing approaches (e.g. DNA templating). In SAXS, a collimated x-ray beam hits the dispersion and some photons are scattered at various angles due to their interactions with the dispersed materials. The intensity of scattered and transmitted x-rays are collected as a function of scattering angle. For analysis purposes, the intensity I(q) is plotted against the scattering vector q, which is dependent to the scattering angle and the photon wavelength. I(q) represents the Fourier transform of the correlation function of electron density in the sample. The profile that is generated depends on the material composition and shape/geometry of the sample. Since the scattering intensity is strongly related to the electron density contrast (i.e. between dispersed and continuous phases), the scattering signal from SAXS is dominated by the GNPs and the PEG chains are essentially ‘invisible’ via this technique. In other words, SAXS allows for the analysis of the interparticle distances between GNPs without being affected by the surface-bound organic molecules. The dependence of PEG surface concentration on the scattering profile is shown in Figure 4.8. In each figure, the PEG surface concentration of the 13 nm GNPs was varied and that of the 7 nm GNPs was fixed (Figure 4.8a), and vice versa (Figure 4.8b).

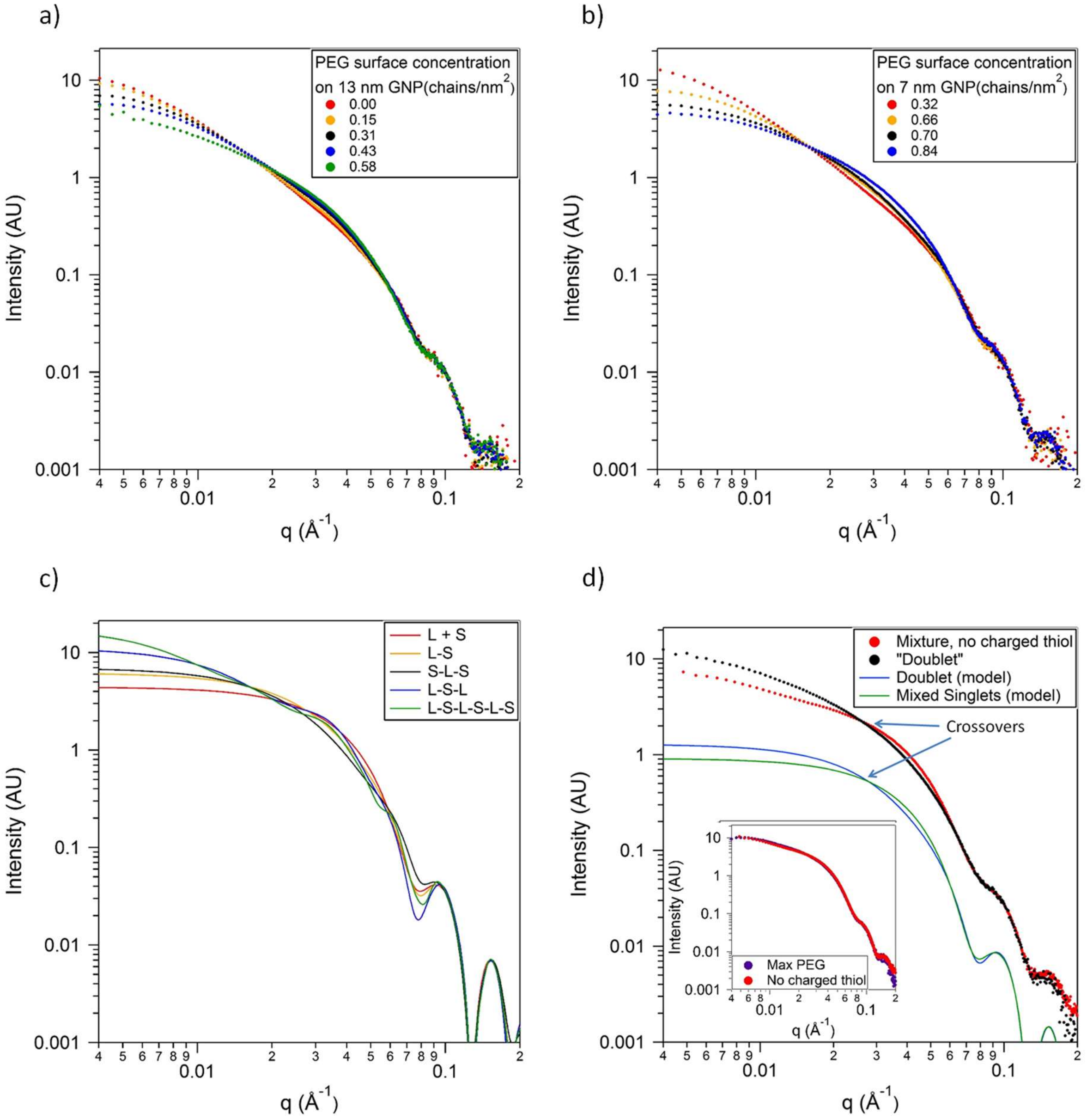

Figure 4.8: Dependence of PEG surface concentration and SAXS profile when a) PEG surface concentration on 7 nm GNP is fixed at 0.32 chains/nm^2, b) PEG surface concentration of 13 nm GNP is fixed at 0.00 chains/nm^2. Other combinations of PEG surface concentration show very similar pattern. c) Theoretical scattering profiles of various assemblies as calculated using the Debye model (eq 4.3); L represents a 13 nm GNP (large) and S represents a 7 nm GNP (small). d) Comparison of scattering profiles between doublets and mixed singlets, both theoretical and experimental data. Insert compares the scattering profile between a sample where no charged thiols were used (i.e. singlets) and samples loaded with the maximum PEG surface concentration in this work, 0.84 and 0.58 chains/nm^2 for the 7 nm and 13 nm GNPs, respectively.

The theoretical scattering intensity for different particle assemblies was calculated with help from the Debye model for complex systems consisting of individual spherical subunits (eq 4.3). In eq 4.3, q is the scattering vector, r_{ij} is the center to center distance between the spherical subunits and F_i is the form factor of the individual particles. For spheres, the form factor is defined in eq 4.4, where R is the radius of the sphere. Note that the Debye model is only useful for modeling the scattering profile for a monodisperse structure where there are no variations in the size, number or the relative position of the individual components (i.e. primary particles) of heteroassemblies in the dispersion. For polydisperse samples, the Debye equation would have to be used to model each type of assembly individually and this would need to be weighed by the relative abundance of each species in the dispersion. Assuming linear assemblies, the theoretical scattering profiles for these assemblies was calculated and shown in Figure 4.8c.

$$I(q) \propto \sum_{i=1}^{N} F_i(q)^2 + 2\sum_{i=1}^{N}\sum_{j=i+1}^{N} F_i(q)F_j(q)\frac{\sin(qr_{ij})}{qr_{ij}} \tag{4.3}$$

$$F(q) = \frac{3[\sin(qR) - qR\cos(qR)]}{(qR)^3} \tag{4.4}$$

The PEG molecules serve as stabilizers against uncontrolled particle aggregation. At one extreme, when the PEG functionalization step was skipped and there were no PEG molecules attached to the surface of the GNPs, uncontrolled aggregation and sedimentation was observed due to attractive electrostatic and van der Waals forces. This contradicts a previous work by Gschneidtner et al., where oppositely charged colloids were able to form stable dispersions without any polymer protection.[43] On the other extreme, when there are abundant PEG chains on the surface of the GNPs, previous work has shown that clustering can be completely inhibited and this was also observed in our work.[26] Somewhere in the middle, there is a balance of electrostatic attraction and polymer steric repulsion that is suitable to create particle assemblies of controlled size. We observed that dosing the GNPs at PEG concentrations of 0 to 4 chains/nm^2 covered the entire spectrum from large aggregation to stable colloidal assemblies (e.g. doublets) and fully stabilized individual particles. Mixtures of particles where the 7 nm GNPs functionalized with only MUTA (no PEG) never reached a stable final structure regardless of the PEG loading on the 13 nm GNPs. Eventually these particles aggregated and sedimented within a few weeks.

Significant differences were observed in the stability of the 'as-synthesized' nanoparticles that were used in this study. It was noted that, before mixing, the anionic 13 nm GNP were significantly more stable than the cationic 7 nm GNP. In the absence of PEG conjugation to the surface, the cationic 7 nm particles were not stable over long times (days). This effect was due to the lower surface charge density that could be achieved upon conjugation with MUTA as compared to conjugation with MDA. Therefore, despite the fact that the van der Waals attraction is lower for smaller particles, the electrostatic repulsion that prevents homoaggregation was significantly weaker for the smaller particles. In fact, the zeta-potential values of the GNPs functionalized with MUTA (+38 mV) were significantly lower than those functionalized with MDA (-77 mV). This is further quantified with the predictions from DLVO theory (Figure 4.2). While the 13 nm particles have a large energy barrier against homoaggregation, the bare 7 nm particles have an energy barrier of less than 2 kT. TGA measurements also showed that the MUTA surface concentration was up to 50% lower than that of the larger GNPs functionalized with MDA. Therefore, for the GNPs with MUTA used in this study, a small amount of surface-bound PEG was essential to preventing homoaggregation from occurring in the long term. Still, TEM images showed that heteroaggregation with oppositely charged GNPs are preferred over homoaggregation between positively charged 7 nm GNPs. As a control, when oppositely charged 13 nm and 7 nm

GNPs without PEG functionalization were mixed, a color change from red to purple was observed in the dispersion within a few minutes, indicating rapid formation aggregates, and sedimentation followed within a few hours. In contrast, signs of homoaggregation between GNPs functionalized with only MUTA (no PEG) were only observed after several weeks at rest.

When the 13 nm and 7 nm GNP were mixed together in 1:1 ratio, UV-Vis (Figure 4.3b), DLS (Figure 4.4b), and SAXS (Figure 4.8) suggest that lower PEG loading on the GNP resulted in larger clusters. This is in perfect agreement with the observations made by Larson-Smith et.al. for particle assemblies that were formed by hydrophobic attraction and steric repulsion.[26] Here, the formation of multi-particle assemblies caused surface plasmons on the surface of neighboring GNPs to couple together and this was observed as a shift in the primary resonant frequency to a larger wavelength. As the resulting particle assemblies increase in size, due to a decrease in steric repulsion (i.e. PEG surface concentration), the red-shift increased further (Figure 4.3b). DLS results (Figure 4.4b) further supported the trends observed from UV-Vis spectroscopy. Here, the hydrodynamic diameter of the particles was calculated from the measurement of diffusion coefficients that are obtained from DLS. When comparing Figure 4.4b to Figure 4.3b, the trend is very similar. Larger hydrodynamic diameters are measured in samples containing less PEG loading on either type of GNPs, indicating the formation of larger clusters. Although the expected changed in size with PEG surface concentration were very evident in DLS, it must be noted that the hydrodynamic diameter values will deviate from the real size of the heteroassemblies when their aspect ratio is very large (i.e. linear structures). This is due to the intrinsic use of the spherical Stoke-Einstein relation that is used to convert between diffusion coefficient and particle size. Nevertheless, the DLS results provided a useful assessment of the effect of changing the steric interactions between particles. SAXS, which allows the measurement of size of solely the GNPs without the effect of PEG, also confirms the findings of UV-Vis spectroscopy and DLS. In light of the linear assemblies observed under TEM, theoretical scattering profiles of various assemblies were calculated (Figure 4.8c). It is evident that higher intensity and absolute value of the slope at low-q, indicating a larger radius of gyration, were observed for larger linear assemblies. A very similar pattern is seen for samples functionalized with less PEG (Figure 4.8a,b). Although not all combinations of PEG surface concentrations are shown here, other combinations show a very similar pattern.

Also in agreement with previous work, loading the particles with a very large amount of surface-bound PEG prevented their assembly from occurring due to strong steric repulsion. Therefore, this resulted in the formation of a stable mixture of dissimilar particles, where the electrostatic attraction would not be enough to overcome the steric repulsion imparted by the polymer. In the insert of Figure 4.8d, the scattering curve of a sample with a high PEG surface concentration of 0.84 and 0.58 chains/nm^2 on the 7 nm and 13 nm GNP, respectively, is identical to that of a perfectly stable control sample that was prepared at an identical particle ratio (1:1) but lacking charged thiols and electrostatic attraction. This result demonstrated that loading the particles with a large amount of PEG was sufficient to prevent their assembly from occurring resulting in a stable mixture of dissimilar particles.

When a slightly lower surface concentration of PEG was used (0.66 PEG/nm^2 and 0.43 PEG/nm^2 in the 7 nm and 13 nm GNP respectively), a very high concentration of heterodimers was selectively produced with a yield of greater than 66% (Figure 4.5). This result suggested that clustering was effectively limited by steric interactions at high PEG surface concentrations but there was still sufficient free surface to allow for the formation of doublets. In addition to TEM, SAXS analysis of these samples (Figure 4.8d) also supported the formation of stable doublets in dispersion. This was demonstrated by comparing experimental SAXS data and model predictions for heterodimers and for a sample with identical composition but no attractive interaction (i.e. no charged thiols). From Figure 4.8d, it is clear that the features in the data and the model correspond well between doublets and non-interacting mixtures. The doublet model and sample had a higher low-q intensity than the mixed-particles at low q, which indicates a larger radius of gyration. At intermediate q values (~0.025 Å^{-1}), there is a cross-over between the profiles for the heterodoublet and the non-interactive particle mixture that shows up in both the model and in the experimental data. Finally, at high q values (>0.07 Å^{-1}) the profiles for the heterodoublet and the non-interacting mixture become identical since the characteristic length-scale that is being probed by SAXS in this range is smaller than that of an individual particle. Unfortunately, polydispersity in the particle size prevented us from making a quantitative comparison (i.e. direct fitting) between the models and the experimental data. It should also be noted that the lack of polydispersity in the model leads to more prominent oscillations in the profiles when compared to the experimental scattering data. In any experiment, the scattering signal is a sum of all the contributions from the structures in a dispersion. If there is polydispersity in these structures, the period of oscillation would be different from one assembly to another (eq 4.3) and this would result in significant dampening of these oscillations.

At intermediate PEG surface concentrations, such as 0.32 and 0.31 chains/nm^2 for the 7 nm and 13 nm GNP respectively, steric interactions did not seem to provide tight enough control to fully limit growth and this resulted in linear heteroassemblies with large variations in length (Figure 4.6). Interestingly, particles in these assemblies are always alternating between the anionic 13 nm and the cationic 7 nm GNP demonstrating that their self-assembly is dominated by specific electrostatic attraction and not by van der Waals forces or other colloidal attraction force. No globular assemblies were observed in any of these samples (i.e. the resulting structures had low fractal dimension). However, several linear assemblies were observed to curl back upon themselves to create rings. There are several plausible explanations for the observation of exclusively linear structures. If clustering is diffusion limited, then this result agrees with previous work showing that diffusion limited growth results in structures of lower fractal dimension. The fractal dimension was found to increase monotonically with stability ratio and shear,[44,45] reaching even lower fractal dimension at low ionic strength.[46] Another explanation comes from the electrostatic fields that surround the structures. Figure 4.8 shows a finite element model simulation of the electrostatic field surrounding a heterodimer composed of oppositely charged particles. As one would anticipate, the surrounding field is not spherically symmetric around either the positively charged or the negatively charged GNPs. Moreover, in the lateral region between the particles, the opposite local electrical potentials radiating from the particles cancel out. Therefore, regions of strongest local electrostatic potential are located at the two opposing ends of the dumbbell. Thus, an approaching charged particle would have the highest sticking probability at the end corresponding to the opposite surface charge and it would be highly improbable to find particles that would bind laterally to a heteroassembly. However, we cannot fully discount the possible role of the surface PEG molecules in also guiding this linear particle arrangement. At low PEG surface concentrations, such as 0.32 and 0.15 chains/nm^2 for the 7 nm and 13 nm GNP respectively, assemblies became more globular while still preserving the alternating structure between 7 nm and 13 nm particles. For the linear assemblies, it is possible that surface PEG molecules could be enriched in the equatorial position around the particles and their steric repulsion could prevent the lateral binding of other particles. Moreover, the possibilities that are discussed above are not mutually exclusive and all may contribute to the formation of linear heterostructures.

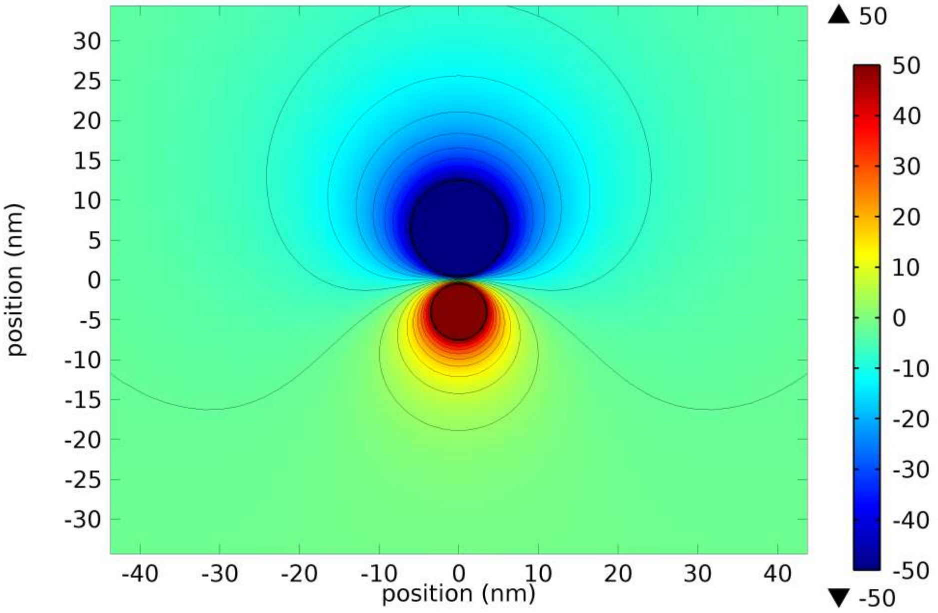

Figure 4.9: COMSOL simulation of the electrostatic potential surrounding a heterodimer. In this simulation, the boundary conditions of the particles were set to |50| mV. The colors represent the magnitude of the local electric potential and the contour lines represent equipotential levels.

Finally, experiments with particles at number ratios that deviate from 1:1 were also performed. When an excess of one type of particles are used, i.e. systems with 10:1 or 1:10 mixing ratios, there are several emerging scenarios. The first scenario is when the particles' surfaces were saturated with PEG; steric repulsion prevent any particles from clustering, and thus everything remained as monomers. The second scenario is when the surface concentration of PEG is high in both particles, but not saturated. In this case, clustering was still dominated by steric repulsion and heterodimers were formed, while the excess of the particles with larger population would remain as monomers. The third scenario is when the surface concentration of PEG is low enough to accommodate multi-particle binding. A population of trimers and monomers were observed because aggregation would be terminated at an early stage. TEM images of these systems are provided in the supporting information. We note that controlling the aggregation of oppositely charged colloids with an excess of one type particle has been previously studied and demonstrated[45]. Our present work focused on controlling aggregation by balancing electrostatic and steric interactions.

4.4 CONCLUSION

In this work, we have demonstrated that it is possible to balance electrostatic attraction and steric repulsion between two different types of oppositely charged GNPs by conjugating the surfaces with controlled amounts of oppositely charged thiols and surface-bound PEG molecules. This approach provides a facile, scalable and efficient method to produce controlled heteroassemblies of nanoparticles in large numbers. When no PEG molecules are bound to the particle surfaces and charged particles are mixed, large aggregates formed and sedimented. In the opposite limit, when large amounts of PEG molecules were bound to the particle surface, stable isolated individual particles were observed with no evident formation of heteroassemblies. In the region between these two extremes, it was demonstrated that it is possible to selectively create heterodimers and linear heteroassemblies of oppositely charged GNPs by tuning their steric repulsion. The yield of heterodimer synthesis was 66%, but it is anticipated that the conditions can likely be further optimized to provide an even larger yield by fine-tuning the PEG surface concentration on both particles. In contrast to other methods, this process can be carried out at room temperature, in aqueous media, with simple chemical functionalization. While gold was used in this work, the approach is flexible and can be extended to a wide variety of nanomaterials to enable advanced technologies. If iron oxide and palladium heterodoublets were synthesized, then these agents could be used as recoverable catalysts.[13] In contrast, if iron oxide and gold heterodoublets were synthesized, such agents would be potentially useful as medical imaging agents.[16] Therefore, this work represents a major step forward in the development of bottom-up methods for creating complex structures from nanoparticle sub-units.

4.5 SUPPORTING INFORMATION

Thermogravimetric Analysis (TGA) and Thiol Grafting Density Determination

TGA is a type of thermal analysis used to detect physical or chemical changes to a sample with heat. The mass of the sample is continuously monitored as a function of temperature and time. In this study, the mass of dried gold nanoparticles (GNP), grafted with thiols, is monitored as the temperature is ramped at 1 ºC/min, blanketed with nitrogen. When the thiol moieties decompose at a certain temperature, the loss in mass can be used to back-calculate the amount of thiol that was grafted onto the gold nanoparticles' surface. The gold nanoparticles were grafted with polyethylene glycol (PEG) and either 12-mercaptododecanoic acid (MDA) or (11-Mercaptoundecyl)-N,N,N-trimethylammonium bromide (MUTA). Since the decomposition temperature of PEG and that of the charged thiols (MUTA or MDA) are different, the loss in mass are not convoluted. The decay at 175 ºC can be attributed to the decomposition of MUTA or MDA, and the decay at 300 ºC can be attributed to PEG. Triplicates were performed, and the error of surface-bound PEG is less than 12 %. These uncertainties mostly arise from uncertainties in polymer/ligand dosing, which depends on the available surface area. Assuming complete reduction of gold ions, the concentration of the particle dispersion depends very strongly on the volume of each particle. Because the volume of a particle is proportional to R^3, small errors in particle size measurement lead to significant errors in concentration calculation, and in turn, available surface for thiol to bind.

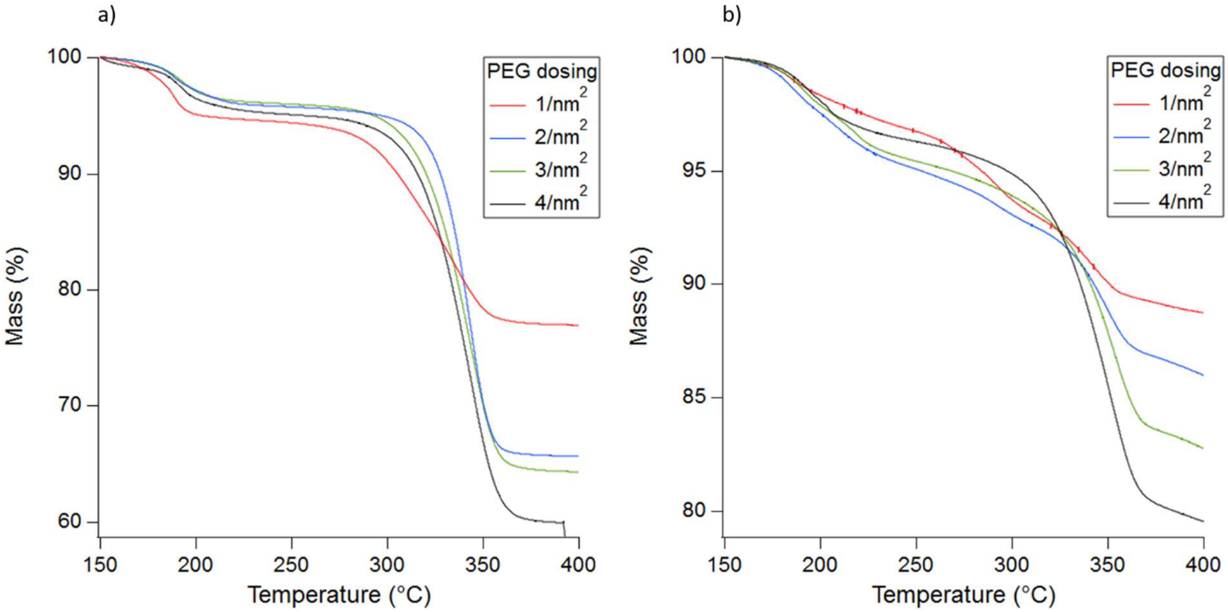

Figure 4.10: TGA curves of a) 7 nm GNP decorated with varying amounts of PEG and saturated with MUTA, b) 13 nm GNP decorated with varying amounts of PEG and saturated with MDA.

Zeta Potential Determination

After the particles were synthesized according to the procedure given in the main article, the PEG surface functionalization step was skipped, and the particles were functionalized with charged alkane thiols only; the 13 nm GNP was functionalized with negatively charged thiols while the 7 nm GNP was functionalized with positively charged thiols. Each sample was then dialyzed into a known 1 mM NaCl solution to remove excess charged thiols from the solution, and diluted by a factor of ten. The pH was adjusted using HCl or NaOH to the desired value, before measuring the zeta potential using Malvern Zetasizer Nano ZS in a folded capillary zeta cell. Figure 4.11 shows the pH regions of stability for different thiols where particles do not show signs of rapid aggregation. For a particular charged thiol, the zeta potential is constant throughout the whole region except near the pKa of the functional group, where the functional groups start to protonate/deprotonate and lose their charge. The pKa for carboxylic acids is about 4.5, and hence the 13 nm GNPs are not stable below this pH. The pKa for amines is about 9.5, and hence the 7 nm GNPS functionalized with 8A1O are not stable above this pH. GNPs functionalized with MUTA are stable even above pH of 12 because MUTA is a quaternary amine, and therefore there is no hydrogen to deprotonate, allowing the most flexible range of design. MDA has a larger zeta potential than MOA because MDA has a longer carbon chain, therefore minimizing the repulsive electrostatic interaction between adjacent thiols, and allowing it to pack more densely onto the nanoparticle surface. Although MSA has a short carbon chain, it carries two carboxylic groups per molecule, and hence the larger zeta potential value as well. Regions of pH where both amine functional groups and acid functional groups are charged are viable system conditions.

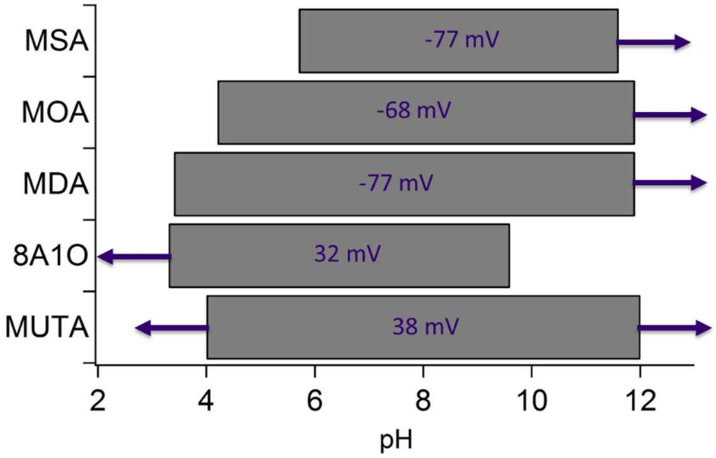

Figure 4.11: Regions of stability for GNPs functionalized with different thiols and their zeta potentials. Arrows indicate continued stability beyond the testing range.

TEM Images for Samples with Intermediate PEG Concentration

Figure 4.12 shows TEM images of samples with intermediate PEG concentration. Similar to Figure 4.6, the assemblies are alternating linear structures, despite a different PEG loading configuration.

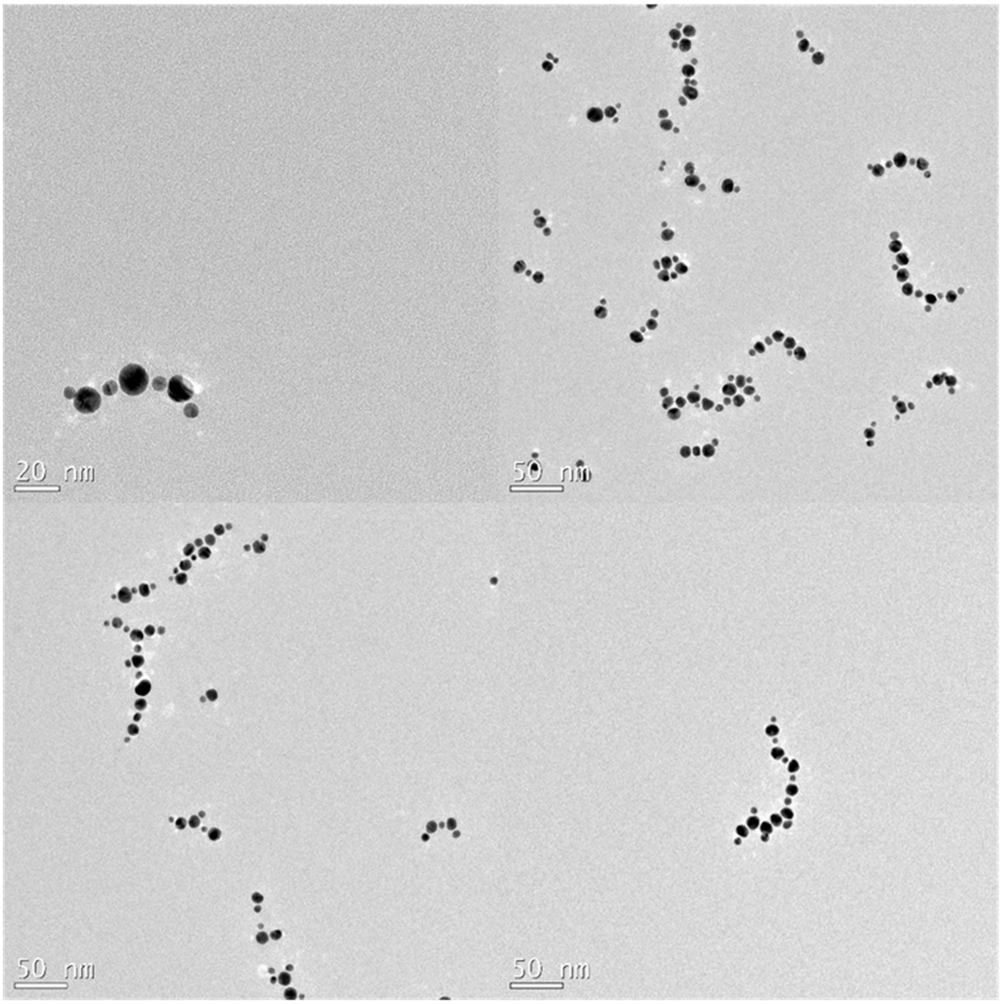

Figure 4.12: TEM images of a sample with particles mixed at a ratio of 1:1 (cationic : anionic) where the surface PEG concentration (10 kDa) corresponded to 0.66 and 0.15 chains/nm^2 on the 7 nm (cationic) and 13 nm (anionic) GNP, respectively.

TEM Images for Samples with no PEG functionalization

Rapid aggregation was observed for samples with no PEG functionalization; the sample quickly changes color to purple and sediments within a few hours. By quickly diluting with water after mixing of oppositely charged GNPs, this aggregation can be quenched, and subsequently deposited onto a TEM grid to be imaged (Figure 4.13). Still, the onset of uncontrolled aggregation is evident in these images.

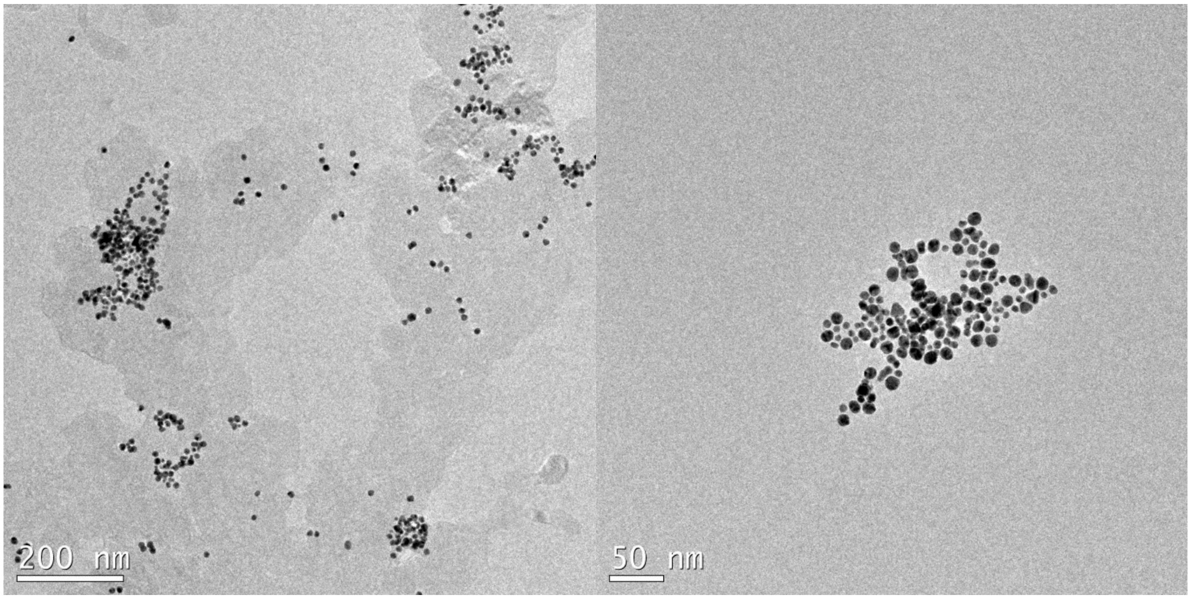

Figure 4.13: TEM images of a sample with particles mixed at a ratio of 1:1 (cationic : anionic) where there were no PEG functionalization. The sample was quickly diluted after mixing to quench the rapid aggregation. Still, evidence of the aggregation is indicated by the formation of large aggregates.

TEM Images for Samples with High PEG Concentration

At high PEG concentration, clusters are mostly doublets with some triplets. While the main article provides the tally of the cluster sizes, here we provide more TEM images from the sample (Figure 4.14).

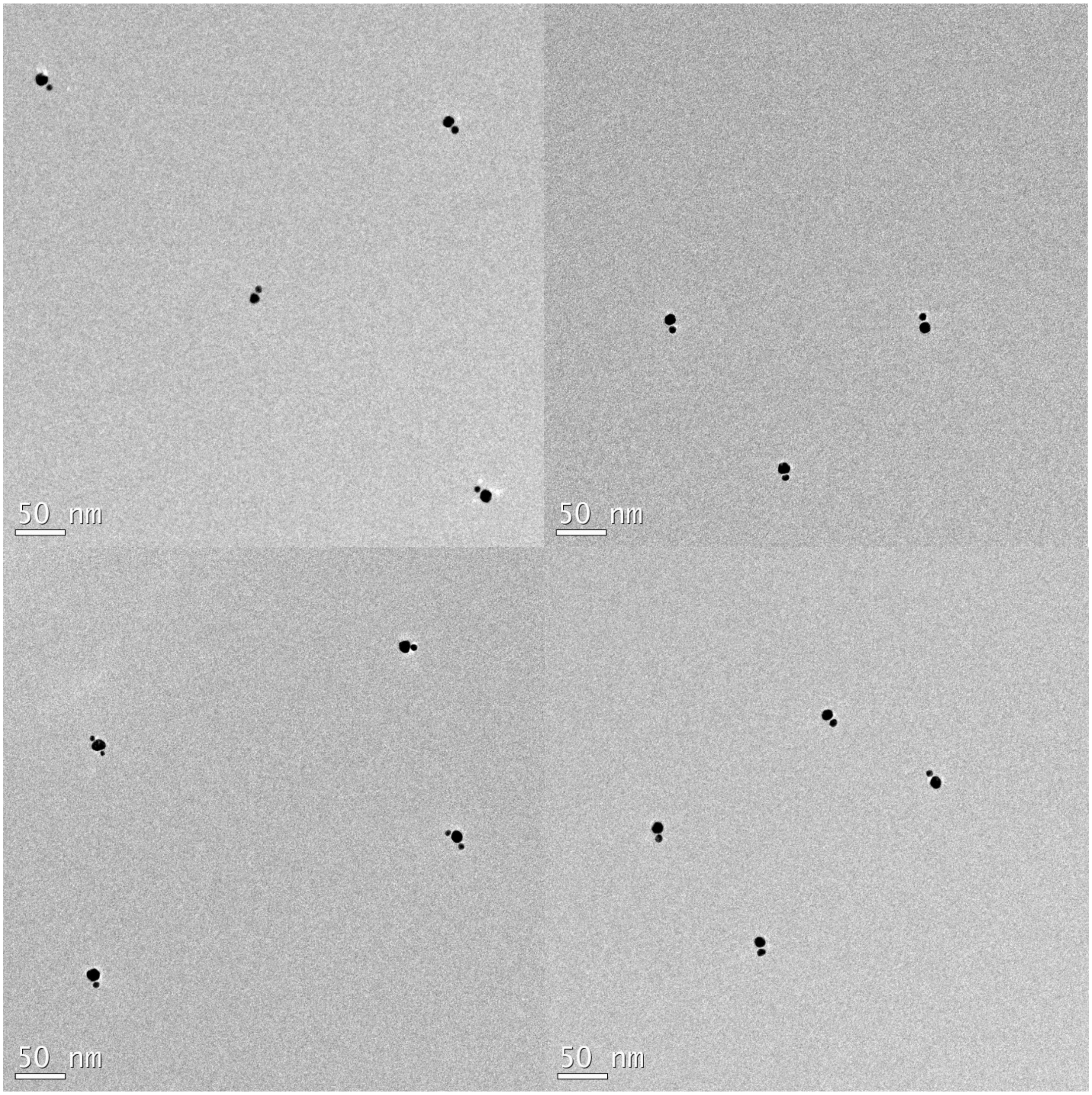

Figure 4.14: TEM images for a sample containing particles mixed at a ratio of 1:1 (cationic: anionic) that were loaded with 0.66 PEG/nm^2 and 0.43 PEG/nm^2 on the cationic 7 nm and anionic 13 nm GNP respectively.

TEM Images for Samples with Tenfold Excess of Cationic or Anionic Particles

Several experiments were performed where one type of particle is mixed in tenfold excess. At low concentration of PEG, an excess of the 7 nm GNPs results in the formations of flower like clusters, where the 7nm GNPs surround the 13 nm particles (Figure 4.16). This geometry is not observed if the 13 nm GNPs are in excess instead; doublets are formed (Figure 4.15). At a low PEG concentration, the interactions are dominated by electrostatics, and the larger particles carry a larger amount of charge. With an excess of 7nm GNPs, a 13 nm GNP will continue attracting 7 nm GNPs until the overall charge is neutralized. On the other hand, with an excess of 13 nm GNPs, having one anionic 13 nm GNP bind to a cationic 7 nm GNP is enough to completely make the cluster anionic.

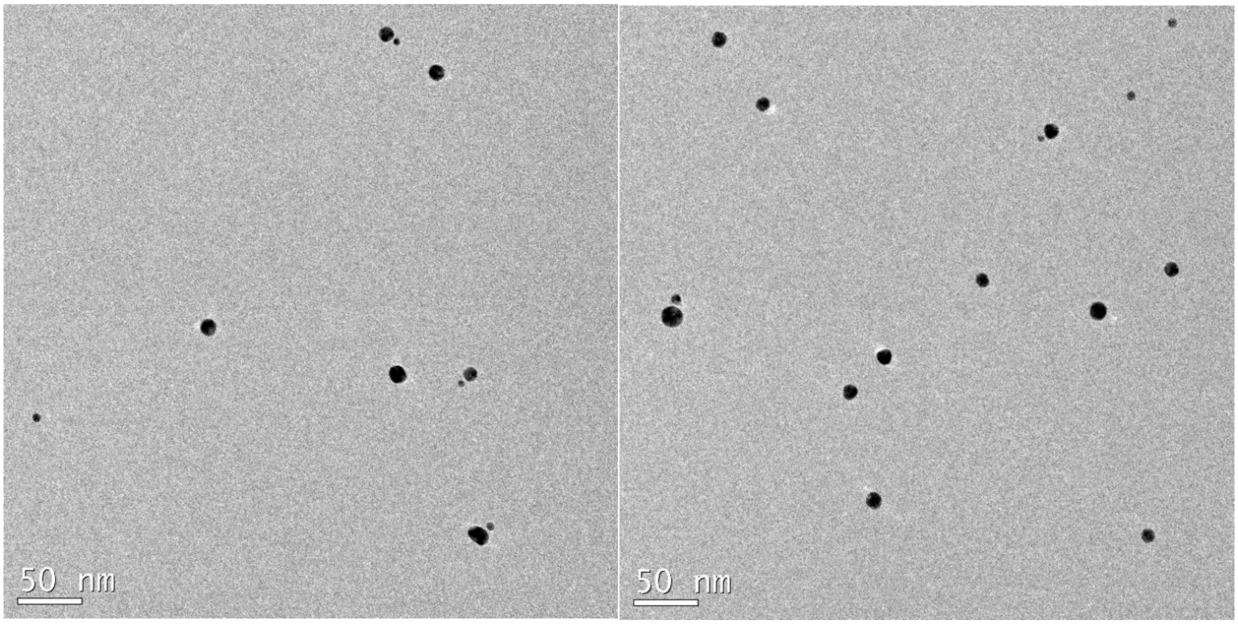

Figure 4.15: TEM images for a sample containing particles with tenfold excess of 13 nm GNPs. Samples were loaded with 0.32 PEG/nm^2 and 0.15 PEG/nm^2 on the cationic 7 nm and anionic 13 nm GNP respectively.

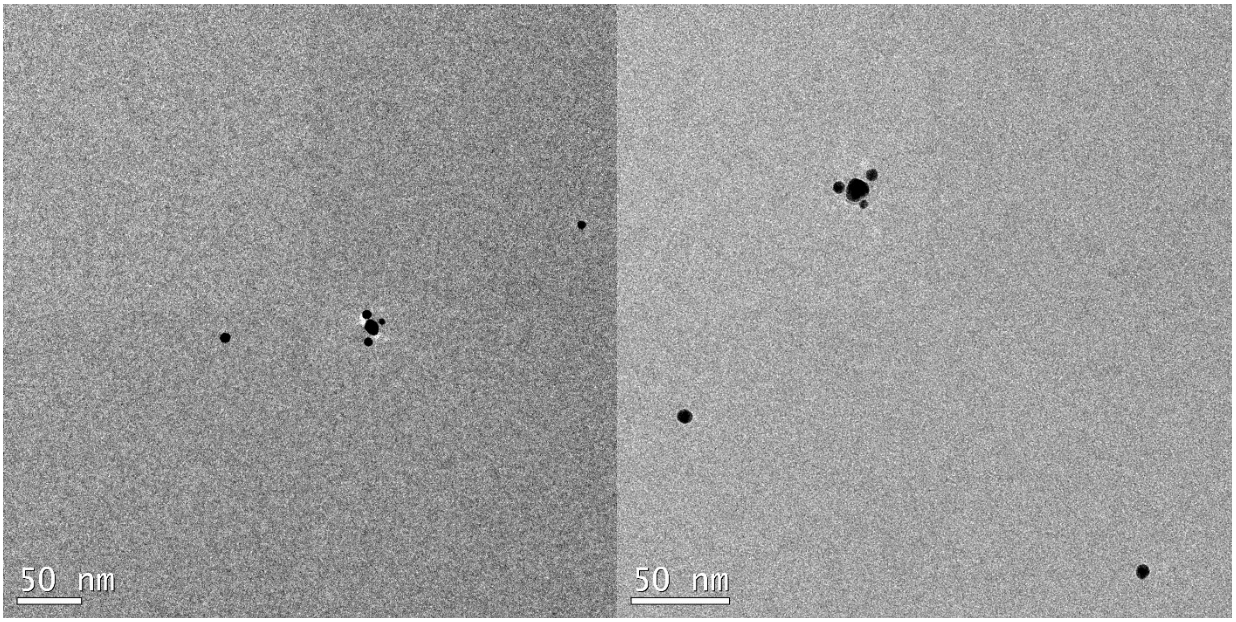

Figure 4.16: TEM images for a sample containing particles with tenfold excess of 7 nm GNPs. Samples were loaded with 0.32 PEG/nm^2 and 0.15 PEG/nm^2 on the cationic 7 nm and anionic 13 nm GNP respectively.

At intermediate PEG concentration, multi particle binding is still observed. With an excess of 13 nm GNPs, again only doublets were formed (Figure 4.17). On the other hand, an excess of 7 nm GNPs led to the formation of triplets and singlets of the 7 nm GNPs (Figure 4.18). Upon the formation of a triplet, there is a lack of 13 nm GNPs to continue the chain, and the aggregation is halted. This is remarkably different from the case when the ratio of the particles is 1:1, where long linear heteroaggregates were formed.

At high PEG concentration, PEG dominates the particle interactions. Regardless of the number of particles in solution, the heavy coating of PEG allows only the formation of doublets (Figure 4.19, Figure 4.20)

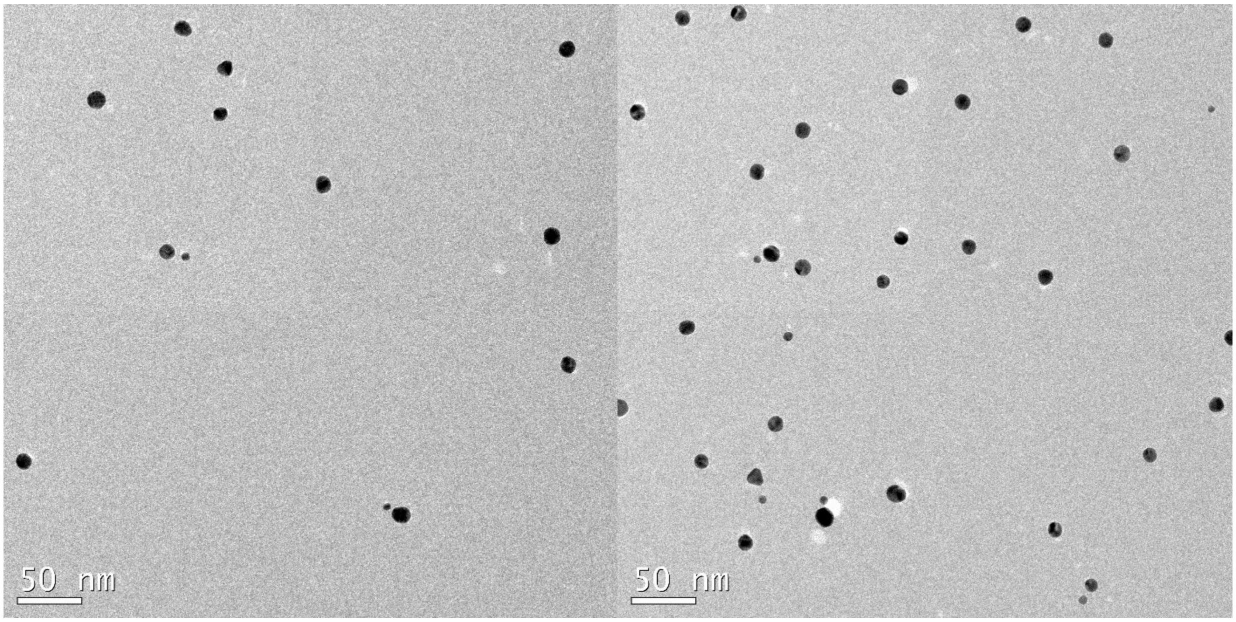

Figure 4.17: TEM images for a sample containing particles with tenfold excess of 13 nm GNPs. Samples were loaded with 0.32 PEG/nm^2 and 0.31 PEG/nm^2 on the cationic 7 nm and anionic 13 nm GNP respectively.

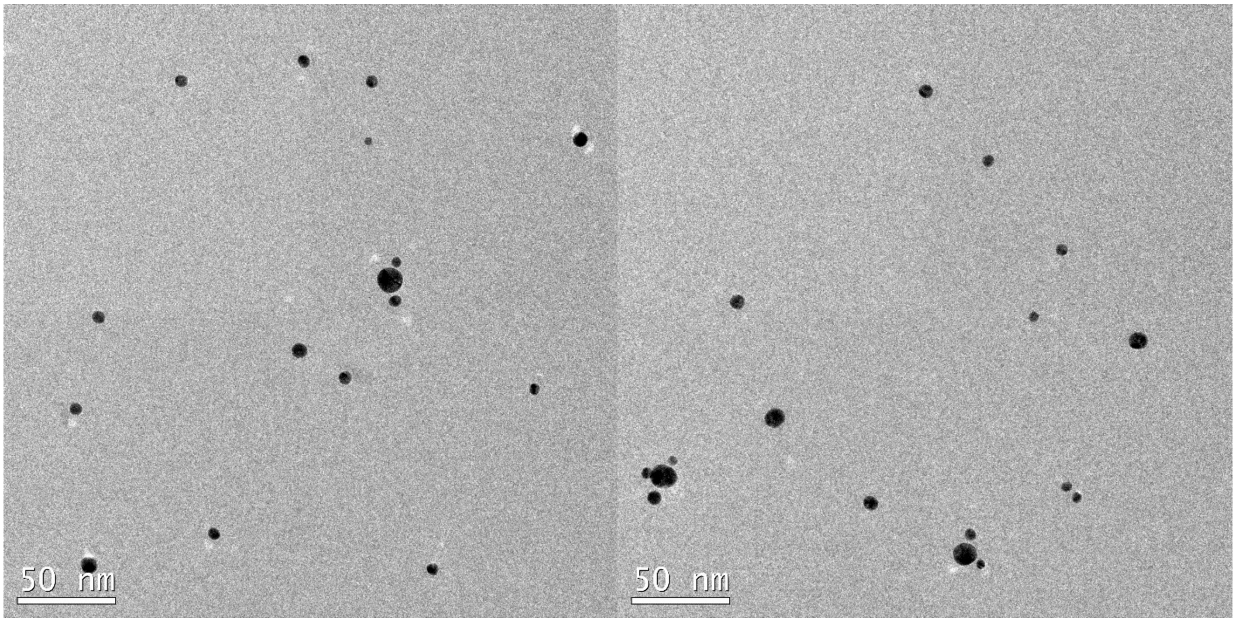

Figure 4.18: TEM images for a sample containing particles with tenfold excess of 7 nm GNPs. Samples were loaded with 0.32 PEG/nm^2 and 0.31 PEG/nm^2 on the cationic 7 nm and anionic 13 nm GNP respectively.

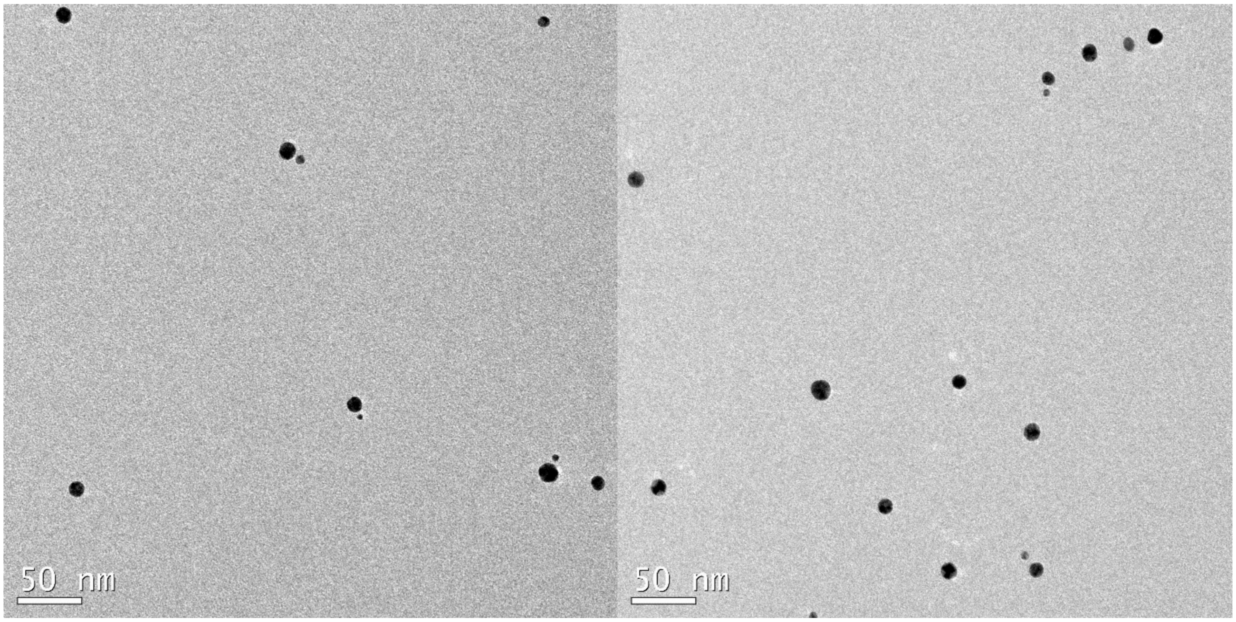

Figure 4.19: TEM images for a sample containing particles with tenfold excess of 13 nm GNPs. Samples were loaded with 0.66 PEG/nm^2 and 0.43 PEG/nm^2 on the cationic 7 nm and anionic 13 nm GNP respectively.

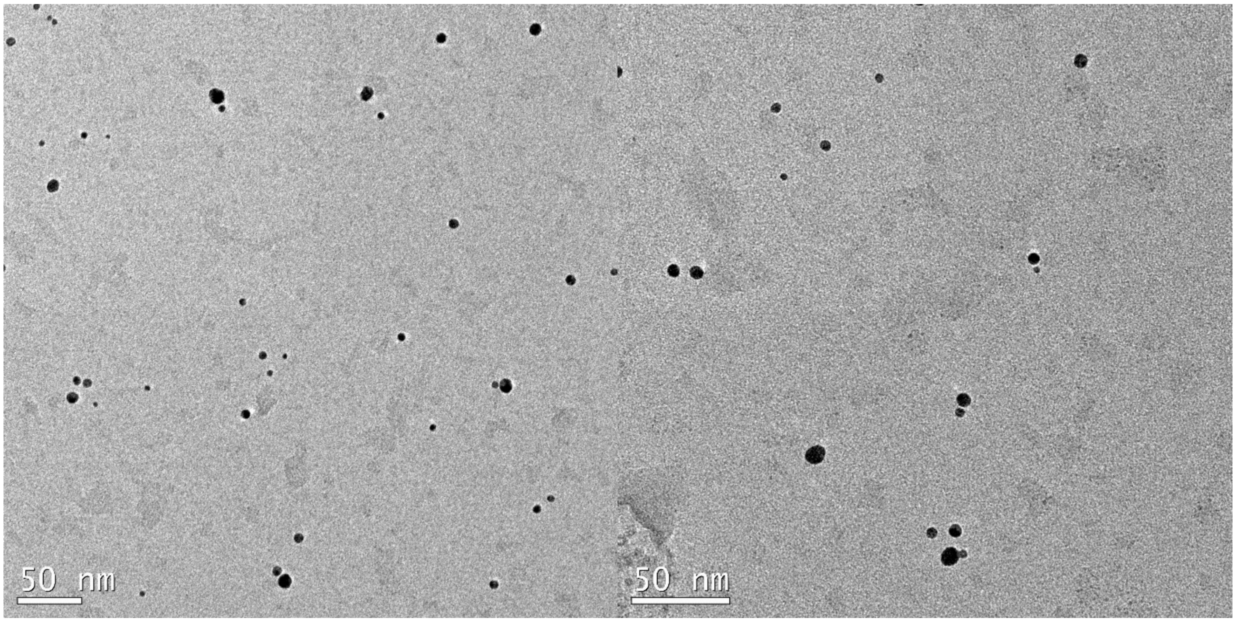

Figure 4.20: TEM images for a sample containing particles with tenfold excess of 7 nm GNPs. Samples were loaded with 0.66 PEG/nm^2 and 0.43 PEG/nm^2 on the cationic 7 nm and anionic 13 nm GNP respectively.

Gold Nanoparticle Synthesis: Complete Reduction of Gold Ions

SAXS was performed on freshly synthesized 13 nm and 7nm GNPs in absolute scale. The resulting scattering profiles were fit to the sphere model (Figure 4.21), and the volume fraction of the dispersion can be obtained. Assuming complete reduction of gold ions and bulk density of gold, the calculated volume fraction of gold is in very good agreement with the volume fraction obtained from SAXS data fitting (Table 4.3).

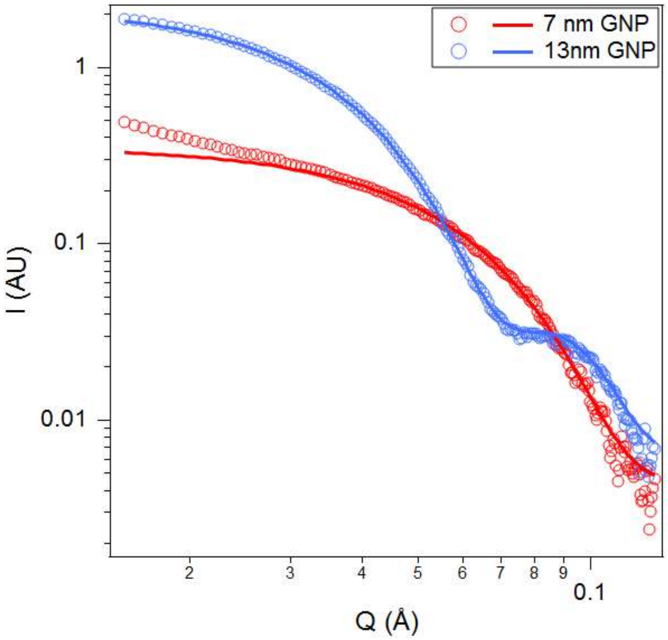

Figure 4.21: SAXS profiles of freshly synthesized 13 nm and 7 nm GNPs in absolute scale, and their corresponding model fits.

Table 4.3: Comparison of volume fraction obtained from calculation and from SAXS profile fitting.

	Calculated Volume Fraction	SAXS Volume Fraction
7 nm GNP	5.10×10^{-6}	5.26×10^{-6}
13 nm GNP	1.02×10^{-5}	1.15×10^{-5}

4.6 REFERENCES

(1) Ozbay, E. Plasmonics : Merging Photonics and Electronics at Nanoscale Dimensions. *Science* **2006**, *311*, 189–193.

(2) Ku, K. H.; Shin, J. M.; Kim, M. P.; Lee, C.-H.; Seo, M.-K.; Yi, G.-R.; Jang, S. G.; Kim, B. J. Size-Controlled Nanoparticle-Guided Assembly of Block Copolymers for Convex Lens-Shaped Particles. *J. Am. Chem. Soc.* **2014**.

(3) Lee, J.; Govorov, A. O.; Kotov, N. A. Nanoparticle Assemblies with Molecular Springs: A Nanoscale Thermometer. *Angew. Chemie - Int. Ed.* **2005**, *44*, 7439–7442.

(4) Lee, J.; Hernandez, P.; Govorov, A. O.; Kotov, N. A. Exciton-Plasmon Interactions Inmolecular Spring Assemblies of Nanowires and Wavelength-Based Protein Detection. *Nat. Mater.* **2007**, *6*, 291–295.

(5) Lee, J. S.; Han, M. S.; Mirkin, C. A. Colorimetric Detection of Mercuric Ion (Hg2+) in Aqueous Media Using DNA-Functionalized Gold Nanoparticles. *Angew. Chemie - Int. Ed.* **2007**, *46*, 4093–4096.

(6) Elghanian, R.; Storhoff, J. J.; Mucic, R. C.; Letsinger, R. L.; Mirkin, C. a. Selective Colorimetric Detection of Polynucleotides Based on the Distance-Dependent Optical Properties of Gold Nanoparticles. *Science* **1997**, *277*, 1078–1081.

(7) Nie, S. Probing Single Molecules and Single Nanoparticles by Surface-Enhanced Raman Scattering. *Science* **1997**, *275*, 1102–1106.

(8) Tseng, R. J.; Tsai, C.; Ma, L.; Ouyang, J.; Ozkan, C. S.; Yang, Y. Digital Memory Device Based on Tobacco Mosaic Virus Conjugated with Nanoparticles. *Nat. Nanotechnol.* **2006**, *1*, 72–77.

(9) Sun; Murray; Weller; Folks; Moser. Monodisperse FePt Nanoparticles and Ferromagnetic FePt Nanocrystal Superlattices. *Science* **2000**, *287*, 1989–1992.

(10) Hoinville, J.; Bewick, A.; Gleeson, D.; Jones, R.; Kasyutich, O.; Mayes, E.; Nartowski, A.; Warne, B.; Wiggins, J.; Wong, K. High Density Magnetic Recording on Protein-Derived Nanoparticles. *J. Appl. Phys.* **2003**, *93*, 7187–7189.

(11) Bao, J.; Chen, W.; Liu, T.; Zhu, Y.; Jin, P.; Wang, L.; Liu, J.; Wei, Y.; Li, Y. Bifunctional Au-Fe 3 O 4 Nanoparticles for Protein Separation. *ACS Nano* **2007**, *1*, 293–298.

(12) Abu-Reziq, R.; Wang, D.; Post, M.; Alper, H. Platinum Nanoparticles Supported on Ionic Liquid-Modified Magnetic Nanoparticles: Selective Hydrogenation Catalysts. *Adv. Synth. Catal.* **2007**, *349*, 2145–2150.

(13) Jang, Y.; Chung, J.; Kim, S.; Jun, S. W.; Kim, B. H.; Lee, D. W.; Kim, B. M.; Hyeon, T.

Simple Synthesis of Pd-Fe3O4 Heterodimer Nanocrystals and Their Application as a Magnetically Recyclable Catalyst for Suzuki Cross-Coupling Reactions. *Phys. Chem. Chem. Phys.* **2011**, *13*, 2512–2516.

(14) Fan, J. a; Wu, C.; Bao, K.; Bao, J.; Bardhan, R.; Halas, N. J.; Manoharan, V. N.; Nordlander, P.; Shvets, G.; Capasso, F. Self-Assembled Plasmonic Nanoparticle Clusters. *Science* **2010**, *328*, 1135–1138.

(15) Brown, L. V.; Sobhani, H.; Lassiter, J. B.; Nordlander, P.; Halas, N. J. Heterodimers: Plasmonic Properties of Mismatched Nanoparticle Pairs. *ACS Nano* **2010**, *4*, 819–832.

(16) Xu, C.; Xie, J.; Ho, D.; Wang, C.; Kohler, N.; Walsh, E. G.; Morgan, J. R.; Chin, Y. E.; Sun, S. Au-Fe3O4 Dumbbell Nanoparticles as Dual-Functional. *Angew. Chemie - Int. Ed.* **2008**, *47*, 173–176.

(17) Carbone, L.; Cozzoli, P. D. Colloidal Heterostructured Nanocrystals: Synthesis and Growth Mechanisms. *Nano Today* **2010**, *5*, 449–493.

(18) Wang, C.; Xu, C.; Zeng, H.; Sun, S. Recent Progress in Syntheses and Applications of Dumbbell-like Nanoparticles. *Adv. Mater.* **2009**, *21*, 3045–3052.

(19) Mucic, R. C.; Storhoff, J. J.; Mirkin, C. A.; Letsinger, R. L. DNA-Directed Synthesis of Binary Nanoparticle Network Materials. *Journal of the American Chemical Society*. 1998, pp 12674–12675.

(20) Casavola, M.; Buonsanti, R.; Caputo, G.; Cozzoli, P. D. Colloidal Strategies for Preparing Oxide-Based Hybrid Nanocrystals. *Eur. J. Inorg. Chem.* **2008**, No. 6, 837–854.

(21) Sun, S.; Yu, H.; Wang, S. X. Dumbbell-like Nanoparticles and a Process of Forming the Same. US 2006/0053971 A1, 2006.

(22) Fu, Q.; Sheng, Y.; Tang, H.; Zhu, Z.; Ruan, M.; Xu, W.; Zhu, Y.; Tang, Z. Growth Mechanism Deconvolution of Self-Limiting Supraparticles Based on Microfluidic System. *ACS Nano* **2015**, *9*, 172–179.

(23) Yan, N.; Liu, H.; Zhu, Y.; Jiang, W.; Dong, Z. Entropy-Driven Hierarchical Nanostructures from Cooperative Self-Assembly of Gold Nanoparticles/Block Copolymers under Three-Dimensional Confinement. *Macromolecules* **2015**, *48*, 5980–5987.

(24) Stover, R. J.; Moaseri, E.; Gourisankar, S. P.; Iqbal, M.; Rahbar, N. K.; Changalvaie, B.; Truskett, T. M.; Johnston, K. P. Formation of Small Gold Nanoparticle Chains with High NIR Extinction through Bridging with Calcium Ions. *Langmuir* **2016**, *32*, 1127–1138.

(25) Stover, R. J.; Murthy, A. K.; Nie, G. D.; Gourisankar, S.; Dear, B. J.; Truskett, T. M.; Sokolov, K. V; Johnston, K. P. Quenched Assembly of NIR-Active Gold Nanoclusters Capped with Strongly Bound Ligands by Tuning Particle Charge via PH and Salinity. *J. Phys. Chem. C* **2014**, *118*, 14291–14298.

(26) Larson-Smith, K.; Pozzo, D. C. Scalable Synthesis of Self-Assembling Nanoparticle Clusters Based on Controlled Steric Interactions. *Soft Matter* **2011**, *7*, 5339–5347.

(27) Frens, G. Controlled Nucleation for the Regulation of the Particle Size in Monodisperse Gold Suspensions. *Nat. Phys. Sci.* **1973**, *241*, 20–22.

(28) Martin, M. N.; Basham, J. I.; Chando, P.; Eah, S. K. Charged Gold Nanoparticles in Non-Polar Solvents: 10-Min Synthesis and 2D Self-Assembly. *Langmuir* **2010**, *26*, 7410–7417.

(29) Luedtke, W. D.; Landman, U. Structure, Dynamics, and Thermodynamics of Passivated Gold Nanocrystallites and Their Assemblies. *J. Phys. Chem.* **1996**, *100*, 13323–13329.

(30) Luedtke, W. D.; Landman, U. Structure and Thermodynamics of Self-Assembled Monolayers on Gold Nanocrystallites. *J Phy chem B* **1998**, *5647*, 6566–6572.

(31) Love, J. C.; Estroff, L. A.; Kriebel, J. K.; Nuzzo, R. G.; Whitesides, G. M. Self-Assembled Monolayers of Thiolates on Metals as a Form of Nanotechnology. *Chem. Rev.* **2005**, *105*, 1103–1170.

(32) Hinterwirth, H.; Kappel, S.; Waitz, T.; Lindner, W.; Lämmerhofer, M.; Morgenstelle, A. Der. Quantifying Thiol Ligand Density of Self-Assembled Monolayers on Gold Nanoparticles by Inductively Coupled Plasma Mass Spectrometry Quantifying Thiol Ligand Density of Self-Assembled Monolayers on Gold Nanoparticles by Inductively Coupled Plasma Mass Spec. *ACS Nano* **2013**, *7*, 1129–1136.

(33) Larson-smith, K.; Pozzo, D. C. Competitive Adsorption of Thiolated Poly(Ethylene Glycol) and Alkane-Thiols on Gold Nanoparticles and Its E Ff Ect on Cluster Formation. *Langmuir* **2012**, *28*, 13157–13165.

(34) Bain, C. D.; Evall, J.; Whitesides, G. M. Formation of Monolayers by the Coadsorption of Thiols on Gold: Variation in the Head Group, Tail Group, and Solvent. *J. Am. Chem. Soc.* **1989**, *111*, 7155–7164.

(35) Laibinis, P.; Fox, M.; Folkers, J.; Whitesides, G. Comparisons of Self-Assembled Monolayers on Silver and Gold: Mixed Monolayers Derived from HS (CH2) 21X and HS (CH2) 10Y (X, Y= CH3, CH2OH) Have Similar. *Langmuir* **1991**, *7*, 3167–3173.

(36) Chung, C.; Lee, M. Exchange of Self-Assembled Thiol Monolayers on Gold: Characterization by FT-IR External Reflection Spectroscopy. *J. Electroanal. Chem.* **1999**, *468*, 91–97.

(37) Schlenoff, J. B.; Li, M.; Ly, H. Stability and Self-Exchange in Alkanethiol Monolayers. *J. Am. Chem. Soc.* **1995**, *117*, 12528–12536.

(38) Collard, D. M.; Fox, M. A. Use of Electroactive Thiols to Study the Formation and Exchange of Alkanethiol Monolayers on Gold. *Langmuir* **1991**, *7*, 1192–1197.

(39) Nishida, N.; Hara, M.; Sasabe, H.; Knoll, W. Formation and Exchange Processes of

Alkanethiol Self-Assembled Monolayer on Studied by Thermal Desorption Spectroscopy and Scanning Tunneling Microscopy Au (111). *Japanese J. Appl. Physics, Part 1* **1997**, *36*, 2379–2385.

(40) Hostetler, M. J.; Templeton, A. C.; Murray, R. W. Dynamics of Place-Exchange Reactions on Monolayer-Protected Gold Cluster Molecules. *Langmuir* **1999**, *15*, 3782–3789.

(41) Sader, J. E.; Carnie, S. L.; Chan, D. Y. C. Accurate Analytic Formulas for the Double-Layer Interaction between Spheres. *J. Colloid Interface Sci.* **1995**, *171*, 46–54.

(42) Hamaker, H. C. The London--Van Der Waals Attraction Between Spherical Particles. *Phys. IV* **1937**, *10*.

(43) Gschneidtner, T. A.; Fernandez, Y. A. D.; Syrenova, S.; Westerlund, F.; Langhammer, C.; Moth-Poulsen, K. A Versatile Self-Assembly Strategy for the Synthesis of Shape-Selected Colloidal Noble Metal Nanoparticle Heterodimers. *Langmuir* **2014**, *30*, 3041–3050.

(44) Kim, A. Y.; Berg, J. C. Fractal Aggregation: Scaling of Fractal Dimension with Stability Ratio. *Langmuir* **2000**, *16*, 2101–2104.

(45) Kim, A.; Berg, J. Fractal Heteroaggregation of Oppositely Charged Colloids. *J. Colloid Interface Sci.* **2000**, *229*, 607–614.

(46) Kim, A. Y.; Hauch, K. D.; Berg, J. C.; Martin, J. E.; Anderson, R. A. Linear Chains and Chain-like Fractals from Electrostatic Heteroaggregation. *J. Colloid Interface Sci.* **2003**, *260*, 149–159.

Chapter 5. PROPERTIES AND STRUCTURE OF LUDOX/ALKYLSILANE XEROGEL WITH CONTROLLED POROSITY

5.1 INTRODUCTION

This work resulted from a collaboration with Membrion, a startup company that spun out of the Pozzo group during my time as a PhD student. This company aims to develop ceramic-based ion exchange membranes for target applications in flow batteries, where the membrane needs to be permeable for hydrogen ions, but not to ionic redox active species, while also being stable in a highly acidic and oxidative environment. The current gold standard, a perfluorosulfonic acid polymer membrane called Nafion, has good chemical stability and is proton conductive, but it is also exceedingly expensive and has subpar ion selectivity. As an alternative, ceramics represent a viable class of materials due to their high thermal and chemical stability, and highly tunable pore sizes. Unfortunately, however, they are also brittle and handling these thin ceramic membranes for transport and installation is very challenging. The goal of this project was to develop new formulations that could improve the mechanical properties of these ceramics while preserving the desired ion transport and stability.

Ceramics are often synthesized using the sol-gel process, a method to form solid ceramics from molecular precursors, namely metal alkoxides. The sol-gel process has been extensively studied, with special emphasis on silicates, and much of the material is collected in a seminal book by Brinker and Scherer.[1] In a typical sol-gel process, alkoxysilane percursors, such as tetraethylorthosilicate (TEOS), are mixed with water and alcohol as a cosolvent. The alkoxysilanes are hydrolyzed and subsequently condensed to form siloxane bonds. Monomers become dimers, then trimers, and eventually form larger particles. These particles aggregate and form a three-dimensional gel network that, when dried, becomes a nanoporous material.[2] The properties of the final product are dependent on the underlying structure, which is in turn dependent on reaction conditions, including pH and water content, among many others.[2–4]

The sol-gel process is flexible and organic entities can be included in the process to create hybrid inorganic-organic materials, also known as ormocers (organically modified ceramics), or in the case of silicates, ormosils. The organic components can be polymers or monomers, such as organosilanes which are typically used in coating applications.[5] The organic components can also co-polymerize with metal alkoxides or simply be dispersed within the matrix. There are a couple of advantages in including organic components in ceramics. First, it opens the material to a wide range of applications: optical materials,[6–9] ferroelectric materials,[10–12], and separation membranes,[13–16] among others. Secondly, introducing organics reduces the tendency to crack when drying thin films and enhances mechanical properties of the material.[5,17]

Numerous systematic investigations have been performed to characterize the mechanical properties of ormocers with polymers as the organic component.[18–21] The general trend for these materials are as expected: higher organic content results in more flexible materials, reducing brittleness, at the cost of tensile strength, and larger amount of crosslinking between the phases results in higher elastic modulus. In contrast, fewer systematic studies have been performed where the organic components are monomers. Etienne et al. studied the mechanical properties of films prepared from (3-glycidyloxypropyl)trimethoxysilane (GLYMO) and either TEOS or silica nanoparticles. They found that increasing silica content in the range 0-30 % mass fraction increases elastic modulus.[22] Douce et al. studied the effect of particle size and surface conditions of nanoparticles on the mechanical properties of ormosil films. Similarly, they found a positive correlation between elastic modulus and volume fraction of particle fillers, up to 15 % volume fraction, but there was no significant difference in elastic modulus between films made out of different particle sizes. In both of these studies, the inorganic fraction is low, and they act as fillers in a predominantly organic matrix.

Palmisano et al. synthesized thin films synthesized out of MTMS and tetramethylorthosilicate (TMOS), varying the composition from 0 – 100 % MTMS.[23] They found that elastic modulus is positively correlated proportional with the amount of TMOS throughout the whole compositional range, confirming the results of the two previously cited works for materials with high monomeric inorganic content. If nanoparticles are included in the material, the results are slightly different. Malzbender studied the mechanical properties of films synthesized out of TEOS and methyltrimethoxysilane (MTMS) with silica or alumina nanoparticle fillers. The amount of fillers was varied from 0-69 % volume, while the ratio of TEOS to MTMS was kept constant. At low filler content, the results were consistent, i.e. higher filler content results in higher elastic modulus. At higher filler content, where the volume fraction of the alumina particles exceeds approximately 45 %, there is a plateau in elastic modulus. It is unclear how elastic modulus would vary at even higher nanoparticle content.

In this work, the mechanical properties and structures of ormosils with high inorganic nanoparticle content were investigated. The materials were prepared using LUDOX particles and alkylsilanes. Both the amount and the type of alkylsilanes was varied, namely ethyltriethoxysilane (ETES), butyltriethoxysilane (BTES), hexyltriethoxysilane (HTES), and diethyldiethoxysilane (DEDES). Nano-scale structures were probed using small angle x-ray scattering (SAXS) to explain the observed mechanical properties.

5.2 EXPERIMENTAL

TEOS and LUDOX SM-30 were obtained from Sigma Aldrich (St Louis, MO). ETES, BTES, HTES, and DEDES were obtained from Gelest (Morrisville, PA). Hydrochloric acid (HCl) was obtained from Macron Fine Chemicals (Center Valley, PA). Type A/E glass fiber filter paper with 330 μm thickness was obtained from Pall Corporation (Port Washington, NY). All chemicals were used as received.

The dependence of gel time on pH was investigated. Between 67-75 μL of concentrated HCl was added to 3 mL of Ludox SM-30 to tune the pH between 4.9 and 2.1. Gelation is determined visually, and the sol is considered to have gelled when the dispersions no longer flow when the container is inverted.

A schematic of the sol synthesis process is shown in Figure 5.1a. In a typical synthesis, 3 mL of LUDOX dispersion is added into a 20 mL scintillation vial. While vigorously stirred, 69 μL or 75 μL of concentrated acid, 5 mL of ethanol, and 0-1 mL of alkylsilane are added in rapid succession. After stirring for 5 minutes, the mixture is ready for sample preparation. It is critical to add the acid into LUDOX first before adding ethanol. If ethanol is added first, the dispersion will gel within seconds. It is also important to add ethanol and alkyltriethoxysilane quickly after adding the acid to dilute the LUDOX particles and prevent premature gelation of the mixture.

SAXS samples are prepared by transferring the mixture into an aluminum trough with Kapton tape as the base (Figure 5.1b). The trough is placed in a plastic petri dish, and the petri dish is capped using its lid. The petri dish is left in ambient air for 24 hours and placed in an oven at 60 °C for 12 hours. Vacuum is pulled from the oven, and the sample is left in the oven for an additional 12 hours. SAXS experiments are performed on Anton Paar SAXSess benchtop instrument with a

Cu-K_α line-collimated beam. The beam path is normal to the base of the trough. The scattering contribution of Kapton background is also subtracted.

To prepare samples for mechanical measurements, filter paper is cut into 30 mm x 30 mm square pieces. The gel precursor mixture is transferred to a petri dish, and the filter paper is soaked in the mixture for 2 minutes. The filter paper is slowly drawn out of the mixture, minimizing excess mixture on filter paper surface, and laid flat over a Teflon plate. Similar to the sample preparation for SAXS, the Teflon plate is left in ambient air for 24 hours and placed in an oven at 60 °C for 12 hours. Vacuum is pulled from the oven, and the sample is left to dry for an additional 12 hours. A 15 mm x 15 mm square is cut out from the center of the 30 mm x 30 mm square using a laser cutter. This inner square piece is the sample used for three-point flexural test. The support span is 10 mm, and the loading pin is lowered at 1 mm/min. The toe region at low strain is removed and the strain is corrected such that extrapolation of the linear region crosses the origin.

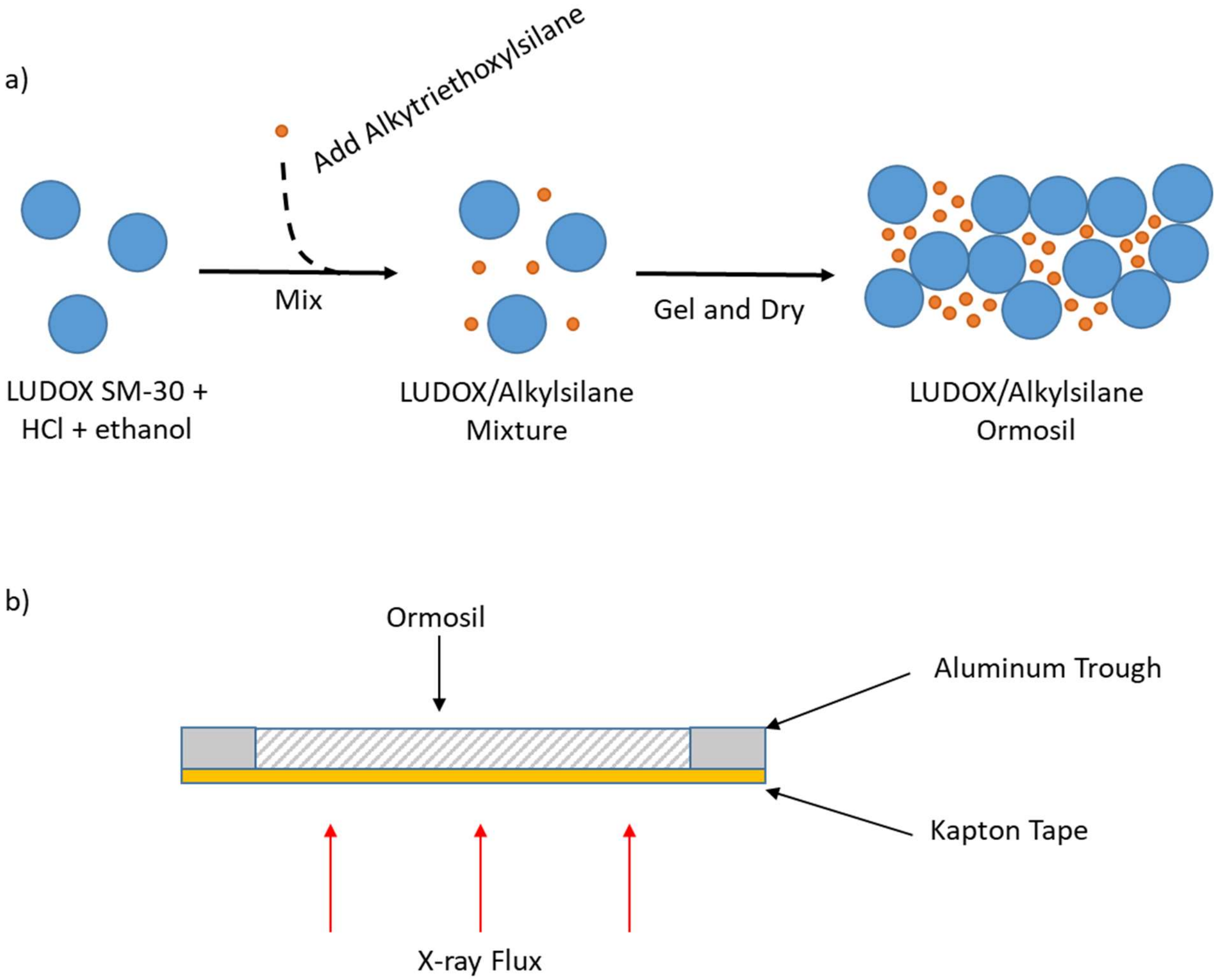

Figure 5.1: a) Schematic of the synthesis of LUDOX/alkylsilane ormosils. b) Schematic of sample preparation for SAXS experiments.

5.3 RESULTS AND DISCUSSION

LUDOX SM-30 particles come from the manufacturer at pH 10, where the silica particles have sufficient negative surface charge to be stable against aggregation and gelation. When mixing the components, using 67-75 µL of concentrated HCl tunes the pH of the mixture over a range of 4.9-2.1, as measured by a pH meter. The pH dependence on gel time is shown in Figure 5.2. The time to gel is largest for pH 2.1 and decreases exponentially as the pH increases towards 4.9, similar to the gelation of sols synthesized from TEOS.[24] A similar study was performed using LUDOX SM-30 particles instead of TEOS. Even though the PZC of silica is close to 2, gelation is slow at pH 2 because condensation reaction is minimized at this pH. The rate of condensation can be thought of as the sticking probability of particles upon collision. The low sticking probability allows the particles and fractals to slip past each other to form denser structures upon drying.[3] On the other hand at pH 4, gelation is much faster, leading to more open structures. In this work, pH 2.1 was chosen to minimize the pore size since this project was motivated by proton selective membrane applications. Unfortunately, a system containing both particles and monomeric silanes are not as simple to describe. Interactions between monomers and particles involve competing hydrolysis, condensation, polymerization, and adsorption of the monomer onto the particle surface.[25] Kinetics of hydrolysis and condensation are altered, and adsorption behavior are complex.[26,27] Still, the mechanical properties of ormosils synthesized with these alkylsilanes can be compared.

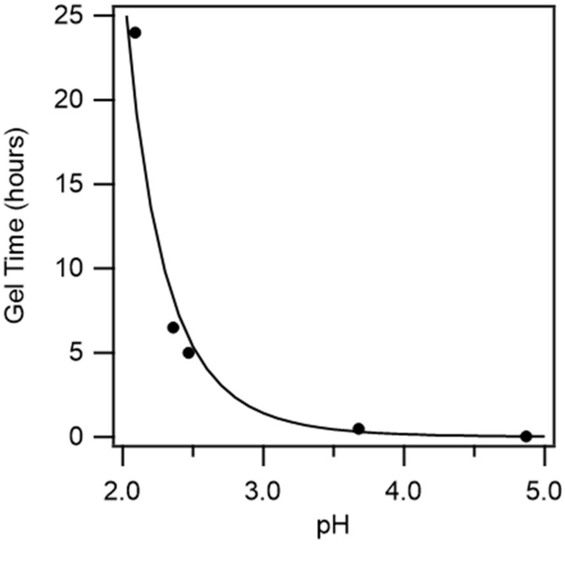

Figure 5.2: Dependence of LUDOX SM-30 gel time on pH.

To investigate the effect of adding alkylsilane on the mechanical properties of the composite, 250 µL, 500 µL, or 1 mL of ETES was added into the sol formulation (Figure 5.3). Assuming complete hydrolysis and condensation of ETES into $SiO_{1.5}(C_2H_5)$, the volume fraction of the silane in the dried material is 0-38 %. The volume occupied by LUDOX particles was calculated assuming a density of amorphous silica, 2.2 g/cm^3. The volume occupied by $SiO_{1.5}(C_2H_5)$ was estimated in the following way. Each ETES molecule has three hydrolysable ethoxy groups. Upon complete hydrolysis and condensation, 3 mol of ethanol are released and 1.5 mol of water are incorporated for every mol of Si. Thus, the volume occupied by 1 mol of $SiO_{1.5}(C_2H_5)$ is the volume of 1 mol of ETES subtracted by the volume occupied by three mol of ethanol plus the volume occupied by 1.5 mol of water. The stress-strain curves for all samples, including those that use different types of alkylsilanes, are characteristic of brittle materials (Figure 5.3a). The stress-strain relationship is linear until the strain is close to the material's fracture strain, at which point the material slightly yields and fractures.

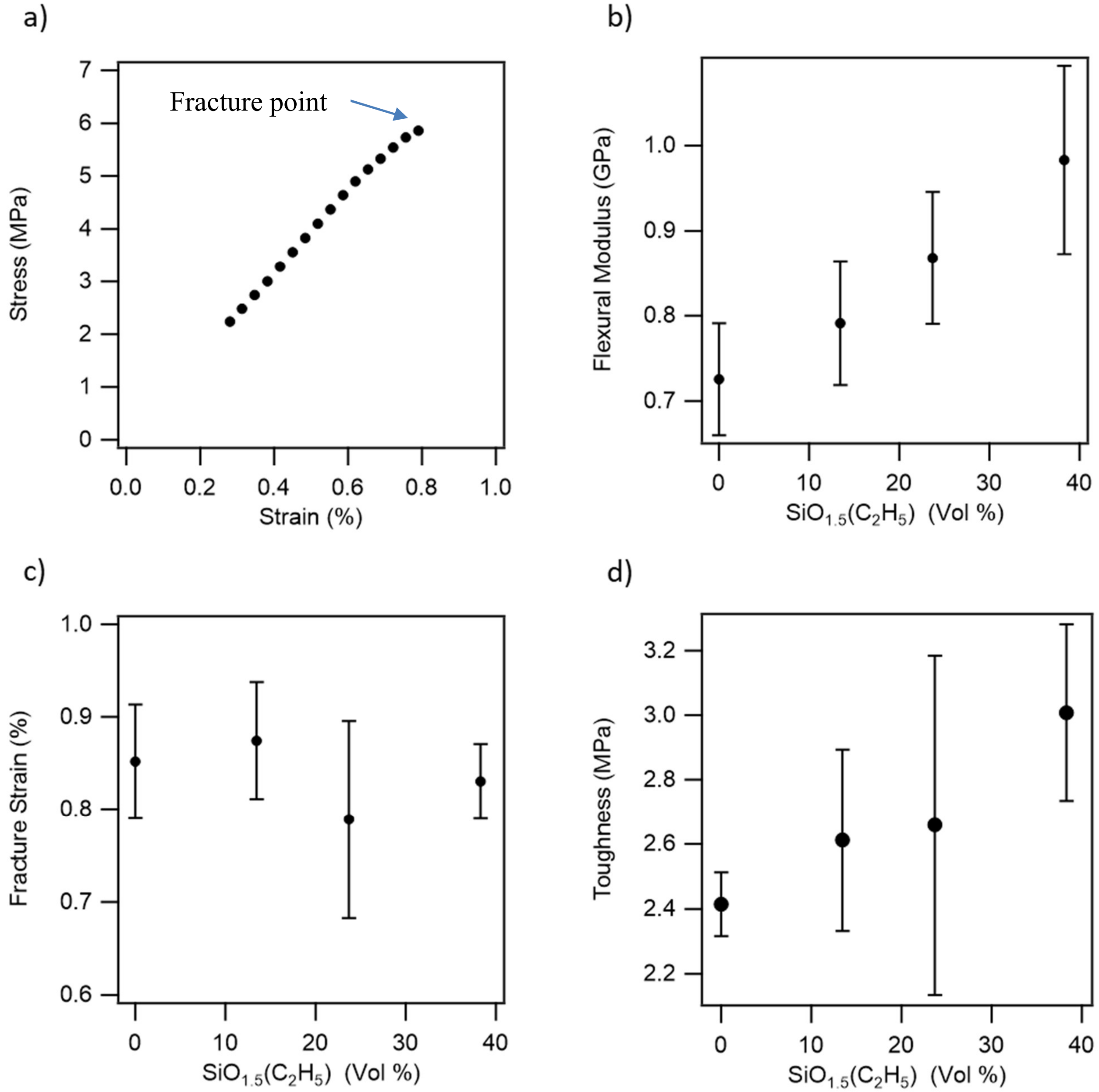

Figure 5.3: Typical stress strain curve of LUDOX-ATES ormosils. b) Flexural Modulus, c) fracture strain and, d) flexural strength as function of $SiO_{1.5}(C_2H_5)$ content. Error bars represent standard deviations for synthesis triplicates.

The mechanical properties of ormosils synthesized using various alkylsilanes were also investigated (Figure 5.4). ETES, BTES, and HTES were chosen to study the effect of the alkyl chain length, and DEDES was chosen to study the effect of having two nonhydrolyzable alkyl chain. For these samples, 500 μL of alkylsilane was added to the sol formulation. The mechanical properties of xerogels made from LUDOX only was also included for comparison.

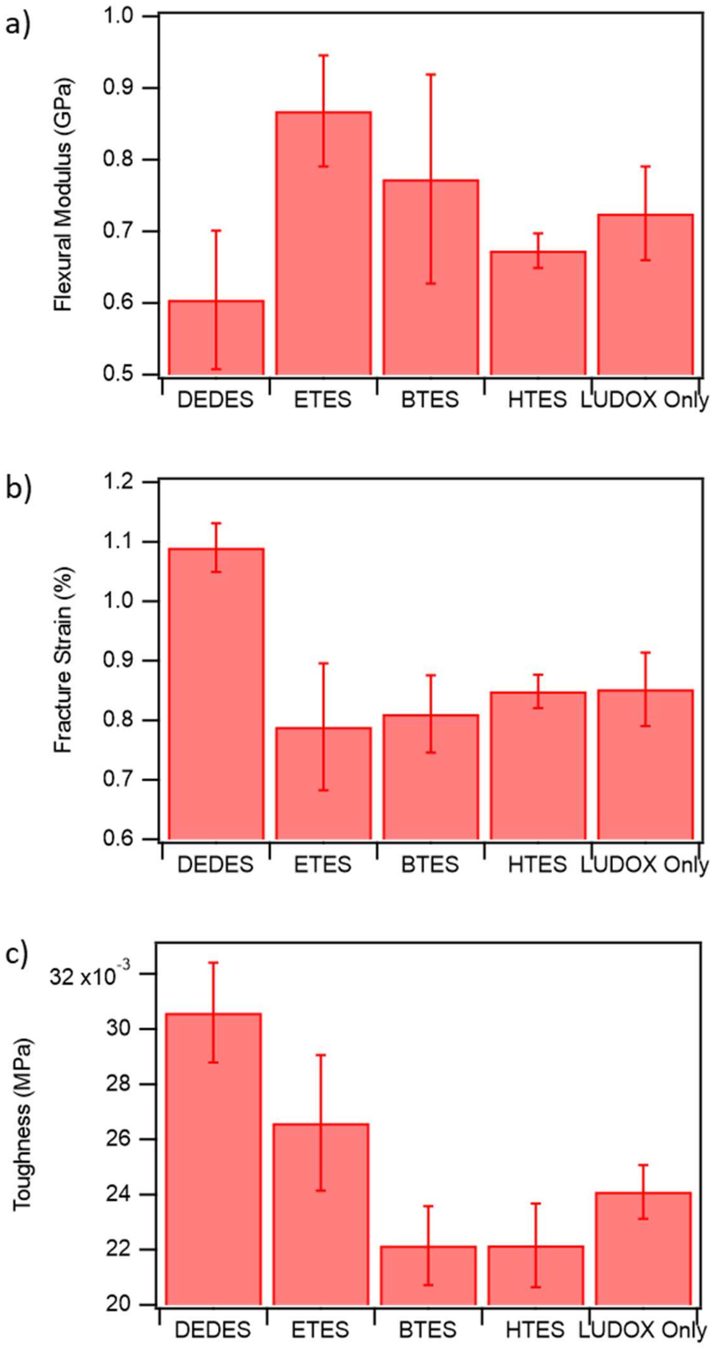

Figure 5.4: a) Flexural modulus, b) fracture strain, and c) toughness for ormosils with different alkylsilanes. Error bars represent standard deviations for synthesis triplicates.

SAXS experiments were performed to investigate the nanostructure of the ormosils. All SAXS profiles are slit-smeared. Figure 5.5 compares the SAXS profile of LUDOX particles as a 1 wt % dispersion and a xerogel. The dispersion data was fit with the sphere model, while the xerogel data was fit using the unified model implemented as part of Irena tool suite.[28,29] SAXS profiles for ormosils synthesized with varying amounts of ETES, keeping the pH at 2.1, are compared in Figure 5.6. SAXS profiles of ormosils with different types of alkylsilanes are compared in Figure 5.7. Comparison of SAXS profiles was performed by matching the scattering intensity at high-q, where the scattering is dominated by the surface of the LUDOX particles, and not on the 3-dimensional arrangement.

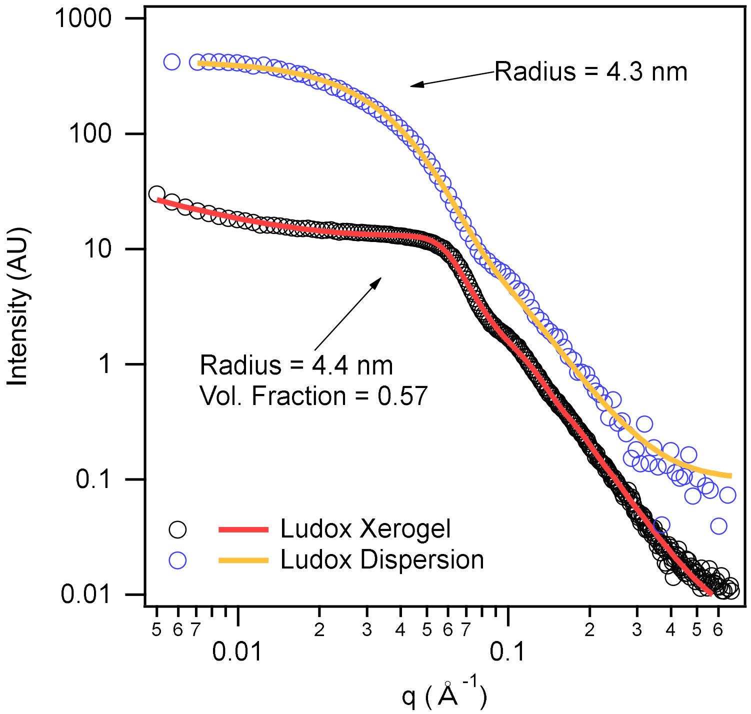

Figure 5.5: SAXS profile of LUDOX xerogel and diluted LUDOX dispersion, and their corresponding model fits.

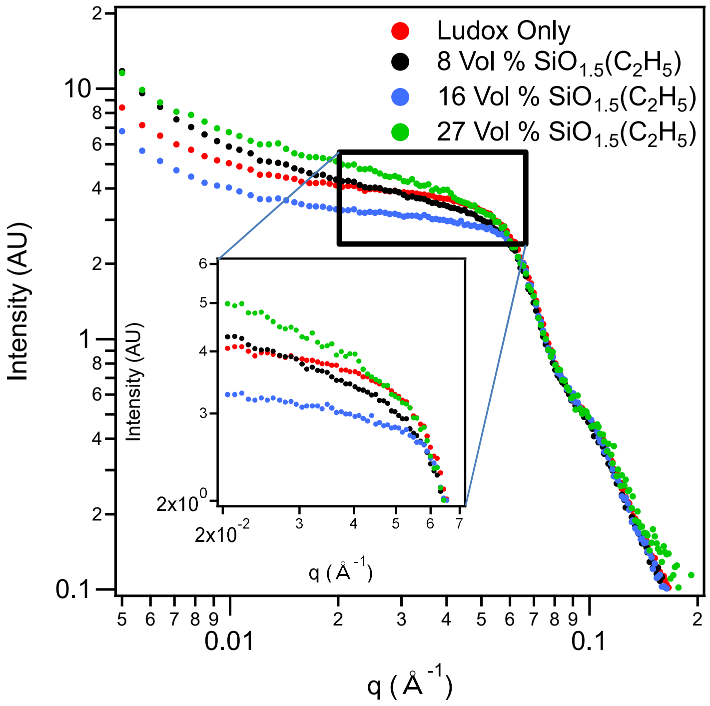

Figure 5.6: SAXS profiles of ormosils synthesized with varying amounts of ETES. Inset expands the boxed region of interest. The pH was kept constant at 2.1.

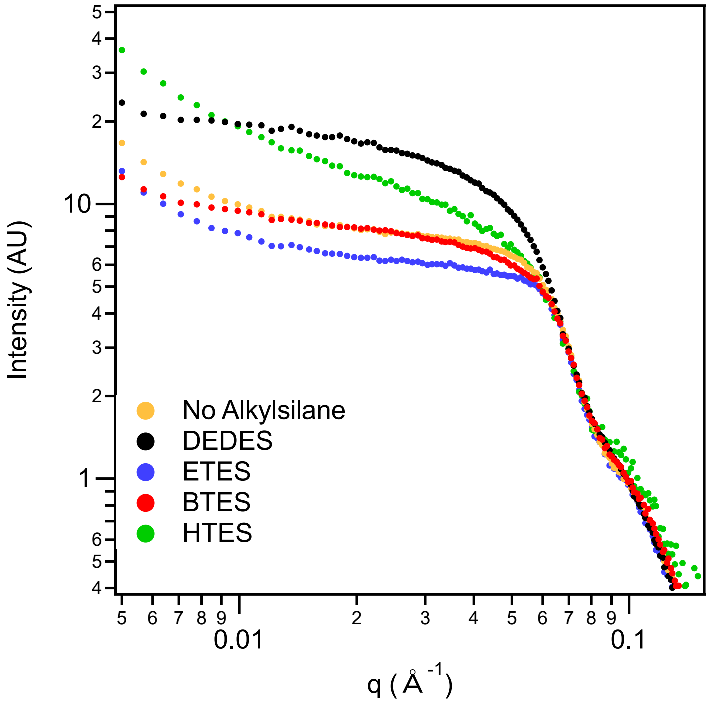

Figure 5.7: SAXS profiles of ormosils synthesized with different kinds of alkylsilanes. All samples were synthesized using 500 μL alkytriethoxysilane, at pH 2.1.

Figure 5.5 highlights some important features in forming xerogels from LUDOX particles. Scattering at the Porod region for both systems have a slope of -4, as expected for smooth silica particles. However, there is a significant difference from the low-q region to the mid-q region. The intensity for the xerogel is significantly depressed because of the close packing of LUDOX particles. Scattering intensity is proportional to the difference in scattering length density (SLD) between a particle and its surrounding, squared. For dilute systems, particles are surrounded by the medium. As particles are packed closer together, particles are surrounded by other particles, effectively reducing the SLD difference between a particle and its surrounding environment.

The increasing intensity towards low-q indicates that particles form fractal aggregates. Such multi-scale system can be fit and analyzed using the unified model. The unified model fits the Guinier part and the power law tail, level by level starting from the smallest scale. The Guinier region is located at the first knee for a particular level, and it reflects a generic size of the particle, regardless of its shape. The Porod region is located high-q and reflects the surface properties of the particles. For particles with smooth surfaces, the slope in the Porod region is -4. For rough surfaces, the slope is between -3 and -4. For mass fractals, the slope is between -1 and -3. In our system, the Guinier region and the power law tail is first fit for the LUDOX particles, and then for the fractals. Unfortunately, the limited resolution of the SAXS instrument (i.e. low-q limit), prevents full characterization of the fractals. Nevertheless, the model can include a correlation term or structure factor to account for the densely packed spheres. Fitting the model to the data, the radius of the particles was found to be 4.4 nm with a volume fraction of 0.57 in the solid ceramic material. The particle radius extracted from the unified model in the xerogel is in good agreement with that in dispersion (4.3 nm), even though the dispersion data was modeled using a different model, the spherical form factor. The volume fraction of 0.57 is consistent with random loose packing of uniform spheres,[30] as expected by particles with low sticking probability.

The effect of increasing ETES

The flexural modulus increases with increases amount of ETES used, while the fracture strain remains constant, which leads to higher toughness for larger amounts of ETES (Figure 5.3). The invariant fracture strain suggests that, for these samples, cracking is determined primarily by the gel network formed by the LUDOX particles. Palmisano et al. found the opposite trend in a TMOS and MTMS system, i.e. elastic modulus decreases with increasing organic content throughout the composition range.[23] However, the system presented in this work is not comparable to that in the work of Palmisano. In their system, the source of both organic and inorganic components are molecular precursors, and they are mixed at the molecular level. When using monomers as the organic content in a system where the inorganic content are also monomers, it is useful to think about this as substituting a TMOS molecule with a MTMS molecule. With each substitution, that molecule may have less binding with its neighbors, since MTMS only have 3 condensable groups, as opposed to 4 in TMOS. This leads to a less connected network and a lower modulus. The system presented in this work is different. Rather than having a co-condensation of organic and inorganic components, the inorganic components are silica particles that are large relative to the monomeric precursors. In a sense, the inorganic and organic components are phase separated into particles and the network formed by the monomers.

Our system is more similar to that in the work of Malzbender's,[17] where LUDOX particles are added into TEOS and MTMS mixture. That group found that the elastic modulus increases with increasing amounts of LUDOX particles, which is the opposite of our findings. However, the range of composition investigated by them is not the same as in our work. Malzbender investigated systems with a low fraction of particles, akin to dispersing inorganic particles in an organic matrix to strengthen it (Figure 5.8a). The strength of the composite is enhanced by the presence of the inorganic fillers according to the rule of mixtures for elastic modulus.[31] On the other hand, the system in this work is where the material is mostly composed of inorganic particles with small amounts of alkylsilane added as fillers to fill the gaps in between the particles (Figure 5.8c). In this case, the strength of the material is enhanced as alkylsilanes increase network connectivity between LUDOX particles and provide extra support in what would otherwise be empty space (Figure 5.8d), effectively increasing density and reducing porosity.

This conclusion is supported by the SAXS profiles of ormosils with increasing fraction of ethylsilanes (Figure 5.6). Ethylsilanes fill the gaps in between the LUDOX particles, which effectively reduces the SLD difference between the particles and their surroundings, which decreases the SAXS intensity at mid-q ($q = 0.04$ Å^{-1}). At 38 volume % of ethylsilane, there is an increase in intensity at mid-q. It has been shown that xerogels synthesized out of TEOS and MTMS have porosity over 60 %.[9,32] Since the calculated volumes taken by the ethylsilane network assumes dense packing, the calculated 38 volume % is a lower bound. Meanwhile, xerogel made with only LUDOX particles has a volume fraction of 0.57 (Figure 5.5). Thus, a likely explanation is that the amount of ethylsilane required to fill the gaps in between the LUDOX particles are exceeded, and excess ethysilane in the system dilutes the LUDOX particles, pushing them apart and effectively increasing the SLD difference (Figure 5.8b).

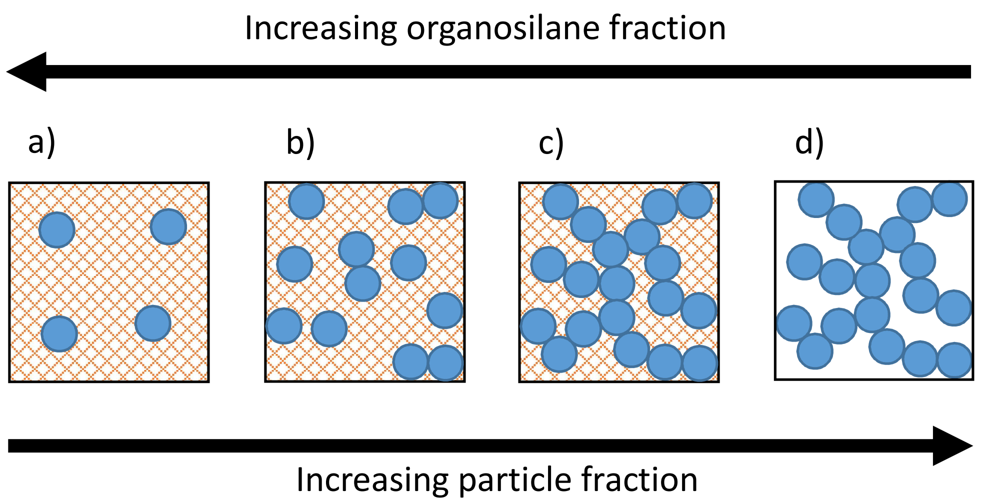

Figure 5.8: Structures of ormosils formed with different ratio of particles to monomers.

Effect of alkyl group

For ormosils synthesized using triethoxysilanes, increasing the alkyl chain length decreases flexural modulus, with no significant difference in fracture strain. Similar to ormosils synthesized with varying amounts of ETES, increasing flexural modulus is correlated with decreasing intensity of the SAXS profile at mid-q, indicating a tighter packing of LUDOX particles (Figure 5.7). The tighter packing of LUDOX particles can be reasoned the following way. Although the same volume of alkyltriethoxysilane was added into the sol mixture during the synthesis process, the calculated volume after complete hydrolysis and condensation is not the same (Table 5.1). All alkyltriethoxysilanes have comparable density, but there are large differences in molar mass. For a fixed volume of alkyltriethoxysilane, there are more molecules for compounds with a lower molar mass. Having more molecules means that there is more ethanol released during the hydrolysis reaction, and therefore less volume of remaining hydrolyzed silanes.

Table 5.1: Calculated volume fraction of alkylsilanes in synthesized ormosil assuming complete hydrolysis and condensation, when 500 µL of alkyltriethoxysilane is used in the sol formulation.

	Alkyltriethoxysilane Density (g/cm^3)	Alkyltriethoxysilane molar mass (g/mol)	Alkylsilane Amount (mol)	Alkylsilane Volume Fraction in Xerogel
ETES	0.896	192.33	0.00233	0.24
BTES	0.888	220.38	0.00202	0.29
HTES	0.860	248.44	0.00173	0.33
DEDES	0.862	176.33	0.00245	0.34

A similar argument can be made for DEDES. Although it has the largest molar amount per 500 µL of alkyltriethoxysilane, there are only two ethoxy groups to be hydrolyzed, and therefore less volume is subtracted by the leaving ethanol molecules. Of course, the calculated volume fraction of alkylsilane is a lower bound that does not take into account the packing efficiency of the alkylsilanes in forming the network. One would expect bifunctional silanes such as DEDES to pack less efficiently than trifunctional silanes because of extra unreactive ethyl group, and the scenario in Figure 5.8b is approached, where the LUDOX particles are less densely packed. The looser packing of LUDOX particles clearly be seen its SAXS profile (Figure 5.7), where the intensity at mid-q increases significantly. Furthermore, one would also expect the degree of crosslinking to be less for DEDES than for trifunctional silanes because it only has two condensable groups and it may form linear polymers. Both reasons combined may explain the lower strength of xerogels synthesized with DEDES, but also the higher elasticity.

Interestingly only xerogels synthesized with ETES had enhanced modulus over xerogels synthesized with only LUDOX particles. BTES and HTES had a negligible and negative effect, respectively. The most likely reason is that butyl- and hexyl- silanes are unable to form a network because of the bulky alkyl group. Loy et al. studied the gelation of various trialkoxysilanes, and they found that while ethylsilanes can form gels, butyl- and hexyl- silanes do not.[33] Instead they form an oil or resinous phase, which are presumably Polyhedral Oligomeric Silsesquioxane (POSS) particles. Silanes may also bind to the surface of LUDOX particles and create a thin hairy layer. In the case of hexylsilanes, the length of the alkyl chain may provide sufficient steric hindrance against condensation, viz. preventing adhesion between LUDOX particles, leading to the decrease in modulus.

Yet a more meaningful metric is toughness. Toughness is the area under the stress-strain curve and is a measure of how much energy the material can absorb before cracking. Although ormosils synthesized with DEDES results in the lowest flexural modulus, the brittleness of the material is greatly reduced, as shown by the significant increase in fracture strain (Figure 5.4b). The overall effect is that ormosils synthesized with DEDES have the highest toughness, and it can be reasoned in the following way. First, as previously discussed, out of all the alkylsilanes used, DEDES occupies the most volume when dried, pushing the LUDOX particles apart from each other. This gives room for the LUDOX particles to flex and move under strain without disrupting the gel network. Second, each DEDES molecule can either condense with another DEDES molecule or a surface of a LUDOX particle. With only two hydrolysable groups, and DEDES cannot form a cross-linked network. In this case, DEDES molecules polymerize to form polydiethylsiloxanes (PDES), an analog to the more commonly known rubbery material, polydimethylsiloxane (PDMS). These PDES chains act as binders to keep the LUDOX particles from collapsing and also as molecular springs between LUDOX particles.

5.4 CONCLUSION

Hybrid organic/inorganic xerogels were synthesized using LUDOX particles and various alkylsilanes. All xerogels were synthesized with low organic content. Two sets of experiments were performed. In the first set of experiments, ormosils were synthesized using various amounts of ETES. Increasing amounts of ETES in the recipe leads to larger flexural modulus and no effect on fracture strain, and thus leads to larger toughness as well. These ethylsilanes form a network that fill the gap in between LUDOX particles, and therefore reinforce the structure that would otherwise be empty space. The fact that these ethylsilanes do not affect the fracture strain suggests that fracture is primarily determined by a break in the LUDOX gel network. The second set of experiments investigated the effect of different kinds of alkylsilanes. No mechanical enhancement was observed when BTES or HTES was used instead of ETES. Unlike ethylsilanes, butylsilanes and hexylsilanes cannot form an interconnected network, and instead prevents adhesions between LUDOX particles. Using DEDES results in ormosils with a lower modulus and much higher fracture strain than any other ormosils, including those synthesized without any alkylsilane additives, resulting in significant increase in toughness. DEDES condense together to form PDES that act as molecular springs between LUDOX particles. Thus at low organic content, rather than small alkylsilane molecules, polymers or alkylsilanes that can form polymers are better candidates towards crack resistant ceramics.

5.5 REFERENCES

(1) Brinker, C. J.; Scherer, G. W. *Sol-gel science : the physics and chemistry of sol-gel processing*, 1st ed.; Academic Press: San Diego, 1990.

(2) Iler, R. K. *The Chemistry of Silica*; John Wiley & Sons: New York, 1979.

(3) Brinker, C. J.; Sehgal, R.; Hietala, S. L.; Deshpande, R.; Smith, D. M.; Loy, D.; Ashley,

C. S. *J. Memb. Sci.* **1994**, *94* (1), 85–102.

(4) Brinker, C. J. *J. Non. Cryst. Solids* **1988**, *100*, 31–50.

(5) Mammeri, F.; Le Bourhis, E.; Rozes, L.; Sanchez, C. *J. Mater. Chem.* **2005**, *15* (35–36), 3787–3811.

(6) Mackenzie, J. D. *J. Sol-Gel Sci. Technol.* **1993**, *1* (1), 7–19.

(7) Sanchez, C.; Ribot, F.; Lebeau, B. *J. Mater. Chem.* **1999**, *9*, 35–44.

(8) Priyadharshini, A.; Kalainathan, S.; Boury, B.; Corriu, R. J. P. *Pure Appl. Opt.* **1996**, *5*, 689–699.

(9) Budunoglu, H.; Yildirim, A.; Bayindir, M. *J. Mater. Chem.* **2012**, *22* (19), 9671–9677.

(10) Zhang, Q.; Chan, H. L. W.; Zhou, Q.; Choy, C. L. *Chinese Sci. Bull.* **1998**, *43* (2), 111–114.

(11) Chen, Y.; Chan, H. L. W.; Choy, C. L. *Thin Solid Films* **1998**, *323*, 270–274.

(12) Chan, H. L. W.; Lau, S. T.; Kwok, K. W.; Zhang, Q. Q.; Zhou, Q. F.; Choy, C. L. *Sensors Actuators, A Phys.* **1999**, *75* (3), 252–256.

(13) Harmer, M. A.; Farneth, W. E.; Sun, Q. *J. Am. Chem. Soc.* **1996**, *118* (33), 7708–7715.

(14) Honma, I.; Hirakawa, S.; Yamada, K.; Bae, J. M. *Solid State Ionics* **1999**, *118*, 29–36.

(15) Hu, Q.; Marand, E.; Dhingra, S.; Fritsch, D.; Wen, J.; Wilkes, G. *J. Memb. Sci.* **1997**, *135*, 65–79.

(16) Nunes, S. P.; Schultz, J.; -V., P. K. *J. Mater. Sci. Lett.* **1996**, *15* (13), 1139–1141.

(17) Malzbender, J.; den Toonder, J. M. J.; Balkenende, A. R.; de With, G. *Mater. Sci. Eng. R Reports* **2002**, *36* (2–3), 47–103.

(18) Mackenzie, J. D.; Huang, Q.; Iwamoto, T. *J. Sol-Gel Sci. Technol.* **1996**, *7* (3), 151–161.

(19) Haas, K. H.; Wolter, H. *Curr. Opin. Solid State Mater. Sci.* **1999**, *4* (6), 571–580.

(20) Hu, Y.; Mackenzie, J. D. *J. Mater. Sci.* **1992**, *27* (16), 4415–4420.

(21) Coltrain, B. K.; Landry, C. J. T.; O'Reilly, J. M.; Chamberlain, A. M.; Rakes, G. A.; Sedita, J. S.; Kelts, L. W.; Landry, M. R.; Long, V. K. *Chem. Mater.* **1993**, *5* (10), 1445–1455.

(22) Etienne, P.; Phalippou, J.; Sempere, R. *J. Mater. Sci.* **1998**, *33* (15), 3999–4005.

(23) Palmisano, G.; Le Bourhis, E.; Ciriminna, R.; Tranchida, D.; Pagliaro, M. *Langmuir* **2006**,

22 (26), 11158–11162.

(24) Coltrain, B. K.; Melpolder, S. M.; Salva, J. M. In *Ultrastructure Processing of Advanced Materials*; Uhlmann, D. R., Ulrich, D. R., Eds.; John Wiley & Sons: New York, 1992; pp 69–76.

(25) Daniels, M. W.; Sefcik, J.; Francis, L. F.; McCormick, A. V. *J. Colloid Interface Sci.* **1999**, *219* (2), 351–356.

(26) Nishiyama, N.; Horie, K.; Asakura, T. *J. Colloid Interface Sci.* **1989**, *129* (1), 113–119.

(27) Nishiyama, N.; Asakura, T.; Horie, K. *J. Colloid Interface Sci.* **1988**, *124* (1), 14–21.

(28) Ilavsky, J.; Jemian, P. R. *J. Appl. Crystallogr.* **2009**, *42* (2), 347–353.

(29) Beaucage, G. *J. Appl. Crystallogr.* **1995**, *28*, 717–728.

(30) Onoda, G. Y.; Liniger, E. G. *Phys. Rev. Lett.* **1990**, *64* (22), 2727–2730.

(31) Callister Jr., W. D.; Rethwisch, D. G. *Materials Science and Engineering An Introduction*, 8th ed.; John Wiley & Sons: New York, 2010.

(32) Yu, S.; Wong, T. K. S.; Hu, X.; Pita, K. *J. Electrochem. Soc.* **2003**, *150* (5), F116.

(33) Loy, D. A.; Baugher, B. M.; Baugher, C. R.; Schneider, D. A.; Rahimian, K. *Chem. Mater.* **2000**, *12* (12), 3624–3632.

Chapter 6. SUMMARY AND OUTLOOK

6.1 SONOCHEMICAL SYNTHESIS OF NANOMATERIALS

The traditional methods of synthesizing nanoparticles from molecular precursors, the hot-injection and heat-up method, have numerous problems that results in poor scalability and reproducibility.[1] A relatively new method to synthesize nanomaterials is through sonochemistry, viz. using ultrasound. Application of ultrasound to liquid leads to violent cavitation causing extreme local temperatures and pressures. These extreme conditions can be used to decompose metalloorganic precursors to produce nanoparticles.[2]

Although nanoparticles with various size, shape, and compositions have been successfully synthesized using ultrasound, the focus has been mostly placed on the final product itself, and the process is often not sufficiently understood and, thus, poorly controlled.[3] In chapter 3, a novel sonochemical synthesis method is presented, where sonication is performed in an emulsion system rather than in a single-phase bulk system. Sonication in a single-phase system was also performed for comparison. The reactions used cadmium oleate and trioctylphosphine selenium precursors to synthesize CdSe quantum dots (QD), and the reaction progress is tracked as a function of sonication time under controlled temperature conditions to isolate the effect of cavitation from that of bulk temperature changes. Conversion from precursors to QD is slow in a single-phase bulk liquid system (octadecene), but it is greatly accelerated in the dispersed system (octadecene in ethylene glycol emulsion). The presence of a liquid-liquid interface allows the preferred heterogenous nucleation of bubbles,[4] resulting in more frequent cavitations to drive the conversion from precursors to QDs. The capacity of CdSe production using ultrasound in the emulsion system and the single-phase system are 3.8 g/L hr and 0.54 g/L hr, respectively. In the emulsion system, the rate of CdSe production is comparable to the typical hot-injection synthesis of CdSe QDs and can likely be further optimized. The difference in the rate of QD production leads to different products between the two systems. Sonication in the emulsion system leads to CdSe magic-size clusters (MSC), QDs with an exact number of atoms; in this case, $(CdSe)_{33}$ and $(CdSe)_{34}$ are synthesized. These MSCs form large aggregates with low fractal dimension, resembling a fiber, which protect the MSCs from growth and dissolution.[5] In the single-phase system, initially MSCs are also formed. However, because the production rate of MSCs is low, the concentration is low such that they do not form aggregates. With no protection, these MSCs quickly dissolve or grow into ultrasmall QDs. Finally, precise temporal control of QD production is demonstrated by turning the ultrasound on and off; QDs are produced when there is ultrasound, and not produced when there is not.

While this work successfully demonstrated the sonochemical synthesis of CdSe in the emulsion system, many things are yet to be investigated. From a fundamental perspective, there are still missing puzzle pieces. For example, the literature addresses the mechanism of CdSe synthesis using the hot-injection or heat-up method extensively.[1,6–9] It was assumed that similar reaction mechanisms occur for synthesis using ultrasound. For example, in the hot-injection method, the use of tertiary phosphine-chalcogenide involves the decomposition of the precursors to form reactive H_2Se intermediates.[6] Given the extreme temperatures and pressures of cavitation of 5000 K and 1000 bar,[2,3] respectively, it seems reasonable to assume that a cavitation event is sufficient to decompose the precursors, and the same reaction route is taken; however, we have not proven this.

A study to further optimize the system is also warranted. It was shown that sonochemical synthesis in the emulsion system is much faster than that in the single-phase bulk system, and at a CdSe production rate of 3.8 g/L hr excluding ligands, it is comparable to a typical hot-injection synthesis. The volumetric yield of QDs can be optimized by performing experiments in which the volume ratio between the octadecene and ethylene glycol is varied. At one extreme, where the volume is entirely composed of the oil phase, it was shown that the synthesis of QD is slow. Of course, at the other extreme where the volume is entirely ethylene glycol, no QD would be produced at all. Hence, somewhere in between, there is likely an optimum ratio between octadecene and ethylene glycol such that the amount of precursor and interface combined is optimized.

Recently, Flamee et al. was able to produce up to 50 g/L hr of CdSe using the hot-injection method,[10] assuming total synthesis time of 1 hour including the initial heating and final cooling of the reaction mixture. They were able to do this by using a much more concentrated precursor mixture, with Cd precursor solution of up 1 M, as opposed to 0.063 M in the work performed in chapter 3. The caveat is that their experiments were performed in 10 mL batches, and scaling the reaction to larger volumes would entail all the problems associated with scaling of the hot-injection method. It would thus be interesting to use such highly concentrated precursor mixtures with ultrasound in an emulsion system. However, using the most concentrated precursor solution may not necessarily lead to fastest production rate. Increasing precursor concentration to 1 M canresults in a 5-fold increase in viscosity,[11] and higher viscosity discourages cavitation[4,12].

Another missing piece is with regards to the QDs themselves. Are QDs produced sonochemically in an emulsion system equivalent to those produced by the hot-injection method? Fast and intense, non-equlibrium methods such as laser ablation are known to result in defects.[13,14] Thus, it seems reasonable to think that cavitation would do similar things. Crystal structure characterization of small QDs, especially MSCs, are challenging because their x-ray diffraction (XRD) spectra exhibit broad peaks that may overlap with each other. It wasn't until recently that some light was shed on these structures, which required a combination of characterization methods.[15,16] But then again, a defect is considered a defect when it is an irregularity in an otherwise continuous lattice. What is a defect when the entire structure is essentially a defect "composed of entirely of a discontinuous arrangement of atoms that are all in constant chemical contact with the capping material, solvent, and contaminants"?[17]

Finally, CdSe was used as a model system to study sonochemical synthesis in an emulsion system. One of the next steps would be to synthesize other types of QDs as well. In particular indium phosphide (InP) has gained much interest because they can be applied in similar ways, but is much less toxic than CdSe. Also, while CdSe is a II-VI semiconductor, InP is a III-V semiconductor. Therefore, synthesizing InP would serve well to demonstrate the versatility of this new method.

6.2 SELF-ASSEMBLY OF NANOPARTICLES

Once the nanoparticles are synthesized, chapter 4 discusses how they can be assembled together to elicit new properties and/or create functional materials. Specifically, bottom-up approaches to the synthesis of nanostructures are of particular interest because they offer several advantages over the traditional top-down approaches. A new method was described to self-assemble nanoparticles into controlled heteroaggregates. The technique relies on carefully balancing attractive electrostatic forces with repulsive steric hindrance that is provided by surface-grafted polyethylene glycol (PEG). Two different-sized gold nanoparticles (GNP) were used as a model system; 13 nm GNPs were functionalized with PEG-thiol and a positively charged thiol, while 7 nm GNPs were functionalized with PEG-thiol and a negatively charged thiol. When mixed together, these oppositely charged particles self-assemble into stable colloidal structures (i.e.

nanoclusters) whose structure depends strongly on the surface concentration of PEG. Smaller structures are obtained as the PEG surface concentration increases because steric hindrance dominates and prevents uncontrolled aggregation. In particular, under the right conditions, it was possible to selectively synthesize heterodimers (which are effectively Janus particles) and linear heteroassemblies. Thus far, methods to synthesize heteroassemblies are energy intensive, sensitive to the heating procedure, and are mostly material combination specific.[18–20] On the other hand, the method presented in chapter 4 is simple, and it is a generalized method to synthesize heteroassemblies out of any material.

Gold nanoparticles were selected as the model systems because their properties are well characterized and this facilitated the core objective of the project: to develop a scalable method to assemble two different types of particles into controlled heteroaggregates. The natural extension of this work would be to use other types of particles to create functional materials. It is important that the head groups of the ligands may need to be different depending on the material. Love et al. compiled a list of substrates and their compatible head groups to create self-assembled monolayers.[21] For example, if a substrate is iron oxide, then a molecule with an alcohol group would serve well to bind to the surface of iron oxide.

One interesting application would be to attach a catalytically active material like palladium to a magnetic material like iron oxide to create magnetically recyclable catalysts. Jang et al. have exactly done this; they synthesized Pd-Fe_3O_4 heterodimers to catalyze for Suzuki cross-coupling reactions.[22] They showed that the palladium is catalytically active even though they are covered with oleylamine and oleic acid ligands. A lingering question, however, is if the surface of the palladium would still be as catalytically active when it covered with a thick layer of polymer such as PEG. Dynamic light scattering (DLS) showed that 10 kDa polyethylene glycol results in an adlayer of about 10 nm. Perhaps it would be necessary to use lower molecular weight polymers. If the surface is still not catalytically active, then perhaps ligand removal and/or exchange may be necessary, and there are simple ways to do that.[23]

6.3 IMPROVING THE MECHANICAL PROPERTIES OF CERAMICS

The work in chapter 5 was performed in collaboration with Membrion, a startup with a mission to create ceramic based ion exchange membranes for any application in harsh environments. While ceramics offer good chemical and thermal stability, their brittle nature makes transportation and handling challenging. Literature has shown that adding organic additives to ceramics can improve their mechanical properties.[24,25] Towards that goal, a study was performed on the mechanical properties of ormosils synthesized out of LUDOX particles and various alkylsilanes.

Specifically, ormosils were synthesized with low alkylsilane loading. In this system, the material is still mostly composed of LUDOX particles, and alkylsilanes act as fillers in between LUDOX particles. Fracture behavior is still determined by a break in the LUDOX gel network. When triethoxysilanes with short alkyl chain, ethyltriethoxysilane (ETES), was used as the additive, these silanes form a network in between the LUDOX particles, enhancing the flexural modulus without sacrificing fracture strain, viz. flexibility. Up to a volume fraction of 38 %, the ormosils had higher flexural modulus and toughness with increasing ETES content. Such enhancement was not observed when triethoxysilanes of longer alkyl chain, butyltriethoxysilane (BTES) and hexyltriethoxysilane (HTES), because steric hindrance from the longer alkyl chains prevent efficient packing of these molecules. Using diethyldiethoxysilane (DEDES), a lowering of modulus, but a significant increase in fracture strain was observed, resulting in the highest toughness out of all the alkylsilane additives. This is because DEDES cannot crosslink, and instead they polymerize to form polydiethylsiloxane (PDES), which acts as springs between the LUDOX particles. Thus to prevent cracks, polymers or alkylsilanes that can form polymers are better candidates.

It should be noted that the original purpose of these ceramics is to be used as ion exchange membranes in flow batteries. While the work presented in chapter 5 uses organosilane additives, the organic components are simply alkyl groups and are not functional. In fact, Alkyl groups are hydrophobic and prevent efficient transport of ions through the pores. Preliminary iron chloride permeability, which is one of the redox species candidates, for ormosils synthesized with alkylsilanes was very low. Unfortunately, the hydrophobic nature of the additives also almost entirely blocked the passage of protons, which rendered the membranes useless for the intended application. Future work should focus on using organosilanes with strongly acidic functional groups, such as sulfonic acid, and/or with hydrophilic substituents, such as polyethers, so that the organic component would not only improve the mechanical properties of the ceramics, but also improve the membrane's ionic conduction performance.

6.4 REFERENCES

(1) Van Embden, J.; Chesman, A. S. R.; Jasieniak, J. J. *Chem. Mater.* **2015**, *27* (7), 2246–2285.

(2) Suslick, K. S. *Science* **1990**, *247*, 1439–1445.

(3) Bang, J. H.; Suslick, K. S. *Adv. Mater.* **2010**, *22* (10), 1039–1059.

(4) Brennen, C. E. *Cavitation and Bubble Dynamics*, 1st ed.; Cambridge University Press: Cambridge, 2013.

(5) Nevers, D. R.; Williamson, C. B.; Savitzky, B. H.; Hadar, I.; Banin, U.; Kourkoutis, L. F.;

Hanrath, T.; Robinson, R. D. *J. Am. Chem. Soc.* **2018**, *140* (10), 3652–3662.

(6) Frenette, L. C.; Krauss, T. D. *Nat. Commun.* **2017**, *8* (1), 1–8.

(7) Ruberu, T. P. A.; Albright, H. R.; Callis, B.; Ward, B.; Cisneros, J.; Fan, H. J.; Vela, J. *ACS Nano* **2012**, *6* (6), 5348–5359.

(8) Evans, C. M.; Evans, M. E.; Krauss, T. D. *J. Am. Chem. Soc.* **2010**, *132* (32), 10973–10975.

(9) Cossairt, B. M.; Owen, J. S. *Chem. Mater.* **2011**, *23* (12), 3114–3119.

(10) Flamee, S.; Cirillo, M.; Abe, S.; De Nolf, K.; Gomes, R.; Aubert, T.; Hens, Z. *Chem. Mater.* **2013**, *25* (12), 2476–2483.

(11) Williamson, C. B.; Nevers, D. R.; Hanrath, T.; Robinson, R. D. *J. Am. Chem. Soc.* **2015**, *137* (50), 15843–15851.

(12) Vijaya Kumar, R.; Diamant, Y.; Gedanken, A. *Chem. Mater.* **2000**, *12* (8), 2301–2305.

(13) Usui, H.; Shimizu, Y.; Sasaki, T.; Koshizaki, N. **2005**, 120–124.

(14) Zeng, B. H.; Duan, G.; Li, Y.; Yang, S.; Xu, X. **2010**, 561–572.

(15) Williamson, C. B.; Nevers, D. R.; Nelson, A.; Hadar, I.; Banin, U.; Hanrath, T.; Robinson, R. D. *Science* **2019**, *363* (6428), 731–735.

(16) Beecher, A. N.; Yang, X.; Palmer, J. H.; Lagrassa, A. L.; Juhas, P.; Billinge, S. J. L.; Owen, J. S. *J. Am. Chem. Soc.* **2014**, *136* (30), 10645–10653.

(17) Landes, C. F.; Braun, M.; El-Sayed, M. A. *J. Phys. Chem. B* **2001**, *105* (43), 10554–10558.

(18) Wang, C.; Xu, C.; Zeng, H.; Sun, S. *Adv. Mater.* **2009**, *21* (30), 3045–3052.

(19) Casavola, M.; Buonsanti, R.; Caputo, G.; Cozzoli, P. D. *Eur. J. Inorg. Chem.* **2008**, No. 6, 837–854.

(20) Sun, S.; Yu, H.; Wang, S. X. Dumbbell-like nanoparticles and a process of forming the same. US 2006/0053971 A1, 2006.

(21) Love, J. C.; Estroff, L. A.; Kriebel, J. K.; Nuzzo, R. G.; Whitesides, G. M. *Chem. Rev.* **2005**, *105* (4), 1103–1170.

(22) Jang, Y.; Chung, J.; Kim, S.; Jun, S. W.; Kim, B. H.; Lee, D. W.; Kim, B. M.; Hyeon, T. *Phys. Chem. Chem. Phys.* **2011**, *13* (7), 2512–2516.

(23) Elliott, E. W.; Glover, R. D.; Hutchison, J. E. *ACS Nano* **2015**, *9* (3), 3050–3059.

(24) Mammeri, F.; Le Bourhis, E.; Rozes, L.; Sanchez, C. *J. Mater. Chem.* **2005**, *15* (35–36), 3787–3811.

(25) Malzbender, J.; den Toonder, J. M. J.; Balkenende, A. R.; de With, G. *Mater. Sci. Eng. R Reports* **2002**, *36* (2–3), 47–103.

BIBLIOGRAPHY

Abe, S., Čapek, R. K., De Geyter, B., & Hens, Z. (2012). Tuning the postfocused size of colloidal nanocrystals by the reaction rate: From theory to application. ACS Nano, 6(1), 42–53. https://doi.org/10.1021/nn204008q

Abu-Reziq, R., Wang, D., Post, M., & Alper, H. (2007). Platinum nanoparticles supported on ionic liquid-modified magnetic nanoparticles: selective hydrogenation catalysts. Adv. Synth. Catal., 349(13), 2145–2150. https://doi.org/10.1002/adsc.200700129

Bain, C. D., Evall, J., & Whitesides, G. M. (1989). Formation of monolayers by the coadsorption of thiols on gold: variation in the head group, tail group, and solvent. Journal Of The American Chemical Society, 111(18), 7155–7164. https://doi.org/10.1021/ja00200a039

Bang, J. H., & Suslick, K. S. (2010). Applications of ultrasound to the synthesis of nanostructured materials. Advanced Materials, 22(10), 1039–1059. https://doi.org/10.1002/adma.200904093

Bao, J., Chen, W., Liu, T., Zhu, Y., Jin, P., Wang, L., … Li, Y. (2007). Bifunctional Au-Fe 3 O 4 Nanoparticles for Protein Separation. ACS Nano, 1(4), 293–298. https://doi.org/10.1021/nn700189h

Barthlott, W., & Neinhuis, C. (1997). Purity of the sacred lotus, or escape from contamination in biological surfaces. Planta, 202(1), 1–8. https://doi.org/10.1007/s004250050096

Bawendi, M. G., Steigerwald, M. L., & Brus, Louis, E. (1990). The Quantum Mechanics of Larger Semiconductor Clusters (“Quantum Dots”). Annual Review of Physical Chemistry, 41(1), 477–496.

Beaucage, G. (1995). Approximations Leading to a Unified Exponential/Power-Law Approach to Small-Angle Scattering. Journal of Applied Crystallography, 28, 717–728. Retrieved from http://www.eng.uc.edu/~beaucag/PDFPapers/Beaucage2.pdf

Beecher, A. N., Yang, X., Palmer, J. H., Lagrassa, A. L., Juhas, P., Billinge, S. J. L., & Owen, J. S. (2014). Atomic structures and gram scale synthesis of three tetrahedral quantum dots. Journal of the American Chemical Society, 136(30), 10645–10653. https://doi.org/10.1021/ja503590h

Berg, J. C. (2014). An Introduction to Interafaces & Colloids. Singapore: World Scientific.

Bowers, M. J., McBride, J. R., & Rosenthal, S. J. (2005). White-light emission from magic-sized cadmium selenide nanocrystals. Journal of the American Chemical Society, 127(44), 15378–15379. https://doi.org/10.1021/ja055470d

Brennen, C. E. (2013). Cavitation and Bubble Dynamics (1st ed.). Cambridge: Cambridge University Press. https://doi.org/10.1017/CBO9781107338760

Brinker, C. J. (1988). Hydrolysis and Condensation of Silicates: Effects on Structure. Journal of Non-Crystalline Solids, 100, 31–50.

Brinker, C. J., Sehgal, R., Hietala, S. L., Deshpande, R., Smith, D. M., Loy, D., & Ashley, C. S. (1994). Sol-gel strategies for controlled porosity inorganic materials. Journal of Membrane Science, 94(1), 85–102. https://doi.org/10.1016/0376-7388(93)E0129-8

Brinker, C. Jeffrey, & Scherer, G. W. (1990). Sol-gel science : the physics and chemistry of sol-gel processing (1st ed.). San Diego: Academic Press. https://doi.org/10.1016/S0254-0584(02)00315-2

Brown, L. V., Sobhani, H., Lassiter, J. B., Nordlander, P., & Halas, N. J. (2010). Heterodimers: Plasmonic properties of mismatched nanoparticle pairs. ACS Nano, 4(2), 819–832. https://doi.org/10.1021/nn9017312

Budunoglu, H., Yildirim, A., & Bayindir, M. (2012). Flexible and mechanically stable antireflective coatings from nanoporous organically modified silica colloids. Journal of Materials Chemistry, 22(19), 9671–9677. https://doi.org/10.1039/c2jm30804e

Callister Jr., W. D., & Rethwisch, D. G. (2010). Materials Science and Engineering An Introduction (8th ed.). New York: John Wiley & Sons.

Carbone, L., & Cozzoli, P. D. (2010). Colloidal heterostructured nanocrystals: Synthesis and growth mechanisms. Nano Today, 5(5), 449–493. https://doi.org/10.1016/j.nantod.2010.08.006

Casavola, M., Buonsanti, R., Caputo, G., & Cozzoli, P. D. (2008). Colloidal strategies for preparing oxide-based hybrid nanocrystals. European Journal of Inorganic Chemistry, (6), 837–854. https://doi.org/10.1002/ejic.200701047

Chan, H. L. W., Lau, S. T., Kwok, K. W., Zhang, Q. Q., Zhou, Q. F., & Choy, C. L. (1999). Nanocomposite ultrasonic hydrophones. Sensors and Actuators, A: Physical, 75(3), 252–256. https://doi.org/10.1016/S0924-4247(99)00076-X

Chen, Y., Chan, H. L. W., & Choy, C. L. (1998). Pyroelectric properties of PbTiO3/P(VDF-TrFE) 0 – 3 nanocomposite films. Thin Solid Films, 323, 270–274.

Chung, C., & Lee, M. (1999). Exchange of self-assembled thiol monolayers on gold: characterization by FT-IR external reflection spectroscopy. Journal of Electroanalytical Chemistry, 468(1), 91–97. https://doi.org/10.1016/S0022-0728(99)00072-8

Collard, D. M., & Fox, M. A. (1991). Use of electroactive thiols to study the formation and exchange of alkanethiol monolayers on gold. Langmuir, 7(13), 1192–1197. https://doi.org/10.1021/la00054a029

Coltrain, B. K., Landry, C. J. T., O'Reilly, J. M., Chamberlain, A. M., Rakes, G. A., Sedita, J. S., … Long, V. K. (1993). Role of Trialkoxysilane Functionalization in the Preparation of Organic-Inorganic Composites. Chemistry of Materials, 5(10), 1445–1455. https://doi.org/10.1021/cm00034a014

Coltrain, B. K., Melpolder, S. M., & Salva, J. M. (1992). Effect of hydrogen ion concentration on gelation of tetrafunctional silicate sol-gel systems. In D. R. Uhlmann & D. R. Ulrich (Eds.), Ultrastructure Processing of Advanced Materials (pp. 69–76). New York: John Wiley & Sons.

Cossairt, B. M., & Owen, J. S. (2011). CdSe clusters: At the interface of small molecules and quantum dots. Chemistry of Materials, 23(12), 3114–3119. https://doi.org/10.1021/cm2008686

Daniels, M. W., Sefcik, J., Francis, L. F., & McCormick, A. V. (1999). Reactions of a trifunctional silane coupling agent in the presence of colloidal silica sols in polar media. Journal of Colloid and Interface Science, 219(2), 351–356. https://doi.org/10.1006/jcis.1999.6497

De La Iglesia, P., Jaeger, V. W., Xi, Y., Pfaendtner, J., & Pozzo, L. D. (2015). Structure Characterization and Properties of Metal-Surfactant Complexes Dispersed in Organic Solvents. Langmuir, 31(33), 9006–9016. https://doi.org/10.1021/acs.langmuir.5b02071

Derjaguin, B. V. (1934). Friction and adhesion. IV. The theory of adhesion of small particles. Kolloid Z., 69(2), 155–164.

Dukes, A. D., McBride, J. R., & Rosenthal, S. J. (2010). Synthesis of magic-sized CdSe and CdTe nanocrystals with diisooctylphosphinic acid. Chemistry of Materials, 22(23), 6402–6408. https://doi.org/10.1021/cm102370a

Elghanian, R., Storhoff, J. J., Mucic, R. C., Letsinger, R. L., & Mirkin, C. a. (1997). Selective colorimetric detection of polynucleotides based on the distance-dependent optical properties of gold nanoparticles. Science (New York, N.Y.), 277(5329), 1078–1081. https://doi.org/10.1126/science.277.5329.1078

Elliott, E. W., Glover, R. D., & Hutchison, J. E. (2015). Removal of Thiol Ligands from Surface-Confined Nanoparticles without Particle Growth or Desorption. ACS Nano, 9(3), 3050–3059. https://doi.org/10.1021/nn5072528

Etienne, P., Phalippou, J., & Sempere, R. (1998). Mechanical properties of nanocomposite organosilicate films. Journal of Materials Science, 33(15), 3999–4005. https://doi.org/10.1023/A:1004609115560

Evans, C. M., Evans, M. E., & Krauss, T. D. (2010). Mysteries of TOPSe revealed: Insights into quantum dot nucleation. Journal of the American Chemical Society, 132(32), 10973–10975. https://doi.org/10.1021/ja103805s

Fan, J. a, Wu, C., Bao, K., Bao, J., Bardhan, R., Halas, N. J., … Capasso, F. (2010). Self-assembled plasmonic nanoparticle clusters. Science, 328(May), 1135–1138. https://doi.org/10.1126/science.1187949

Fan, L., Degen, M., Bendle, S., Grupido, N., & Ilavsky, J. (2010). The absolute calibration of a small-angle scattering instrument with a laboratory X-ray source. Journal of Physics: Conference Series, 247. https://doi.org/10.1088/1742-6596/247/1/012005

Fischer, E. W. (1958). Elektronenmikroskopische Untersuchungen zur Stabilität von Suspensionen in makromolekularen Lösungen. Kolloid Z., 160(22), 120–141.

Flamee, S., Cirillo, M., Abe, S., De Nolf, K., Gomes, R., Aubert, T., & Hens, Z. (2013). Fast, high yield, and high solid loading synthesis of metal selenide nanocrystals. Chemistry of Materials, 25(12), 2476–2483. https://doi.org/10.1021/cm400799e

Frenette, L. C., & Krauss, T. D. (2017). Uncovering active precursors in colloidal quantum dot synthesis. Nature Communications, 8(1), 1–8. https://doi.org/10.1038/s41467-017-01936-z

Frens, G. (1973). Controlled Nucleation for the Regulation of the Particle Size in Monodisperse Gold Suspensions. Nature Physical Science, 241(105), 20–22. https://doi.org/10.1038/physci241020a0

Fu, Q., Sheng, Y., Tang, H., Zhu, Z., Ruan, M., Xu, W., … Tang, Z. (2015). Growth mechanism deconvolution of self-limiting supraparticles based on microfluidic system. ACS Nano, 9(1), 172–179. https://doi.org/10.1021/nn5027998

Gschneidtner, T. A., Fernandez, Y. A. D., Syrenova, S., Westerlund, F., Langhammer, C., & Moth-Poulsen, K. (2014). A versatile self-assembly strategy for the synthesis of shape-selected colloidal noble metal nanoparticle heterodimers. Langmuir, 30(11), 3041–3050. https://doi.org/10.1021/la5002754

Guinier, A., Fournet, G., & Walker, C. B. (1955). Small-Angle Scattering of X-Rays. New York: John Wiley & Sons.

Haas, K. H., & Wolter, H. (1999). Synthesis, properties and applications of inorganic-organic copolymers (ORMOCER®s). Current Opinion in Solid State and Materials Science, 4(6), 571–580. https://doi.org/10.1016/S1359-0286(00)00009-7

Hamaker, H. C. (1937). The London-van der Waals attraction between spherical particles. Physica, 4(10), 1058–1072. https://doi.org/10.1016/S0031-8914(37)80203-7

Harmer, M. A., Farneth, W. E., & Sun, Q. (1996). High surface area nafion resin/silica nanocomposites: A new class of solid acid catalyst. Journal of the American Chemical Society, 118(33), 7708–7715. https://doi.org/10.1021/ja9541950

Harrell, S. M., McBride, J. R., & Rosenthal, S. J. (2013). Synthesis of ultrasmall and magic-sized CdSe nanocrystals. Chemistry of Materials, 25(8), 1199–1210. https://doi.org/10.1021/cm303318f

Hinterwirth, H., Kappel, S., Waitz, T., Lindner, W., Lämmerhofer, M., & Morgenstelle, A. Der. (2013). Quantifying Thiol Ligand Density of Self-Assembled Monolayers on Gold Nanoparticles by Inductively Coupled Plasma Mass Spectrometry Quantifying Thiol Ligand Density of Self-Assembled Monolayers on Gold Nanoparticles by Inductively Coupled Plasma Mass Spec. ACS Nano, 7(2), 1129–1136. https://doi.org/10.1021/nn306024a

Hoinville, J., Bewick, A., Gleeson, D., Jones, R., Kasyutich, O., Mayes, E., … Wong, K. (2003). High density magnetic recording on protein-derived nanoparticles. Journal of Applied Physics, 93(10 2), 7187–7189. https://doi.org/10.1063/1.1555896

Honma, I., Hirakawa, S., Yamada, K., & Bae, J. M. (1999). Synthesis of organic/inorganic nanocomposites protonic conducting membrane through sol-gel processes. Solid State Ionics, 118, 29–36. https://doi.org/10.1016/S0167-2738(98)00450-0

Hostetler, M. J., Templeton, A. C., & Murray, R. W. (1999). Dynamics of place-exchange reactions on monolayer-protected gold cluster molecules. Langmuir, 15(11), 3782–3789. https://doi.org/10.1021/la981598f

Hu, Q., Marand, E., Dhingra, S., Fritsch, D., Wen, J., & Wilkes, G. (1997). Poly (amide-imide)/ TiO2 nano-composite gas separation membranes " Fabrication and characterization. Journal of Membrane Science, 135, 65–79. https://doi.org/http://dx.doi.org/10.1016/S0376-7388(97)00120-8

Hu, Y., & Mackenzie, J. D. (1992). Rubber-like elasticity of organically modified silicates. Journal of Materials Science, 27(16), 4415–4420. https://doi.org/10.1007/BF00541574

Ilavsky, J., & Jemian, P. R. (2009). Irena: Tool suite for modeling and analysis of small-angle scattering. Journal of Applied Crystallography, 42(2), 347–353. https://doi.org/10.1107/S0021889809002222

Iler, R. K. (1979). The Chemistry of Silica. New York: John Wiley & Sons.

Jang, Y., Chung, J., Kim, S., Jun, S. W., Kim, B. H., Lee, D. W., … Hyeon, T. (2011). Simple synthesis of Pd-Fe3O4 heterodimer nanocrystals and their application as a magnetically recyclable catalyst for Suzuki cross-coupling reactions. Physical Chemistry Chemical Physics : PCCP, 13(7), 2512–2516. https://doi.org/10.1039/c0cp01680b

Jasieniak, J., Bullen, C., Van Embden, J., & Mulvaney, P. (2005). Phosphine-free synthesis of CdSe nanocrystals. Journal of Physical Chemistry B, 109(44), 20665–20668. https://doi.org/10.1021/jp054289o

Jasieniak, J., Smith, L., Van Embden, J., Mulvaney, P., & Califano, M. (2009). Re-examination of the size-dependent absorption properties of CdSe quantum dots. Journal of Physical Chemistry C, 113(45), 19468–19474. https://doi.org/10.1021/jp906827m

Jiang, C.-W., & Green, M. A. (2006). Silicon quantum dot superlattices: Modeling of energy bands, densities of states, and mobilities for silicon tandem solar cell applications. Journal of Applied Physics, 99(11), 114902. https://doi.org/10.1063/1.2203394

Kasuya, A., Sivamohan, R., Barnakov, Y. A., Dmitruk, I. M., Nirasawa, T., Romanyuk, V. R., … Kawazoe, Y. (2004). Ultra-stable nanoparticles of CdSe revealed from mass spectrometry. Nature Materials, 3(2), 99–102. https://doi.org/10.1038/nmat1056

Kikuchi, T., & Uchida, T. (2011). Calorimetric method for measuring high ultrasonic power using water as a heating material. Journal of Physics: Conference Series, 279(1), 6–11. https://doi.org/10.1088/1742-6596/279/1/012012

Kim, A., & Berg, J. (2000). Fractal Heteroaggregation of Oppositely Charged Colloids. Journal of Colloid and Interface Science, 229(2), 607–614. https://doi.org/10.1006/jcis.2000.7028

Kim, A. Y., & Berg, J. C. (2000). Fractal aggregation: Scaling of fractal dimension with stability ratio. Langmuir, 16(5), 2101–2104. https://doi.org/10.1021/la990841n

Kim, A. Y., Hauch, K. D., Berg, J. C., Martin, J. E., & Anderson, R. A. (2003). Linear chains and chain-like fractals from electrostatic heteroaggregation. Journal of Colloid and Interface Science, 260(1), 149–159. https://doi.org/10.1016/S0021-9797(03)00033-X

Kim, J. Y., Voznyy, O., Zhitomirsky, D., & Sargent, E. H. (2013). 25th anniversary article: Colloidal quantum dot materials and devices: A quarter-century of advances. Advanced Materials, 25(36), 4986–5010. https://doi.org/10.1002/adma.201301947

Klinkova, A., Choueiri, R. M., & Kumacheva, E. (2014). Self-assembled plasmonic nanostructures. Chemical Society Reviews, 43(11), 3976. https://doi.org/10.1039/c3cs60341e

Kodama, K., Iikubo, S., Taguchi, T., & Shamoto, S. I. (2006). Finite size effects of nanoparticles on the atomic pair distribution functions. Acta Crystallographica Section A: Foundations of Crystallography, 62(6), 444–453. https://doi.org/10.1107/S0108767306034635

Ku, K. H., Shin, J. M., Kim, M. P., Lee, C.-H., Seo, M.-K., Yi, G.-R., … Kim, B. J. (2014). Size-Controlled Nanoparticle-Guided Assembly of Block Copolymers for Convex Lens-Shaped Particles. J. Am. Chem. Soc. https://doi.org/10.1021/ja502075f

Kudera, S., Zanella, M., Giannini, C., Rizzo, A., Li, Y., Gigli, G., … Manna, L. (2007). Sequential growth of magic-size CdSe nanocrystals. Advanced Materials, 19(4), 548–552. https://doi.org/10.1002/adma.200601015

Kumar, S., Gandhi, K. S., & Kumar, R. (2007). Modeling of Formation of Gold Nanoparticles by Citrate Method †. Industrial & Engineering Chemistry Research, 46, 3128–3136. https://doi.org/10.1021/ie060672j

Laibinis, P., Fox, M., Folkers, J., & Whitesides, G. (1991). Comparisons of self-assembled monolayers on silver and gold: mixed monolayers derived from HS (CH2) 21X and HS (CH2) 10Y (X, Y= CH3, CH2OH) have similar. Langmuir, 7(12), 3167–3173. https://doi.org/10.1021/la00060a041

Landes, C. F., Braun, M., & El-Sayed, M. A. (2001). On the nanoparticle to molecular size transition: Fluorescence quenching studies. Journal of Physical Chemistry B, 105(43), 10554–10558. https://doi.org/10.1021/jp0118726

Larson-smith, K., & Pozzo, D. C. (2012). Competitive Adsorption of Thiolated Poly(ethylene glycol) and Alkane-Thiols on Gold Nanoparticles and Its E ff ect on Cluster Formation. Langmuir, 28(37), 13157–13165.

Larson-Smith, K., & Pozzo, D. C. (2011). Scalable synthesis of self-assembling nanoparticle clusters based on controlled steric interactions. Soft Matter, 7(11), 5339–5347. https://doi.org/10.1039/c0sm01497d

Lazarenkova, O. L., & Balandin, A. A. (2002). Electron and phonon energy spectra in a three-dimensional regimented quantum dot superlattice. Physical Review B, 66(24), 245319. https://doi.org/10.1103/PhysRevB.66.245319

Leatherdale, C. A., Woo, W. K., Mikulec, F. V., & Bawendi, M. G. (2002). On the absorption cross section of CdSe nanocrystal quantum dots. Journal of Physical Chemistry B, 106(31), 7619–7622. https://doi.org/10.1021/jp025698c

Lee, J. S., Han, M. S., & Mirkin, C. A. (2007). Colorimetric detection of mercuric ion (Hg2+) in aqueous media using DNA-functionalized gold nanoparticles. Angewandte Chemie - International Edition, 46(22), 4093–4096. https://doi.org/10.1002/anie.200700269

Lee, J, Hernandez, P., Govorov, A. O., & Kotov, N. A. (2007). Exciton-plasmon interactions inmolecular spring assemblies of nanowires and wavelength-based protein detection. Nature Materials, 6(4), 291–295. https://doi.org/10.1038/nmat1869

Lee, Jaebeom, Govorov, A. O., & Kotov, N. A. (2005). Nanoparticle assemblies with molecular springs: A nanoscale thermometer. Angewandte Chemie - International Edition, 44(45), 7439–7442. https://doi.org/10.1002/anie.200501264

Li, D. S., Yoon, S. J., Pelivanov, I., Frenz, M., O'Donnell, M., & Pozzo, L. D. (2017). Polypyrrole-Coated Perfluorocarbon Nanoemulsions as a Sono-Photoacoustic Contrast Agent. Nano Letters, 17(10), 6184–6194. https://doi.org/10.1021/acs.nanolett.7b02845

Love, J. C., Estroff, L. A., Kriebel, J. K., Nuzzo, R. G., & Whitesides, G. M. (2005). Self-Assembled Monolayers of Thiolates on Metals as a Form of Nanotechnology. Chemical Reviews, 105(4), 1103–1170. https://doi.org/10.1021/cr0300789

Loy, D. A., Baugher, B. M., Baugher, C. R., Schneider, D. A., & Rahimian, K. (2000). Substituent effects on the sol-gel chemistry of organotrialkoxysilanes. Chemistry of Materials, 12(12), 3624–3632. https://doi.org/10.1021/cm000451i

Luedtke, W. D., & Landman, U. (1996). Structure, Dynamics, and Thermodynamics of Passivated Gold Nanocrystallites and Their Assemblies. The Journal of Physical Chemistry, 100(32), 13323–13329. https://doi.org/10.1021/jp961721g

Luedtke, W. D., & Landman, U. (1998). Structure and Thermodynamics of Self-Assembled Monolayers on Gold Nanocrystallites. J Phy Chem B, 5647(98), 6566–6572. https://doi.org/10.1021/jp981745i

Mackenzie, J.D. (1993). Nonlinear optical materials by the sol-gel method. Journal of Sol-Gel Science and Technology, 1(1), 7–19.

Mackenzie, John D., Huang, Q., & Iwamoto, T. (1996). Mechanical properties of ormosils. Journal of Sol-Gel Science and Technology, 7(3), 151–161. https://doi.org/10.1007/BF00401034

Majetich, S. A., & Carter, A. C. (1993). Surface effects on the optical properties of cadmium selenide quantum dots. The Journal of Physical Chemistry, 97(34), 8727–8731. https://doi.org/10.1021/j100136a013

Malzbender, J., den Toonder, J. M. J., Balkenende, A. R., & de With, G. (2002). Measuring mechanical properties of coatings: a methodology applied to nano-particle-filled sol–gel coatings on glass. Materials Science and Engineering: R: Reports, 36(2–3), 47–103. https://doi.org/10.1016/S0927-796X(01)00040-7

Mammeri, F., Le Bourhis, E., Rozes, L., & Sanchez, C. (2005). Mechanical properties of hybrid organic-inorganic materials. Journal of Materials Chemistry, 15(35–36), 3787–3811. https://doi.org/10.1039/b507309j

Martin, M. N., Basham, J. I., Chando, P., & Eah, S. K. (2010). Charged gold nanoparticles in non-polar solvents: 10-min synthesis and 2D self-assembly. Langmuir, 26(17), 7410–7417. https://doi.org/10.1021/la100591h

McBride, J. R., Dukes, A. D., Schreuder, M. A., & Rosenthal, S. J. (2010). On ultrasmall nanocrystals. Chemical Physics Letters, 498(1–3), 1–9. https://doi.org/10.1016/j.cplett.2010.08.052

Michalet, X., Pinaud, F. F., Bentolila, L. A., Tsay, J. M., Doose, S., Li, J. J., … Weiss, S. (2005). Quantum Dots for Live Cells, in Vivo Imaging, and Diagnostics. Science, 307(5709), 538–544. https://doi.org/10.1126/science.1104274

Mucic, R. C., Storhoff, J. J., Mirkin, C. A., & Letsinger, R. L. (1998, December). DNA-directed synthesis of binary nanoparticle network materials [5]. Journal of the American Chemical Society. https://doi.org/10.1021/ja982721s

Murcia, M. J., Shaw, D. L., Woodruff, H., Naumann, C. A., Young, B. A., & Long, E. C. (2006). Facile sonochemical synthesis of highly luminescent ZnS-shelled CdSe quantum dots. Chemistry of Materials, 18(9), 2219–2225. https://doi.org/10.1021/cm0505547

Nevers, D. R., Williamson, C. B., Savitzky, B. H., Hadar, I., Banin, U., Kourkoutis, L. F., … Robinson, R. D. (2018). Mesophase Formation Stabilizes High-Purity Magic-Sized Clusters. Journal of the American Chemical Society, 140(10), 3652–3662. https://doi.org/10.1021/jacs.7b12175

Nie, S. (1997). Probing Single Molecules and Single Nanoparticles by Surface-Enhanced Raman Scattering. Science, 275(5303), 1102–1106. https://doi.org/10.1126/science.275.5303.1102

Nie, Z., Petukhova, A., & Kumacheva, E. (2010). Properties and emerging applications of self-assembled structures made from inorganic nanoparticles. Nature Nanotechnology, 5(1), 15–25. https://doi.org/10.1038/nnano.2009.453

Ning, Z., Molnár, M., Chen, Y., Friberg, P., Gan, L., Ågren, H., & Fu, Y. (2011). Role of surface ligands in optical properties of colloidal CdSe/CdS quantum dots. Physical Chemistry Chemical Physics, 13(13), 5848–5854. https://doi.org/10.1039/c0cp02688c

Nishida, N., Hara, M., Sasabe, H., & Knoll, W. (1997). Formation and Exchange Processes of Alkanethiol Self-Assembled Monolayer on Studied by Thermal Desorption Spectroscopy and Scanning Tunneling Microscopy Au (111). Japanese Journal of Applied Physics, Part 1, 36(4A), 2379–2385.

Nishiyama, N., Asakura, T., & Horie, K. (1988). Condensation behavior of a sulane coupling agent in the presence of colloidal silica studied by 29Si and 13C NMR. Journal of Colloid And Interface Science, 124(1), 14–21. https://doi.org/10.1016/0021-9797(88)90319-0

Nishiyama, N., Horie, K., & Asakura, T. (1989). Adsorption behavior of a silane coupling agent onto a colloidal silica surface studied by 29Si NMR spectroscopy. Journal of Colloid And Interface Science, 129(1), 113–119. https://doi.org/10.1016/0021-9797(89)90420-7

Nunes, S. P., Schultz, J., & -V., P. K. (1996). Silicon Membranes with Silica Nanoparticles. Journal of Materials Science Letters, 15(13), 1139–1141.

Onoda, G. Y., & Liniger, E. G. (1990). Random loose packings of uniform spheres and the dilatancy onset. Physical Review Letters, 64(22), 2727–2730. https://doi.org/10.1103/PhysRevLett.64.2727

Ouyang, J., Zaman, M. B., Yan, F. J., Johnston, D., Li, G., Wu, X., … Yu, K. (2008). Multiple families of magic-sized CdSe nanocrystals with strong bandgap photoluminescence via noninjection one-pot syntheses. Journal of Physical Chemistry C, 112(36), 13805–13811. https://doi.org/10.1021/jp803845n

Ozbay, E. (2006). Plasmonics : Merging Photonics and Electronics at Nanoscale Dimensions. Science, 311(5758), 189–193. https://doi.org/10.1126/science.1114849

Palmisano, G., Le Bourhis, E., Ciriminna, R., Tranchida, D., & Pagliaro, M. (2006). ORMOSIL thin films: Tuning mechanical properties via a nanochemistry approach. Langmuir, 22(26), 11158–11162. https://doi.org/10.1021/la061520w

Park, J., Joo, J., Soon, G. K., Jang, Y., & Hyeon, T. (2007). Synthesis of monodisperse spherical nanocrystals. Angewandte Chemie - International Edition, 46(25), 4630–4660. https://doi.org/10.1002/anie.200603148

Polte, J., Kraehnert, R., Radtke, M., Reinholz, U., Riesemeier, H., Thünemann, A. F., & Emmerling, F. (2010). New insights of the nucleation and growth process of gold nanoparticles via in situ coupling of SAXS and XANES. Journal of Physics: Conference Series, 247, 012051. https://doi.org/10.1088/1742-6596/247/1/012051

Pong, B. K., Elim, H. I., Chong, J. X., Ji, W., Trout, B. L., & Lee, J. Y. (2007). New insights on the nanoparticle growth mechanism in the citrate reduction of gold(III) salt: Formation of the Au nanowire intermediate and its nonlinear optical properties. Journal of Physical Chemistry C, 111(17), 6281–6287. https://doi.org/10.1021/jp068666o

Priyadharshini, A., Kalainathan, S., Boury, B., & Corriu, R. J. P. (1996). Hybrid Organic-inorganic Materials with Second-order Optical Nonlinearities Synthesized via Sol-gel Chemistry. Pure and Applied Optics, 5, 689–699.

Protière, M., Nerambourg, N., Renard, O., & Reiss, P. (2011). Rational design of the gram-scale synthesis of nearly monodisperse semiconductor nanocrystals. Nanoscale Research Letters, 6(1), 1–14. https://doi.org/10.1186/1556-276X-6-472

Rao, C. N. R., Vivekchand, S. R. C., Biswas, K., & Govindaraj, A. (2006). Synthesis of inorganic nanomaterials. Journal of the Chemical Society. Dalton Transactions, (34), 3728–3749. https://doi.org/10.1039/b708342d

Ruberu, T. P. A., Albright, H. R., Callis, B., Ward, B., Cisneros, J., Fan, H. J., & Vela, J. (2012). Molecular control of the nanoscale: Effect of phosphine-chalcogenide reactivity on CdS-CdSe nanocrystal composition and morphology. ACS Nano, 6(6), 5348–5359. https://doi.org/10.1021/nn301182h

Sader, J. E., Carnie, S. L., & Chan, D. Y. C. (1995). Accurate Analytic formulas for the Double-Layer Interaction between Spheres. Journal of Colloid and Interface Science, 171, 46–54.

Salazar-Alvarez, G., Lidbaum, H., López-Ortega, A., Estrader, M., Leifer, K., Sort, J., … Nogués, J. (2011). Two-, Three-, and four-component magnetic multilayer onion nanoparticles based on iron oxides and manganese oxides. Journal of the American Chemical Society, 133(42), 16738–16741. https://doi.org/10.1021/ja205810t

Sanchez, C., Ribot, F., & Lebeau, B. (1999). Molecular design of hybrid organic–inorganic nanocomposites synthesized. Journal of Materials Chemistry, 9, 35–44.

Schlenoff, J. B., Li, M., & Ly, H. (1995). Stability and self-exchange in alkanethiol monolayers. Journal of the American Chemical Society, 117(50), 12528–12536. https://doi.org/10.1021/ja00155a016

Shen, W., Tang, H., Yang, X., Cao, Z., Cheng, T., Wang, X., … Deng, Z. (2017). Synthesis of highly fluorescent InP/ZnS small-core/thick-shell tetrahedral-shaped quantum dots for blue light-emitting diodes. Journal of Materials Chemistry C, 5(32), 8243–8249. https://doi.org/10.1039/C7TC02927F

Sivakumar, M., Towata, A., Yasui, K., Tuziuti, T., Kozuka, T., Iida, Y., … Ashok, M. (2012). Ultrasonic cavitation induced water in vegetable oil emulsion droplets - A simple and easy technique to synthesize manganese zinc ferrite nanocrystals with improved magnetization. Ultrasonics Sonochemistry, 19(3), 652–658. https://doi.org/10.1016/j.ultsonch.2011.10.015

Stober, W., & Fink, A. (1968). Controlled Growth of Monodispersed Silica Spheres in the Micron Size Range. Journal of Colloid and Interface Science, 26, 62–69. https://doi.org/10.1016/0021-9797(68)90272-5

Stover, R. J., Moaseri, E., Gourisankar, S. P., Iqbal, M., Rahbar, N. K., Changalvaie, B., … Johnston, K. P. (2016). Formation of Small Gold Nanoparticle Chains with High NIR Extinction through Bridging with Calcium Ions. Langmuir, 32, 1127–1138. https://doi.org/10.1021/acs.langmuir.5b03639

Stover, R. J., Murthy, A. K., Nie, G. D., Gourisankar, S., Dear, B. J., Truskett, T. M., … Johnston, K. P. (2014). Quenched Assembly of NIR-Active Gold Nanoclusters Capped with Strongly Bound Ligands by Tuning Particle Charge via pH and Salinity. Journal of Physical Chemistry C, 118, 14291–14298.

Sun, S. (2000). Monodisperse FePt Nanoparticles and Ferromagnetic FePt Nanocrystal Superlattices. Science, 287(5460), 1989–1992. https://doi.org/10.1126/science.287.5460.1989

Sun, Shouheng, Yu, H., & Wang, S. X. (2006). US 2006/0053971 A1. https://doi.org/US 2010/0311130 Al

Suslick, K. S. (1990). Sonochemistry. Science, 247, 1439–1445.

Suslick, K. S., Choe, S.-B., Cichowlas, A. a., & Grinstaff, M. W. (1991). Sonochemical synthesis of amorphous iron. Nature, 353(6343), 414–416. https://doi.org/10.1038/353414a0

Suslick, K. S., Fang, M., & Hyeon, T. (1996). Sonochemical synthesis of iron colloids. Journal of the American Chemical Society, 118(47), 11960–11961. https://doi.org/10.1021/ja961807n

Talapin, D. V., Rogach, A. L., Kornowski, A., Haase, M., & Weller, H. (2001). Highly Luminescent Monodisperse CdSe and CdSe/ZnS Nanocrystals Synthesized in a Hexadecylamine-Trioctylphosphine Oxide-Trioctylphospine Mixture. Nano Letters, 1(4), 207–211. https://doi.org/10.1021/nl0155126

Talapin, D. V, Lee, J., Kovalenko, M. V, & Shevchenko, E. V. (2010). Prospects of Colloidal Nanocrystals for Electronic and Optoelectronic Applications. Chemical Reviews, 110(1), 389–458. https://doi.org/10.1021/cr900137k

Teixeira, J. (1988). Small-angle scattering by fractal systems. Journal of Applied Crystallography, 21(6), 781–785. https://doi.org/10.1107/S0021889888000263

Tseng, R. J., Tsai, C., Ma, L., Ouyang, J., Ozkan, C. S., & Yang, Y. (2006). Digital memory device based on tobacco mosaic virus conjugated with nanoparticles. Nature Nanotechnology, 1(1), 72–77. https://doi.org/10.1038/nnano.2006.55

Turkevich, J., Stevenson, P. C., Hillier, J. (1951). A Study of the Nucleation and Growth Processes in the Synthesis of Colloidal Gold. Discuss. Faraday. Soc., 11, 55–75.

Usui, H., Shimizu, Y., Sasaki, T., & Koshizaki, N. (2005). Photoluminescence of ZnO Nanoparticles Prepared by Laser Ablation in Different Surfactant Solutions, 120–124. https://doi.org/10.1021/jp046747j

Van Embden, J., Chesman, A. S. R., & Jasieniak, J. J. (2015). The heat-up synthesis of colloidal nanocrystals. Chemistry of Materials, 27(7), 2246–2285. https://doi.org/10.1021/cm5028964

Verwey, E. J. W., & Overbeek, J. T. G. (1948). Thoery of the Stability of Lyophobic Colloids. Amsterdam: Elsevier.

Vijaya Kumar, R., Diamant, Y., & Gedanken, A. (2000). Sonochemical synthesis and characterization of nanometer-size transition metal oxides from metal acetates. Chemistry of Materials, 12(8), 2301–2305. https://doi.org/10.1021/cm000166z

Wang, C., Xu, C., Zeng, H., & Sun, S. (2009). Recent progress in syntheses and applications of dumbbell-like nanoparticles. Advanced Materials, 21(30), 3045–3052. https://doi.org/10.1002/adma.200900320

Williamson, C. B., Nevers, D. R., Hanrath, T., & Robinson, R. D. (2015). Prodigious Effects of Concentration Intensification on Nanoparticle Synthesis: A High-Quality, Scalable Approach. Journal of the American Chemical Society, 137(50), 15843–15851. https://doi.org/10.1021/jacs.5b10006

Williamson, C. B., Nevers, D. R., Nelson, A., Hadar, I., Banin, U., Hanrath, T., & Robinson, R. D. (2019). Chemically reversible isomerization of Inorganic Clusters. Science, 363(6428), 731–735.

Wuithschick, M., Birnbaum, A., Witte, S., Sztucki, M., Vainio, U., Pinna, N., … Polte, J. (2015). Turkevich in New Robes: Key Questions Answered for the Most Common Gold Nanoparticle Synthesis. ACS Nano, 9(7), 7052–7071. https://doi.org/10.1021/acsnano.5b01579

Xi, Y., & Pozzo, L. D. (2017). Electric field directed formation of aligned conjugated polymer fibers. Soft Matter, 13(21), 3894–3908. https://doi.org/10.1039/c7sm00485k

Xu, C., Xie, J., Ho, D., Wang, C., Kohler, N., Walsh, E. G., … Sun, S. (2008). Au-Fe3O4 dumbbell nanoparticles as dual-functional. Angewandte Chemie - International Edition, 47(1), 173–176. https://doi.org/10.1002/anie.200704392

Yan, N., Liu, H., Zhu, Y., Jiang, W., & Dong, Z. (2015). Entropy-Driven Hierarchical Nanostructures from Cooperative Self-Assembly of Gold Nanoparticles/Block Copolymers under Three-Dimensional Confinement. Macromolecules, 48(16), 5980–5987. https://doi.org/10.1021/acs.macromol.5b01219

Yu, Q., & Liu, C. Y. (2009). Study of magic-size-cluster mediated formation of cds nanocrystals: Properties of the magic-size clusters and mechanism implication. Journal of Physical Chemistry C, 113(29), 12766–12771. https://doi.org/10.1021/jp903199y

Yu, S., Wong, T. K. S., Hu, X., & Pita, K. (2003). The Effect of TEOS/MTES Ratio on the Structural and Dielectric Properties of Porous Silica Films. Journal of The Electrochemical Society, 150(5), F116. https://doi.org/10.1149/1.1566021

Yun-Sheng, X., & Zhu, C.-Q. (2008). Aqueous synthesis of luminescent magic sized CdSe nanoclusters. Materials Letters, 62(14), 2103–2105.

Zeng, B. H., Duan, G., Li, Y., Yang, S., & Xu, X. (2010). Blue Luminescence of ZnO Nanoparticles Based on Non-Equilibrium Processes : Defect Origins and Emission Controls, 561–572. https://doi.org/10.1002/adfm.200901884

Zhang, Q., Chan, H. L. W., Zhou, Q., & Choy, C. L. (1998). Study on the pyroelectric properties of PLT/P (VDF-TrFE) nanocomposites. Chinese Science Bulletin, 43(2), 111–114.

VITA

Ryan Kastilani

Education

Ph.D. Chemical Engineering – University of Washington; 2019
B.S. Chemical Engineering – University of California, Los Angeles; 2014

Professional Experience

Software Engineer Intern - The Trade Desk, Sep 2018 – Dec 2018

- Developed a service that periodically queries the database and caches the data for a system health monitor. Existing SQL queries were optimized to reduce I/O by orders of magnitude, resulting in significantly improved performance and responsiveness of the monitoring application.
- Developed a dashboard for engineering quality metrics. Data are obtained periodically from the resources' REST API, stored in a database, and aggregated on demand from the dashboard.
- Integrated Amazon S3 with a database using Dell Boomi.

Data Scientist Intern – Optimum Energy, Mar 2017 – Jun 2017

- Established data-driven optimization paradigm, from data cleaning to application of machine learning.
- Developed a regression model to optimize pump speeds with < 10% error, potentially saving several hundred thousand dollars and thousands of man-hours per year.
- Featured in http://knkx.org/post/uw-developing-curriculum-help-grow-jobs-use-big-data-harness-clean-energy.

Chief Technology Officer – Membrion Inc, Feb 2017 – May 2017

- Commercialized membrane filters, leading technical development.
- Won $25,000 UW Business Plan Competition and $6,000 from Environmental Innovation Challenge.
- Featured in https://www.geekwire.com/2017/molecule-filter-maker-membrion-wins-top-prize-university-washington-business-plan-competition/.

Intern Engineer – Lam Research Corporation, Jun 2013 – Sep 2013

- Developed a novel start-up process to be used by all members in a family etch tools.
- Earned the Lam Research Outstanding Contribution Award and 4th place in intern poster competition (> 70 interns).

Process Engineer Intern – Ecogreen Oleochemicals, Jun 2012 – Aug 2012

- Analyzed heat exchangers to detect fouling and identify potentially problematic heat exchangers.

Honors and Awards

- $25,000 UW Business Plan Competition winner – 2017
- $6,000 Clean Energy Prize at Environmental Innovation Challenge – 2017
- Clean Energy Institute Graduate Fellowship – 2016
- Runstad Family Endowed Fellowship – 2014
- Lam Research Corporation Outstanding Contribution Award – 2013
- Lam Research Corporation 4th place Intern Poster Competition Award – September 2013

Publications and Conference Presentations.

Kastilani R**,** Bishop BP, Holmberg VC, Pozzo LD. On-Demand Sonochemical Synthesis of Ultrasmall and Magic-Size CdSe Quantum Dots in Single-Phase and Emulsion Systems. In Preparation.

Kastilani R, Wong R, Pozzo LD. Efficient Electrosteric Assembly of Nanoparticle Heterodimers and Linear Heteroassemblies. *Langmuir*. **2018** 34 (3), 826-836.

Kastilani R, Pozzo LD. Efficient Electrosteric Assembly of Nanoparticle Heterodimers and Linear Heteroassembliesns. Oral talk presented at Graduate Student Symposium; 2016 September 22; Seattle, WA.

Kastilani R, Pozzo LD. Scalable and controlled heteroaggregation of nanoparticles in aqueous media using electrostatic attraction and controlled steric interactions. Oral talk presented at 90th ACS Colloid & Surface Science Symposium; 2016 June 5-8; Boston, MA.

Kastilani R, Pozzo LD. Synthesis of heterogeneous gold nanoparticle clusters in aqueous media using electrostatic attraction and controlled steric interactions. Poster presented at NanoDDS, 13th International Nanomedicine & Drug Delivery Symposium 2015; 2015 September 16-18; Seattle, WA.

Teaching Assistantship at University of Washington

ChemE 340: Transport Processes II, Heat Transfer (2018, 2019)
ChemE 455: Surface and Colloid Science Laboratory (2016)
ChemE 486: Process Design II (2015)

Service

Test Assistant – Science Olympiad at University of Washington, 2017
In charge of writing and scoring the materials science division.

Tutor – Seattle MESA, Mar 2016 – Jun 2016
Tutor high school students from underprivileged backgrounds in STEM subjects.

Tutor – Tau Beta Pi Engineer Honor Society, Sep 2012 – Dec 2012
Tutor for math, physics, chemistry, and chemical engineering undergraduate students.